

NORTHWESTERN UNIVERSITY

A DISSERTATION

Applications of Volume Holographic Gratings for Signal Processing

SUBMITTED TO THE GRADUATE SCHOOL IN PARTIAL FULFILLMENT OF THE  
REQUIREMENTS

for the degree

DOCTOR OF PHILOSOPHY

Field of Electrical Engineering and Computer Science

By

John Thomas Shen

EVANSTON, ILLINOIS

June 2007

## ABSTRACT

## Applications of Volume Holographic Gratings for Signal Processing

John Thomas Shen

The work presented here represents a series of research projects that are unified in their goal: to use volume holographic gratings to enhance traditional signal processing applications in ways that would otherwise not be possible. To this end, we have completed work that can be classified into four different projects. First, we have developed experimentally a novel holographic medium for volume holographic gratings. Future work on this material will center on achieving greater consistency of results. Second, we have studied the formation of highly selective holographic spectral filters for optical communications using the material that we have developed. Future work will include using optimized material samples and using beam profiling and apodization to achieve the desired filter shape. Third, we have studied the design of a holographic Stokesmeter. We have determined the proper figures of merit for the noise-tolerance of such a Stokesmeter, and have shown how the robustness of this Stokesmeter depends on the properties of its volume holographic gratings. Future work will entail developing a version of the holographic Stokesmeter for laser radar. Finally, we have studied the use of a super-parallel holographic random-access memory (SPHRAM) as the database for a holographic smart eye that can perform high-speed searches using a real-time Vanderlugt correlator. This holographic smart eye has the potential to perform high speed, translation-invariant correlation searches. The SPHRAM was studied theoretically, and the lenslet array, a key component of the SPHRAM, was designed and tested using an industrial optical simulation. With this design in hand, the SPHRAM can now be completed. While developing the full SPHRAM design, we built a real-time Vanderlugt correlator and constructed a prototype holographic smart eye using a

disc-based holographic memory system as an alternative to the SPHRAM while the latter is under development. Using the prototype holographic smart eye, a holographic data storage disc was successfully searched for a query image in an automated fashion. Once the holographic smart eye is completed, it can be combined with the polarimetric LADAR system to create a target recognition system that is capable of searching a massive database at high speed for a given query image using visible and polarimetric signature data. Such a device would have a myriad of possible applications, none of which are possible using current technology.

## Acknowledgements

I would like to thank the faculty and staff in the Electrical Engineering & Computer Science department, who have all contributed to my education and to this thesis in some way. I am especially grateful to the workers in the machine shop, who were always helpful in guiding my woeful mechanical designs as well as prompt in completing that same work.

All of the members of the Laboratory for Atomic and Photonic Technologies have contributed greatly to this work by engaging in countless discussions with me, including Venkatesh Gopal, Alex Heifetz, and Jong-Kwon Lee. I am especially grateful for the help that Gour Pati, Shih Tseng, Mary Salit, and Ken Salit have provided over the years.

The three professors of my thesis exam committee have been by far the most influential personas in my time at Northwestern. Professors Allen Taflove and Alan Sahakian have been mentoring me before I was even a graduate student here; indeed, for most of my 9 years in Evanston. My advisor Selim Shahriar has directed my graduate education well, and I am thankful for the way he has guided and advanced my methods of analysis and execution.

I would be remiss if I did not thank my family for their support over the years. Mary, Holly, and Andrew were all a source of support and inspiration. My parents were always ready to advise me or help me in any way they could. It is no exaggeration to say that without their love and support, this document would not exist. Finally, to my wife Myra, who helped me edit this document: I love you!

## Contents

1	Background.....	12
1.1	Historical Background .....	12
1.2	Holography .....	14
1.3	Properties of Volume Holograms .....	18
1.4	Angle-Multiplexing in Volume Holograms.....	20
1.5	Conclusion .....	21
2	Holographic Materials Development.....	22
2.1	Introduction.....	22
2.2	Material Parameters .....	23
2.3	Photorefractive Materials.....	26
2.4	Photopolymer Materials.....	27
2.5	Northwestern Dye-doped Photopolymer Material.....	29
2.6	Experimental Development .....	31
2.6.1	Preliminary Experiment.....	31
2.6.2	Large Area Holographic Plate .....	31
2.6.3	Thick Material.....	39
2.7	A Simple Technique for Determining the $M_{\#}$ .....	44
2.8	Conclusion and Next Steps .....	52
3	Holographic Spectral Filters .....	53
3.1	Introduction.....	53
3.2	Theoretical Background.....	54
3.2.1	Simple Bragg Method.....	54
3.2.2	Coupled-Wave Theory Results.....	64
3.3	Experimental Results .....	69
3.3.1	First Test: Dye Laser.....	70
3.3.2	Six Holographic Spectral Filters for 1550 nm .....	72
3.4	Conclusion and Next Steps .....	78
4	Holographic Stokesmeter.....	80
4.1	Introduction.....	80
4.2	Basic Architecture.....	81
4.3	Volume Grating Requirements .....	87
4.4	Holographic Beam Combiner for an Active Holographic Stokesmeter .....	95
4.5	Conclusion and Next Steps .....	102
5	Super Parallel Holographic Architectures .....	104
5.1	Introduction.....	104
5.2	Super Parallel Holographic Optical Correlator.....	106
5.2.1	Architecture.....	106
5.2.2	Preliminary Experimental Data.....	108
5.2.3	Conclusion .....	110
5.3	Super Parallel Holographic Random Access Memory .....	110
5.3.1	Architecture.....	110
5.3.2	Experiment.....	112
5.3.3	Conclusion .....	113

		6
5.4	Lenslet Array .....	114
5.4.1	Introduction.....	114
5.4.2	Phase Transformation for Plane Waves.....	116
5.4.3	ZEMAX Simulation.....	118
5.4.4	Conclusion .....	119
5.5	Conclusion and Next Steps.....	120
6	Disc-based Holographic Memory System .....	121
6.1	Introduction.....	121
6.2	Design Overview .....	122
6.2.1	Write Architecture .....	122
6.2.2	Read Architecture .....	124
6.3	LAPT Disc-based Holographic Memory System .....	125
6.3.1	Overview.....	125
6.3.2	Beam Conditioning.....	128
6.3.3	Image Beam: Spatial Light Modulator .....	129
6.3.4	Image Relay Optics.....	133
6.3.5	Reference Beam Optics.....	134
6.3.6	Exposure Schedule.....	136
6.3.7	Holographic Disc Material.....	140
6.3.8	Writing Procedure.....	141
6.3.9	Results.....	144
6.4	Conclusion and Next Steps.....	146
7	Real-time Vanderlugt Correlator .....	149
7.1	Introduction.....	149
7.2	Vanderlugt Correlator .....	150
7.3	Real-time Correlation.....	153
7.3.1	Vanderlugt Configuration .....	154
7.3.2	Phase-conjugation Configuration.....	155
7.3.3	Photorefractive Polymer .....	157
7.3.4	Experimental Results .....	161
7.4	Conclusion and Next Steps.....	167
8	Holographic Smart Eye.....	169
8.1	Introduction.....	169
8.2	Holographic Smart Eye Overview .....	170
8.3	Experimental Design.....	172
8.3.1	Introduction.....	172
8.3.2	Experimental Setup.....	172
8.3.3	Results.....	176
8.4	Conclusion and Next Steps.....	177
9	References.....	180
10	Appendices.....	189
10.1	Coupled-wave Theory.....	189
10.2	Fourier Optics and the Lens.....	192
10.3	4f Imaging Systems.....	197
10.4	Common Holographic Calculations.....	198

11	Vita.....	7 202
----	-----------	----------

## List of Figures

Figure 1-1: Creating a Hologram.....	14
Figure 1-2: Recording geometries .....	16
Figure 1-3: Grating geometry and parameters .....	19
Figure 1-4: Writing an angle-multiplexed grating.....	20
Figure 1-5: Reading an angle-multiplexed grating .....	21
Figure 2-1: First holographic plate attempt .....	32
Figure 2-2: $M_{\#}$ for first 4"x4" sample .....	33
Figure 2-3: Typical Material Response Curve.....	34
Figure 2-4: Second 4"x4" sample .....	34
Figure 2-5: Angle-Multiplexing Laboratory Setup.....	36
Figure 2-6: Comparison of SLM image (left) and hologram image (right).....	37
Figure 2-7: A selection from the 80 multiplexed images .....	38
Figure 2-8: First thick material successes .....	39
Figure 2-9: 1.5x1.5x1.3 cm sample .....	40
Figure 2-10: Result of dye laser frequency scan.....	41
Figure 2-11: Sample created in fluorometer cell .....	43
Figure 2-12: Index matching setup .....	44
Figure 2-13: Simulation result showing the evolution of diffracted pattern as a function of holographic exposure for an even $Q$ ( $m=5, n=0, \alpha=0$ in equation (2.16) value material with a plane wave read-out beam. Normalized diffraction efficiency is plotted versus radial distance.	49
Figure 2-14: Simulation result for the diffraction pattern for fractional $Q$ with a plane wave read-out beam ( $m=5, n=0, \alpha=0.2$ in equation 10). Normalized diffraction efficiency is plotted versus radial distance. ....	49
Figure 2-15 :Writing and Read-out Geometry.....	50
Figure 3-1: Volume Holographic Grating.....	55
Figure 3-2: Multiple Reflections from a Bragg grating.....	56
Figure 3-3: a) Bragg-matched and b) Bragg-mismatched vector summations .....	57
Figure 3-4: Summation showing first null .....	58
Figure 3-5: Summation showing first sideband .....	59
Figure 3-6: Key reflections from the grating planes.....	59
Figure 3-7: Comparison between the CWT and SBT for an index of modulation of $1e-4$ .....	62
Figure 3-8: Difference between the CWT and SBT in Figure 3-7 .....	62
Figure 3-9: Comparison between the CWT and SBT for an index of modulation of $1e-5$ .....	63
Figure 3-10: Difference between the CWT and SBT in Figure 3-9 .....	64
Figure 3-11: Geometry for Coupled-Wave results .....	65
Figure 3-12: Plot comparing the spectral bandwidth of transmission and reflection gratings .....	67
Figure 3-13: Plot comparing the spectral bandwidth for differing grating thicknesses.....	68
Figure 3-14: Writing setup for holographic filter .....	71
Figure 3-15: Oscilloscope trace showing frequency scan and diffracted power .....	72
Figure 3-16: Transmission write/Reflection read geometry .....	74
Figure 3-17: Glass cell and index matching setups with primary reflection .....	75
Figure 3-18: Index Matching Setup .....	76
Figure 3-19: Six holographic spectral filters .....	77

	9
Figure 3-20: Comparison of six holographic filters.....	78
Figure 4-1: Holographic Stokesmeter Architecture.....	82
Figure 4-2: Mueller matrix representation of holographic diffraction.....	82
Figure 4-3: Volume grating diffraction.....	83
Figure 4-4: Readout setup.....	90
Figure 4-5: Theoretical vs. Experimental polarization dependence of the diffraction efficiency	91
Figure 4-6: Percent error plotted versus contrast ratio for each Stokes parameter for the case of AWGN in the intensity measurements. The separate lines in each graph represent the different noise levels: +=-25dB, o=-30dB, x=-35dB, □=-40dB, *=no noise .....	92
Figure 4-7: Percent error plotted versus contrast ratio for each Stokes parameter for the case of AWGN in the measurement matrix. The separate lines in each graph represent the different noise levels: +=-25dB, o=-30dB, x=-35dB, □=-40dB, *=no noise .....	93
Figure 4-8: Heterodyne receiver for holographic Stokesmeter.....	94
Figure 4-9: Conventional phase-locked beam combiner system .....	95
Figure 4-10: Holographic beam combiner system.....	96
Figure 4-11: a) Numerical simulation b) Transmitted beam c) Diffracted beams.....	99
Figure 4-12: Experimental setup for holographic beam combiner .....	100
Figure 4-13: a) Numerical simulation b) Experimental result .....	101
Figure 5-1: SPHOC Architecture.....	106
Figure 5-2: HMDX test.....	108
Figure 5-3: SPHOC Initial Results .....	109
Figure 5-4: SPHRAM Architecture .....	111
Figure 5-5: SPHRAM Feasibility Experiment.....	112
Figure 5-6: Details of a “unit cell” of the lenslet array.....	115
Figure 5-7: LLA in a 3-spatial-location HMU SPHOC/SPHRAM architecture. Beams propagate left to right for SPHOC operation, and right to left for SPHRAM operation.....	116
Figure 5-8: Seidel spherical aberration coefficient for each of four designs .....	119
Figure 6-1: Block Diagram of the Write Architecture.....	123
Figure 6-2: Block Diagram of the Read Architecture.....	125
Figure 6-3: Disc-based Holographic Memory .....	127
Figure 6-4: Spatial Filter .....	128
Figure 6-5: PBS cube, Mask, and Half-wave Plate .....	129
Figure 6-6: DLP SLM.....	130
Figure 6-7: FLC SLM.....	131
Figure 6-8: FLC SLM Polarization Rotation.....	132
Figure 6-9: FLC SLM Architecture .....	132
Figure 6-10: Basic 4f System.....	134
Figure 6-11: 4f System to reduce/expand image size .....	134
Figure 6-12: Galvo mirror.....	135
Figure 6-13: Equilateral Triangle Arrangement of the Galvo Mirrors .....	135
Figure 6-14: Typical Material Response Curve.....	136
Figure 6-15: Equal exposure holograms .....	138
Figure 6-16: Equal grating strength holograms .....	139
Figure 6-17: Memplex™ in Disc Mount .....	141
Figure 6-18: Aprilis CROP Media Disc.....	141

	10
Figure 6-19: Holographic Disc Write Program .....	143
Figure 6-20: Image from the first disc .....	144
Figure 6-21: Data Retrieved from the second Aprilis Disc .....	146
Figure 7-1: Vanderlugt Correlation Steps.....	150
Figure 7-2: Joint Transform Correlator.....	152
Figure 7-3: Real-time Vanderlugt Correlator .....	155
Figure 7-4: Phase-conjugation .....	157
Figure 7-5: NDT Photorefractive Polymer Material.....	158
Figure 7-6: Image and Fourier Transform .....	158
Figure 7-7: Two Dissimilar Images .....	159
Figure 7-8: Cross Correlation (left) and Self Correlation (right).....	160
Figure 7-9: Edge-enhanced Image .....	160
Figure 7-10: Cross Correlation (left) and Self Correlation (right) with Edge-Enhancement .....	161
Figure 7-11: Phase-conjugation/Correlation Experiment .....	162
Figure 7-12: Diagram of Phase-conjugation/Correlation Experiment.....	162
Figure 7-13: Correlation of a Pair of Jets.....	166
Figure 8-1: Image Acquisition .....	170
Figure 8-2: Conceptualization of the Holographic Smart Eye.....	171
Figure 8-3: Experimental Design of the Holographic Smart Eye.....	174
Figure 8-4: Smart Eye Control Program .....	175
Figure 10-1: Two Multiplexed Volume Gratings .....	189
Figure 10-2: $4f$ System.....	197
Figure 10-3: Asymmetric Grating.....	199

**List of Tables**

Table 2-1: Preliminary Holographic Material Recipe .....	31
Table 2-2: Baking schedule for 4"x4" sample .....	35
Table 2-3: Experimentally observed diffraction pattern for 4 different exposures. As one reaches the optimum limit for holographic exposure, the number of interference fringes visible in the diffracted beam each a maximum. ....	51
Table 7-1: Correlation and Phase Conjugation Results .....	165
Table 8-1: Results of the Holographic Smart Eye Search .....	176

# 1 Background

## 1.1 *Historical Background*

In his Nobel Prize acceptance speech, Dennis Gabor called his invention of holography “serendipity”. He was referring to the fact that his original intention was to create a way to magnify x-ray images. Gabor had realized that recording the interference between a wavefront and a coherent wave would allow the reconstruction of that exact wavefront at a later point in time by applying just the coherent wave to the recording.<sup>1</sup> Although he realized at the time that his idea of wavefront reconstruction could be applied to recording three-dimensional (3D) scenes, it was not until the invention of the laser that holography began to take flight.

The laser quickly became a reliable and commonplace coherent source for holography, and Leith and Upatnieks in the United States and Denisjuk in the Soviet Union began to create holograms of 3D objects in 1963.<sup>2-4</sup> They solved one of the problems of Gabor's original geometry, ghost images, by moving one of the recording beams off-axis. This “off-axis” recording geometry was the result of applying communications theory to the problem of the twin-images, and opened the door for work on the storage of multiple images in a hologram.

By the early 1970s, researchers had already realized the enormous potential of holographic data storage by storing multiple holograms throughout the volume of a material, but were unable to make the technology viable. This failure was largely due to the fact that the components necessary for creating a holographic data storage system—spatial light modulators, CCD detectors, and most importantly, high quality holographic materials—were still in their infancy. Despite this limitation, important theoretical advances were made.<sup>5-9</sup>

The research that was done in these early years allowed the growth of many types of optical processing architectures, even as holographic data storage research dwindled with the lack of proper technology. These optical correlators and optical processors have the same foundation as optical holography as well as many of the same components. By the 1990s, the growth of the silicon microchip industry and the development of new manufacturing processes led to spatial light modulators and charged-coupled device (CCD) cameras that were finally approaching the level required for holographic data storage. Material research proved to be more difficult; however, with many of the other necessary elements in place, research in holographic data storage increased.<sup>10-17</sup> Two university-government groups in particular, the Photorefractive Information Storage Materials (PRISM) and the Holographic Data Storage Systems (HDSS) consortiums, have advanced the state of holography to the point where several commercial ventures are now pending.

Even as these corporate ventures seek to commercialize and bring mainstream holographic data storage, researchers continue to seek out further exploitation of the holographic process. High speed database searches using optical correlation and associative memory retrieval of data, and holographic optical devices such as polarization-discriminating sensors, super-narrow holographic filters, and holographic imaging devices are just a few of the possible future applications for holography.

This thesis documents a portion of the work completed at Northwestern University in Selim Shahriar's Laboratory for Atomic and Photonic Technologies, focusing on four projects: development of holographic materials, creation of a holographic "smart" eye, a polarization-sensing element for visual and non-visual sensors (cameras/LADAR), and narrow holographic filters for optical communications.<sup>18-31</sup>

## 1.2 Holography

Holography has at its roots a very simple concept that is familiar to those versed in basic communications theory: A carrier (reference) signal is modulated with the information contained in an information signal. In a traditional example of this theory, an electromagnetic wave in the ~100 MHz frequency range can be amplitude or frequency modulated (AM/FM) to provide a means of communication (radio). In the case of holography, the information and reference signals are both optical frequency waves. The two waves are directed so that they overlap inside a photosensitive medium. The material is responsive to the intensity of the interference pattern, which depends on the amplitude and phase difference between the two waves.

This process of creating a hologram is illustrated in Figure 1-1. We consider the simple case of no absorption. A signal wave and reference wave interfere coherently at the holographic material. As we will soon see, the key to wavefront reconstruction is the recording of the interference pattern of two beams, the signal and reference. If the two beams are not coherent with respect to each other—if the phase difference between them is not constant with respect to time, the interference pattern will be washed out and no hologram will be recorded.

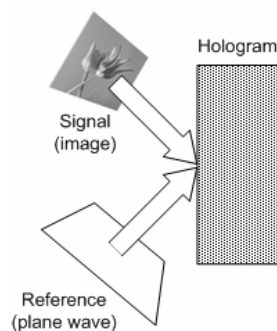


**Figure 1-1: Creating a Hologram**

Writing in complex amplitude notation, the signal wave is  $A_1 e^{i(\omega t - \phi_1)}$  and the reference wave is  $A_2 e^{i(\omega t - \phi_2)}$ , where  $\phi_1$  and  $\phi_2$  are the spatially-varying phase functions of the individual waves. The intensity of the resulting interference pattern is as follows:

$$|A_1|^2 + |A_2|^2 + 2|A_1||A_2|\cos(\phi_1 - \phi_2) \quad (1.1)$$

The first two terms of equation (1.1) are DC (zero frequency) terms and can be ignored. The third term is a cosine proportional to the difference in phase between the signal and reference waves. For a photosensitive medium, the refractive index will be modulated in proportion to the interference pattern in equation (1.1). Re-writing equation (1.1) in complex notation, it is evident that applying the reference wave will reconstruct the signal wave up to a multiplicative constant. For a plane wave reference, this constant will not affect the signal wave.

One way to view the holographic process is via conventional sinusoidal gratings and Fourier signal theory.<sup>32</sup> If one records a hologram of two plane waves interfering, the hologram is simply a diffraction grating with a period equal to the wavelength of the two recording waves divided by twice the sine of the angle between them (for the case of both beams hitting the recording medium from the same side). If this grating is a thin phase grating, it diffracts multiple orders and behaves exactly as a standard sinusoidal grating. If the hologram is recorded in a thick material, the grating obeys Bragg diffraction, and only the first order diffracts efficiently, with the other orders being suppressed.

With this picture in mind, the case of recording a 3D scene is simple to analyze. According to Fourier theory, the light reflected by the image or scene is composed of an infinite sum of weighted plane waves, and the hologram that is created is in fact the superposition of the gratings created by each plane wave component interfering with the reference wave. Thus, the

hologram itself is a superposition of many gratings of varying strengths, periods, and phase shifts. When the proper reference wave is used, it diffracts from all these gratings simultaneously and reconstructs the original image.

Holograms can be characterized by the geometry used to write them as well as by the properties of the recording medium. In general, we will discuss two types of geometries: transmission and reflection; and two types of materials: thin and thick.

A transmission hologram is recorded when both the signal and reference beams are incident on the same side of the holographic medium. In this case, the grating planes will be perpendicular to the surface of the medium. The readout beam is applied to one side of the hologram, and the reconstructed beam exits from the opposite side.

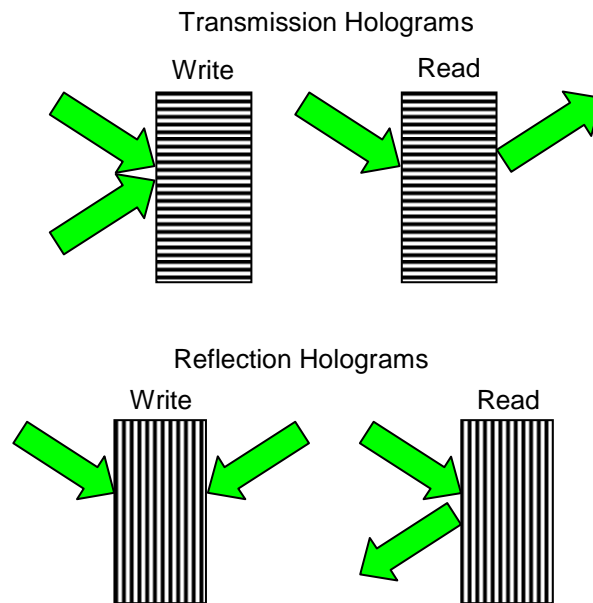


**Figure 1-2: Recording geometries**

Reflection holograms are created when the signal and reference beams are on opposite sides of the holographic medium. The grating planes are now parallel to the surface of the medium, and

when the readout beam is applied, it reflects from the holographic gratings. Figure 1-2 illustrates these two cases.

The thickness of a grating (holographic or otherwise) is usually measured with the  $Q$  parameter as defined in equation (1.2):<sup>6</sup>

$$Q = \frac{2\pi \lambda_0 d}{n \Lambda^2} \quad (1.2)$$

$\lambda_0$  is the free space wavelength,  $n$  is the index of refraction,  $d$  is the effective grating length, and  $\Lambda$  is the grating wavelength. In general, a grating with a  $Q$  parameter of less than 10 is considered to be “thin”, or in the Raman-Nath regime of diffraction. A  $Q$  parameter of greater than 10 indicates a “thick” or “volume” grating that is in the Bragg diffraction regime. The choice of boundary between these two types of holograms is arbitrary, and the change from one regime to the next is gradual.

In thin holograms, the angle used to read the hologram does not affect the diffraction significantly, just as in a thin grating. As the input angle changes, so does the output angle, but the diffraction efficiency is not greatly affected for even moderately large angles ( $\sim 30$ - $40^\circ$ ). For thick holograms, however, this is not the case. The phase matching condition for a thick hologram ensures that only one order of diffraction is diffracted strongly while the other orders are suppressed. Volume holograms thus have very small angle tolerances, typically on the order of  $0.01^\circ$  for a 2 mm thick hologram.

The thickness and angle-tolerance of the hologram plays an important role in holographic optical correlators. Just as one can use the reference wave to reconstruct the signal wave, the signal wave can be used to reconstruct the reference. In fact, this operation is very similar to the mathematical operation of cross-correlation. If an image orthogonal to the original signal image

is used to try to reconstruct the reference beam, no diffraction will be observed. However, if an image is used that correlates in a non-zero way with the image, diffraction will be observed, and the amount of light diffracted will be proportional to the cross-correlation of the test image with the original signal image. For thin holograms, if the Fourier transforms of the images are used instead, the correlation that is performed is translation-invariant. Thus, the test image could be translated in its plane (but not rotated or scaled), and the correlation would still occur. This property is a direct result of the angle tolerance of thin holograms. For volume holograms, the above description is not entirely correct. Although an operation very similar to correlation occurs, there is a departure from the exact correlation operation because of the angle restriction. Also, translation-invariance is reduced as the thickness of the hologram grows, and the correlation output is convolved with a sinc-like function. Depending on the thickness of the hologram and the amount of translation-invariance required, it may still be possible to build a holographic optical correlator using a volume medium.

### ***1.3 Properties of Volume Holograms***

Volume holographic gratings are used in many of the projects described here. Volume holograms can be analyzed using coupled-wave theory or more rigorous coupled-wave analyses.<sup>6, 9, 33-35</sup>

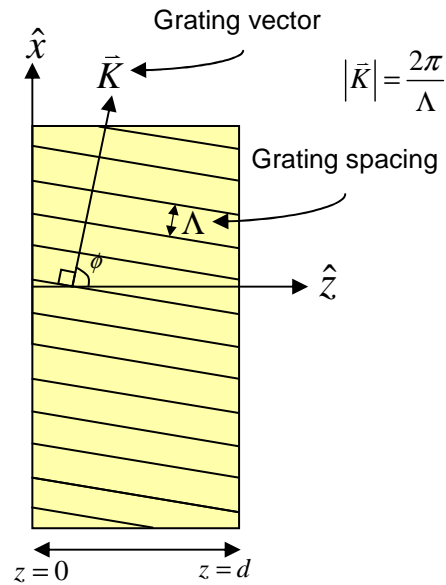


**Figure 1-3: Grating geometry and parameters**

Here we briefly review the properties of interest for volume gratings. Section 10.1 develops the full treatment of thick grating theory for beam combining according to couple-wave analysis. Figure 1-3 illustrates the geometry for a volume transmission grating. The grating vector  $\vec{K}$  is perpendicular to the planes of constant index, and the grating period is related to the magnitude of the grating vector:  $|\vec{K}| = 2\pi/\Lambda$ .

Volume gratings obey Bragg diffraction; that is, there exists a set of constraints on both angle and wavelength such that only a certain combination of angle and wavelength will diffract efficiently from the grating. For example, an unslanted volume hologram written at 532 nm with symmetric writing angles of  $30^\circ$  will diffract strongly only at or very close to that angle and wavelength. The spread in the tolerance of angle and wavelength can be approximated as  $\Delta\theta_{\text{FWHM}} \approx \Lambda/d$  and  $\Delta\lambda_{\text{FWHM}}/\lambda \approx \Lambda \cot\theta/d$ . Thus the thicker the grating, the more selective it is with respect to angle and wavelength. This leads to an important parameter of volume gratings, multiplexed holograms.

## 1.4 Angle-Multiplexing in Volume Holograms

Because thick holograms are angle-selective, one can write multiple holograms in at the same location and volume of the holographic medium by changing the angle of the reference beam before writing each new hologram.<sup>36</sup> In fact, by changing different properties of the reference beam, many multiplexing schemes can be used and even combined. Changing a geometric parameter such as angle or rotation is one possibility, but one can also change the writing wavelength or choose to encode each reference beam with a specific orthogonal phase pattern. Here we will use almost exclusively angle-multiplexing, though other methods could be substituted or combined with this scheme.

Construction of an angle-multiplexed grating in one dimension is shown in Figure 1-4. The first image is written with a reference beam at a specific angle.

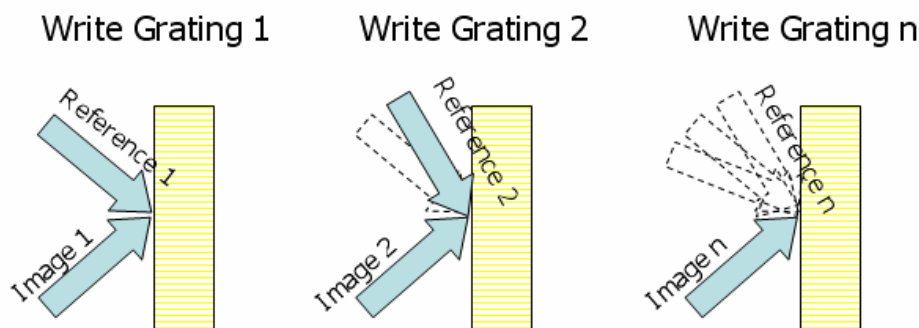


**Figure 1-4: Writing an angle-multiplexed grating**

To write the next image, the angle is changed slightly. This process is repeated until all the holograms are written. The angular bandwidth of the hologram, as discussed above, determines the amount of angle change necessary to ensure crosstalk does not occur. The number of holograms that can be multiplexed in a single spatial location is limited by the dynamic range and scattering properties of the recording medium. As many as 10,000 holograms were stored in

a single location in  $\text{LiNbO}_3$ ,<sup>37</sup> and 1000-2000 holograms have been stored in a single spatial location in photopolymer materials.<sup>38</sup> These parameters will be discussed in further detail in Chapter 2.

Readout of angle-multiplexed holograms is shown in Figure 1-5.

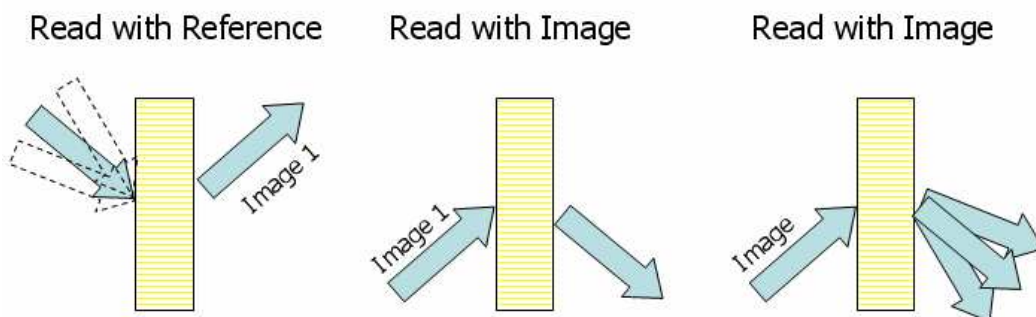


**Figure 1-5: Reading an angle-multiplexed grating**

By choosing a specific angle for the reference beam, a particular image can be read out. In addition, reading with a specific image will reproduce the reference beam propagating at the angle with which that image was written. If an arbitrary image is used, an operation mathematically very similar to cross-correlation will take place, and any image that matches the input image will generate a reference beam at that angle with an intensity proportional to the correlation.

## 1.5 Conclusion

This chapter is meant to familiarize the reader with many of the concepts that are used here, but is by no means a comprehensive review of holographic data storage or holography in general. The excellent books *Holographic Data Storage* and *Practical Holography* serve as a foundation for research into data storage and visual holography, respectively.<sup>39, 40</sup>

## 2 Holographic Materials Development

### 2.1 Introduction

The idea for the hologram was developed by Dennis Gabor in 1948.<sup>1</sup> By 1962, Leith and Upatnieks had used communications theory to create off-axis holograms,<sup>41</sup> and during the early 1970s, angle-multiplexing was used for holographic data storage.<sup>7</sup> However, in the intervening time period no holographic data storage system has been brought to market.

Although many factors are responsible for this, arguably the largest is the lack of suitable materials. The computer and electronics revolution in tandem with the huge growth of optical fiber based communications has led to quick progress in the technology to control and detect light, two of the three necessary components of a holographic data storage system. The final key to a viable holographic data storage system or optical information processing system is a means to store data, both in a permanent and a temporary/re-writable fashion.

Many types of materials have been proposed and developed as candidates to solve this problem, and although advances in the last two decades have brought the possibility of success even closer, the problem is not yet solved. In this chapter, I will first discuss the qualities that are needed in a holographic material. The more serious reader should refer to reference 39 for more detail. I will then review briefly the types of materials that have been tried to date, and finally I will detail our experiments over the past five years with a specific class of material, the photochromic polymer, including a technique we helped develop to determine quickly the  $M_{\#}$ , an important figure of merit for holographic materials.

## 2.2 Material Parameters

The parameters of holographic materials are defined here. Certain applications place more or less emphasis on a particular material characteristic depending on their needs. One of the most important parameters of a holographic system, whether it is for data storage, information processing, or even for a specialized holographic optical element, is the diffraction efficiency. The diffraction efficiency is a measure of the amount of incoming light that is diffracted into the output beam. It is defined as:

$$\eta = \frac{I_d}{I_d + I_t} \quad (2.1)$$

where  $I_d$  is the intensity of the diffracted light, and  $I_t$  is the intensity of the transmitted light. Although the diffraction efficiency is not strictly a parameter of the material, there are several properties of an optical material that affect the maximum possible diffraction efficiency.

The scattering ratio for an optical medium defines the amount of light that is scattered incoherently by the medium. If the diffraction efficiency of a hologram is low enough that the diffracted intensity is smaller than the amount of scattered light, then that hologram is effectively useless because no detector can resolve the diffracted light from the scattered light. In effect, the scattered light adds to the noise floor of the detector. In addition to having a low scattering ratio, a good optical medium should be able to be polished or molded so that it has very flat surfaces for interfacing with optical beams. When an optical wavefront is incident on the surface of a material, any pits or bumps in the surface will create a phase difference in the wavefront at that point. This wavefront distortion leads to increased errors in storage and readout. The scattering ratio and surface quality (sometimes referred to as the scratch/dig number) can be described for any optical material, and as such are not specific to holographic materials. Systems that use a

photosensitive material bonded to a glass substrate, for instance, would need to take into account the optical properties of the glass used.

The sensitivity of a holographic material is similar in nature to the concept of sensitivity for photographic applications. A more sensitive holographic material will have stronger gratings, or holograms, than a less sensitive material given the same amount of recording light. The sensitivity is typically defined for holographic data storage applications as the amount of diffraction efficiency achievable for a certain exposure fluence:

$$S = \frac{\sqrt{\eta}}{It} \quad (2.2)$$

$I$  is the intensity of the recording light, and  $t$  is the exposure time. For data storage applications, the individual holograms are usually weak because there are so many multiplexed in one location. For weak holograms, the diffraction efficiency  $\eta$  is proportional to a constant times the index modulation, or modulation depth. In other words, the square root of the diffraction efficiency is directly proportional to the amount of index variation of the hologram. Thus, equation (2.2) is simply the amount of index variation achieved for a certain recording energy (fluence).

The sensitivity of a material is intrinsically linked to the absorption. This makes intuitive physical sense: when the material is very sensitive, it will quickly absorb light, while an insensitive material will not be able to utilize as much light, and so allow more to pass through. As a material is made thicker, the effects of absorption force a reduction in sensitivity. The tradeoff between the two must be analyzed for each individual application.

When writing more than one hologram in the same volume of space (spatial location), known as multiplexing or co-local storage, the key figure of merit is the  $M_{\#}$ . The  $M_{\#}$

(pronounced m-number) is a measure of the total dynamic range of the material.<sup>14, 27, 31, 42</sup> The  $M_{\#}$  is defined as the sum of the square roots of the diffraction efficiencies of all the holograms that can be written in a single spatial location. In other words, if enough holograms were written in one spatial such that all the sensitivity (dye or photosensitizer) in the material was used up and no further holograms could be recorded, then the sum of the square roots of the diffraction efficiencies of those holograms would add up to be the  $M_{\#}$ :

$$M_{\#} = \sum_{i=1}^M \sqrt{\eta_i} \quad (2.3)$$

The  $M_{\#}$  can be used to determine the diffraction efficiency of a single grating:

$$\eta = \left( \frac{M_{\#}}{M} \right)^2 \quad (2.4)$$

In these equations  $M$  is the total number of holograms that are multiplexed, and  $\eta$  is the diffraction efficiency of a single hologram. As we see from equation (2.4), the higher the  $M_{\#}$ , the greater the number of holograms one can multiplex in a single location, leading to higher storage densities. Alternatively, with a higher  $M_{\#}$  and the same number of holograms  $M$ , greater diffraction efficiency for each grating is possible. Another way of viewing the  $M_{\#}$  is that it represents the maximum possible index modulation available. That is, the gratings in a holographic material are formed by a change in the refractive index of a material. The amount of change is called the index modulation, and the maximum value is directly proportional to the  $M_{\#}$ . The idea of the  $M_{\#}$  is particularly important for holographic data storage for these two reasons, and this idea is expanded upon in Section 2.7.

There are several engineering concerns for the material. It should be easily formed into useful shapes; for instance, a CD-ROM sized disc, or a square “coupon”. The material should be

able to be formed into any desired thicknesses, sometimes up to half a centimeter or more.

Also, some materials exhibit a change of dimension during recording or material post-processing, commonly referred to as shrinkage. This can lead to data reconstruction loss, and so a low shrinkage is desirable. This material shrinkage causes the grating periods of the holograms stored in the material to change as well. Shrinkage should ideally be kept under 1% to ensure no effect on the read out of the gratings. A material should be able to store the data for as long as required, so overall material stability is also a requirement. Finally, some applications require a material that is erasable and re-writable. In this case, the material should have good data fidelity while storing data and quick erasure so that re-writing is as quick as possible.

As mentioned previously, there is no single material that meets all of the above requirements. To date, much work has been done with two classes of materials: photorefractives and photopolymers.

### ***2.3 Photorefractive Materials***

When two coherent laser beams interfere inside a photorefractive crystal, light frees up trapped electrons from the illuminated regions, which then migrate through the crystal lattice and are again trapped in the adjacent dark regions. This migration creates a space-charge pattern similar to the interference pattern. The spatially-varying electric field thus modulates the refractive index of the crystal through the electro-optic effect. The spatial variation of refractive index results in the formation of a volume phase hologram. Typically, this material has resolution of about 1500 lines/mm. The hologram can be erased by uniformly illuminating the crystal, permitting the crystal to be recycled almost indefinitely. In this material, the optical

readout of the stored information is destructive. Nondestructive readout is possible by a complex thermal fixing of the hologram after recording.

This material has several key disadvantages. First, the sensitivity is quite low - of the order of  $103 \text{ mJ/cm}^2$ . Second, the maximum diffraction efficiency of the photorefractive crystals is about 25-30%. Third, the diffraction efficiency is very small at wavelengths longer than the visible range. Photorefractive crystals are also reasonably expensive, and it is difficult to grow good, optical quality, defect-free crystals. The addition of dopant materials to the crystal structure can enhance the properties of these photorefractive crystals, but at present their volatility and the deficiencies listed above leave them short of ideal for holographic data storage.

## **2.4 Photopolymer Materials**

A number of organic materials are known to exhibit photopolymerization or photoreaction in the presence of a photosensitizer when excited with an appropriate light source. These photochemical reactions can induce refractive index modulations resulting in phase holograms with high diffraction efficiency and angular selectivity. DuPont (HRF-600X001, OmniDex, HRF-150-38)<sup>43-47</sup> and Polaroid (DMP 128)<sup>48</sup> photopolymers have been designed primarily for display holography and are currently the most commonly used photopolymers for thin holographic recording.

The Dupont photopolymer films consist of monomers, polymeric binders, photoinitiators, and sensitizing dyes. Upon exposure, the sensitizing dye absorbs light and interacts with initiators resulting in photo-induced polymerization and cross-linking of the monomer. Further UV curing and baking processes lead to the polymerization of the residual monomer and an enhancement of the refractive index modulation. All these processing steps can introduce

thickness variations (shrinkage) in the holographic film. An immediate consequence of this thickness variation is the deviation of the input reconstruction angle from the original recording angle. A deviation up to  $2.5^\circ$  has been experimentally reported for DuPont photopolymer film HFR-150-38. This angular deviation creates very severe technical problems while recording angular multiplexed thick holograms. Diffraction efficiencies as high as 95% have been attained for the DuPont OmniDex photopolymer. Sensitivity and maximum spatial resolution for this photopolymer are  $30 \text{ mJ/cm}^2$  at  $514 \text{ nm}$  and  $5000 \text{ line/mm}$ , respectively.

The Polaroid photopolymer system, DMP 128, utilizes dye sensitized photopolymerization of a vinyl monomer incorporated in a polymer matrix coated on a glass substrate. Post-processing involves a uniform exposure to white light followed by a developer/fixer bath. Diffraction efficiencies up to 95% are obtained with exposures of  $4\text{-}10 \text{ mJ/cm}^2$ . Holographic images recorded in this photopolymer have a moderate spatial resolution of about  $5000 \text{ lines/mm}$ . The high diffraction efficiencies achieved are attributed to the high index modulation due to the formation of alternate solid and porous regions in the processed films. The pores created during the processing have to be filled with an index matching material, normally a viscous fluid, to achieve stable holograms. The physical and optical properties of the holograms are significantly changed by filling. The filling causes a reduction in the refractive index modulation and an increase in the average refractive index of the hologram. The reduction in index modulation effectively reduces the diffraction efficiency and the increase in the refractive index of the hologram alters the incident angle and the optimum wavelength of the readout.

Polaroid recently spun off their holographic materials division as Aprilis, which has developed a cationic-ring opening photopolymer (CROP) material in disc and coupon form up to

400 microns thick.<sup>49, 50</sup> It has an  $M_{\#}$  of about 6.5 at this thickness with very high sensitivity and low shrinkage.

Recently, the Lucent Technologies spin-off InPhase introduced their own photopolymer, whose recording mechanism (diffusion and polymerization of monomer molecules) and performance closely matches that of DuPont or Polaroid. The  $M_{\#}$  of Lucent's photopolymer has been reported as high as 42.<sup>51</sup> InPhase is reportedly close to bringing to market a holographic data storage system based upon this material, with a thickness of 1.5 mm.

## ***2.5 Northwestern Dye-doped Photopolymer Material***

Our material is a quinone-doped polymethyl methacrylate (PMMA) which is essentially light-sensitive plexiglass. This polymeric material uses the novel principle of polymer with diffusion amplification (PDA). Exposure of this material to light results in the writing of two out-of-phase periodic holographic structures that partially compensate each other. One of these is formed by a concentration distribution of dye molecules attached to the PMMA, while the other is formed by the migration of free radicals. As a result of diffusion of the free radicals, one grating degrades over time, and the efficiency of the other grating is amplified without additional processing. The surviving grating is stored in the molecules attached to the PMMA matrix, and these molecules do not diffuse. Because the photosensitive dye molecules simply attach to the host polymer matrix to cause the refractive index change, the overall dimension of the material changes very little upon exposure and development, leading to very low shrinkage. The material is formulated as a liquid monomer and so a mold can be used to create samples in almost any size or shape. Also, being a type of plexiglass, it is very strong and durable as well as being relatively cheap.

We have been developing our material for two general applications. The first is for holographic data storage and information processing applications. For this purpose, the goal is a large area substrate with a thickness of 2 mm. The material should have a high  $M_{\#}$  and good sensitivity. The second application is highly-selective holographic filters and holographic beam combiners. This application is reviewed in more detail in Chapter 3, but in brief, a very thick holographic grating can act as a wavelength filter with a very narrow bandwidth and also as a beam combiner. In these cases, only a few gratings will be multiplexed in one location, and many times only a single grating is necessary. In this case, the more important factor is absorption and achievable thickness.

Both types of material share the same formulation, and then are processed in different ways. The host polymer is made from 10% by weight solid PMMA added to the liquid monomer. This mixture is stirred at an elevated temperature until the liquid is supersaturated and clear. At this point, the photosensitive dye, phenanthraquinone (PQ), is added to the mixture. The amount of dye varies with the type of material used. For the 2 mm thick wide-area plates, more dye is desirable to achieve higher  $M_{\#}$  and sensitivity. For the thick grating application material, the long interaction length inside the material dictates less dye so that absorption does not dominate the recording process. After the dye is added, the mixture is stirred until it is fully integrated. The final step is the addition of an initiator, azobisisobutyronitrile (AIBN), to aid the polymerization process. Once the mixture is homogenous, the solution is poured into the mold used for the specific application that is being targeted. The mixture is then baked until solid, at which point the substrate is ready for use. The solution and substrate are kept in light isolation from the point at which the dye is first added to the mixture until the material has been fully used, at which point it is no longer sensitive to light.

## 2.6 Experimental Development

### 2.6.1 Preliminary Experiment

The initial tests for the NU material were done using a two-piece Teflon mold. Two optical flats with a surface flatness of  $\sim \lambda/5$  were held in place inside the mold and screws were used to press the two halves of the mold together. However, the design of the mold was such that it was very difficult to separate the two halves without damaging either the material or the optical flats. Nevertheless, the first tests were done, and a preliminary baking schedule and material composition were determined. These results are shown in Table 2-1:

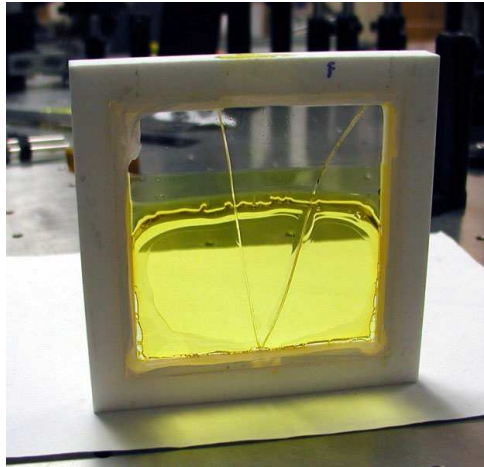
	Material Composition	Temperature (°C)	Time (hours)
Liquid MMA	50 g	70	6
PMMA	5 g	120	2
PQ Dye	0.5-0.7% by wt.	20	8
AIBN	0.5% by wt.		

Table 2-1: Preliminary Holographic Material Recipe

### 2.6.2 Large Area Holographic Plate

These results were used in the first attempt at a holographic plate. The mold in Figure 2-1 was the first prototype for a 4" by 4" square piece of material. The mold was made to specification by the machine shop, and optical quality glass was ordered from Precision Glass & Optics in Santa Ana, CA. The mold held two glass flats 2 mm apart, and Teflon tape was used along the edges of each flat to ensure that when pressed into the mold they would seal. It was found that leakage still occurred, and electrical or paper tapes were used to seal the edges as

well. In this attempt, clamps were used to try to keep the glass flats pressed together in a seal. This pressure plus the material expansion resulted in one of the glass flats cracking. Electrical tape was used in all future attempts to seal the sides and bottom. A slit along the top of the mold allowed the material to be poured in while in the liquid state, and could be covered or left open depending on whether or not it was desired to allow the material to interact with the environment. This material was baked up to 120°C which led to the patterns around the edges of the material.



**Figure 2-1: First holographic plate attempt**

Although one of the glass flats cracked, there was enough room to perform experiments with this sample. 45 gratings were written in a single spatial location using angle-multiplexing using the same exposure for each grating. The diffraction efficiency of these gratings was then measured. The sum of the square root of these efficiencies is plotted in Figure 2-2. The figure shows a linear growth in  $M_{\#}$  versus hologram number (exposure).

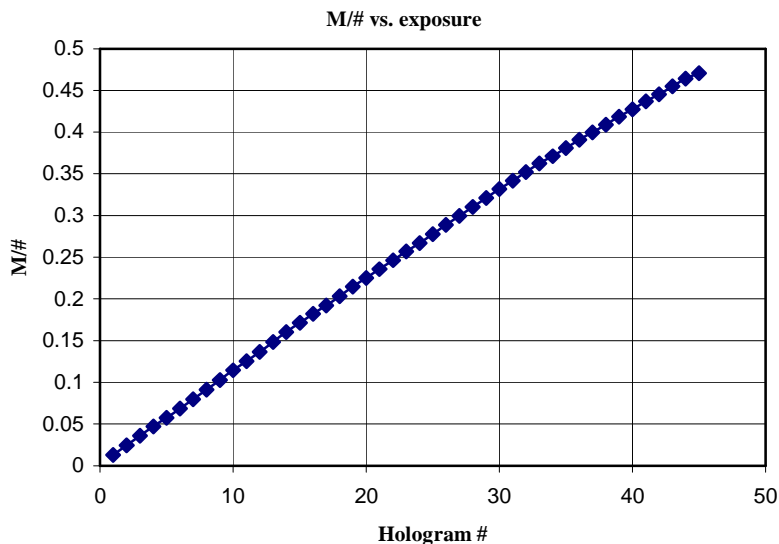
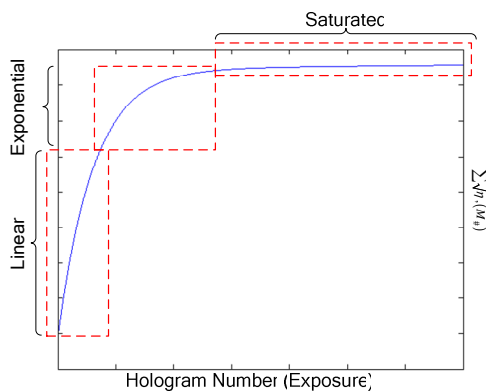


Figure 2-2:  $M_n$  for first 4"x4" sample

A typical material will exhibit three stages of recording dynamics. The first is the linear growth stage, during which equal exposures will result in roughly equal strength holograms. The second stage is the exponential stage, where an exponentially-growing fluence is necessary to record holograms of equal strength. At this point, the photosensitive part of the material is mostly used, and it requires more and more energy to activate. Finally, the material saturates when all the photosensitizer is used up. At this point no amount of additional light will create a hologram. These three zones are shown in Figure 2-3.



**Figure 2-3: Typical Material Response Curve**

Comparing this figure to the data collected in Figure 2-2, we can surmise that the recording took place entirely in the linear regime, and thus the material was not exhausted when recording stopped. Because of this, an estimation of the  $M_{\#}$  for this sample is not possible.

A second sample was made using the same process except with no clamps so that the glass would not crack. This attempt was successful and the resulting sample is shown in Figure 2-4. The sample is 3"x4" and has good optical clarity throughout. The temperature schedule that was used is shown in Table 2-2. It was necessary to ramp the material up to temperature at a very moderate rate to avoid bubble formation in the sample as well as to prevent cracking in the optical flats.

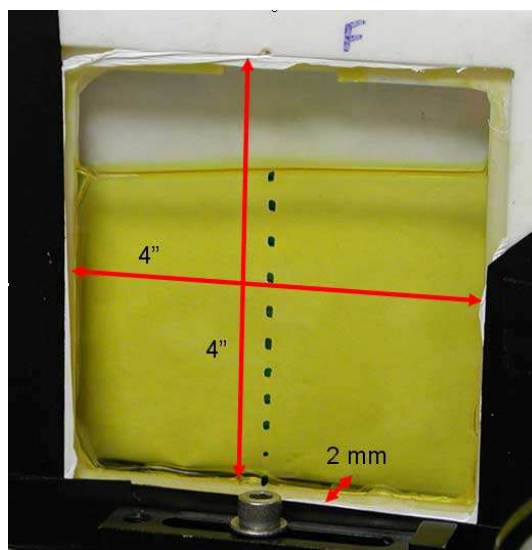


**Figure 2-4: Second 4''x4'' sample**

Temperature	Time	Action
(°C)	(hr)	
30	1	Ramp

30	24	Hold
35	2	Ramp
35	8	Hold
45	4	Ramp
45	24	Hold
20	12	Ramp

**Table 2-2: Baking schedule for 4"x4" sample**

The first test using this sample was to record a high-resolution image as a hologram inside the material. The laboratory setup for this experiment is shown in Figure 2-5. A beam from the 5.5 W Verdi laser was expanded and collimated using a pair of lenses. This expanded beam was then split by a polarizing beamsplitter cube. Part of the beam passed through the cube and was directed to a stage where the holographic substrate was held in place. The final pair of mirrors directing this reference beam was a pair of rotating galvanometric (galvo) mirrors, so that by rotating the two in tandem, the angle of incidence of the beam could be changed without changing the point of incidence at the material. In this case, a single image was written so no angle-multiplexing was performed (the galvos remained in position the entire time). Meanwhile the other part of the beam was reflected off of the spatial light modulator (SLM) and through a  $4f$  imaging system to the material.

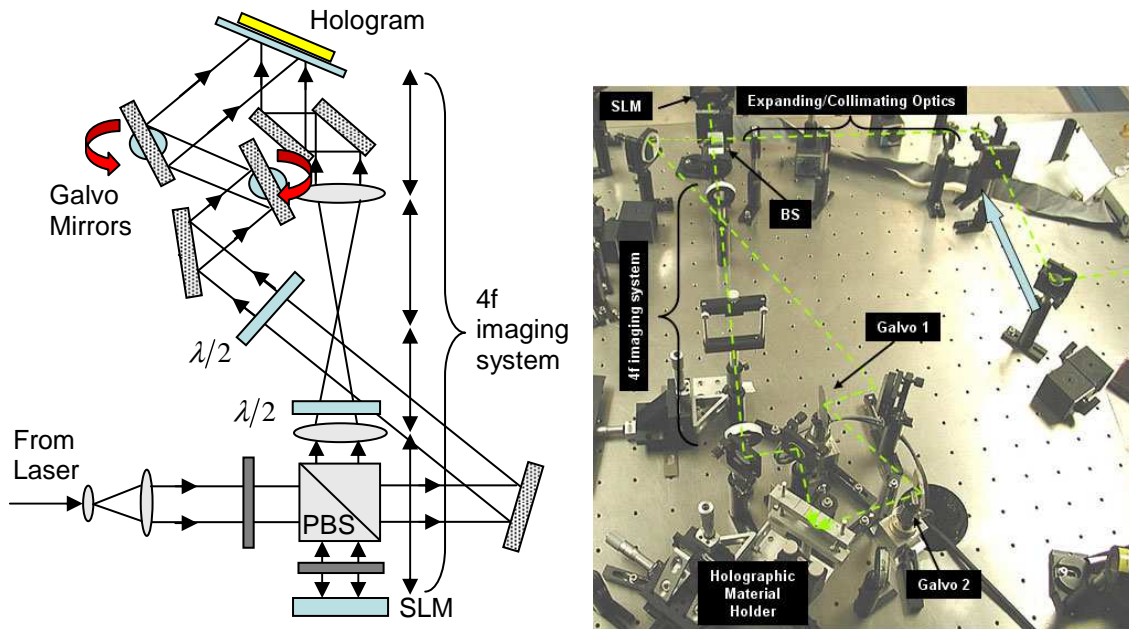


**Figure 2-5: Angle-Multiplexing Laboratory Setup**

The 4f system is used to image the plane of the SLM face to the holographic material. This ensures that diffraction effects will not play a factor in degrading the image quality (see Appendix 10.3). The SLM used was a 512 by 512 pixel device from Boulder Nonlinear Systems (BNS) in Colorado. Using a Pulnix CCD camera, the image at the plane of the hologram was captured and compared to the image captured upon readout from the hologram itself.

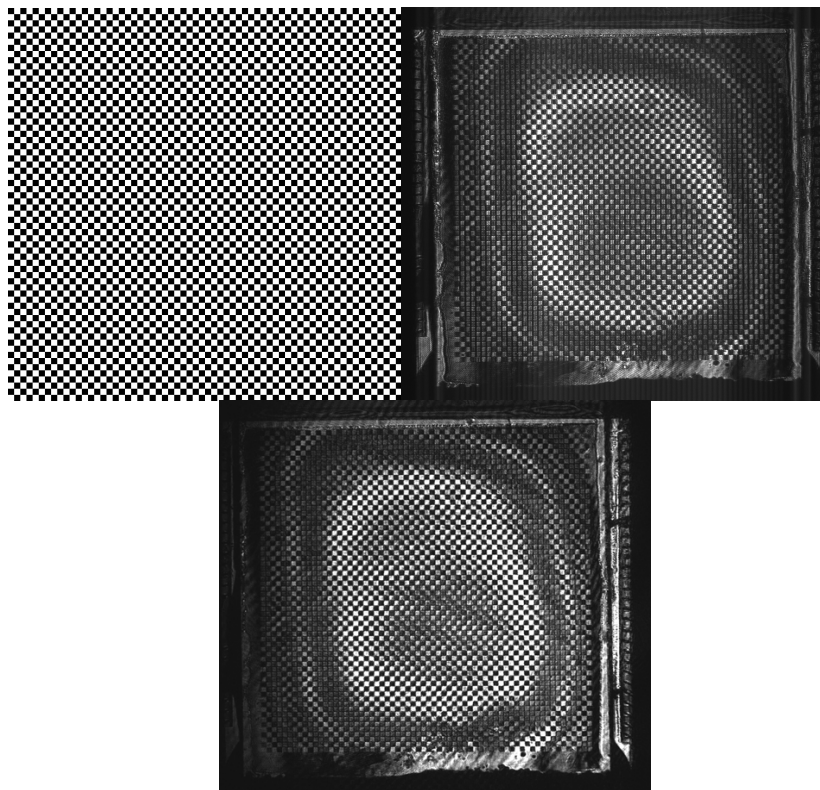


**Figure 2-6: Comparison of SLM image (left) and hologram image (right)**

Figure 2-6 displays these two images along with the original bitmap. The SLM image is on the top right, and the image from the hologram is on the bottom. They are virtually identical, illustrating that we can store very high quality images in our 4"x4" plates. The distortion present in both images is a result of the quality of the polarization optics that were used in conjunction with the SLM, as well as a general distortion that was present in the SLM at the time of the experiment and that has since been fixed. The Boulder Nonlinear Systems SLM operates as a voltage-controlled waveplate in reflection mode. A specially constructed baseboard allows the application of a different voltage at each pixel in the device, which in turn controls the phase retardation of the liquid crystals at each pixel. An incoming linearly-polarized beam must first be rotated into the frame of the optic axis of the SLM by a half-wave plate. This ensures that the SLM can apply both the maximum and minimum retardation and serves as a contrast control.

Once rotated into the proper frame, the light reflects from the SLM face and is phase-retarded at each pixel according to the applied voltage. The retardation difference between the maximum and the minimum phase shift is equivalent to a half-wave shift. When the reflected beam passes back through the polarizing beamsplitter (PBS), an image-bearing beam is the result, as the negative of the image that was on the SLM face is rejected by the PBS. Any nonlinearities in the half-wave plate, PBS, or SLM cause distortion in the images. In this case, the half-wave plate was non-uniform, with a pattern similar to Newton fringes on it. This causes the distortion seen above, as parts of the image are fully rotated into the frame of the SLM, while other parts are not and thus are low or opposite contrast.

To test the capabilities of the material for holographic data storage, 80 images were multiplexed in a single location using angular multiplexing. The experimental setup was identical to that described in Figure 2-5. Several of the images from the 80 that were stored are shown in Figure 2-7.

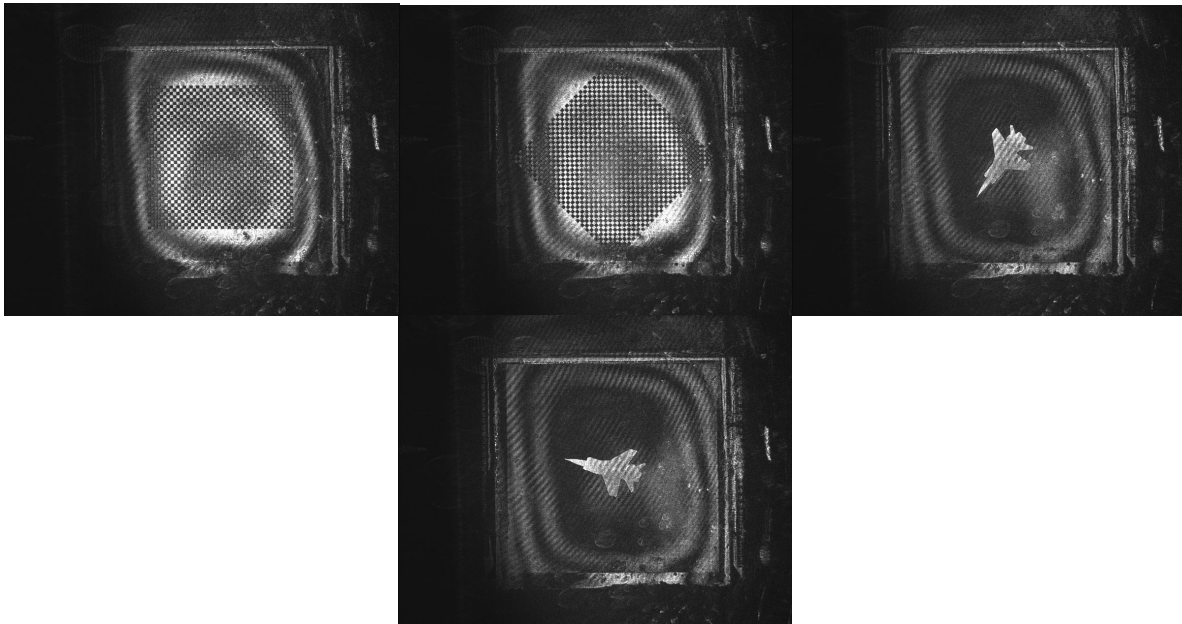


**Figure 2-7: A selection from the 80 multiplexed images**

The images show the same ring-like distortion from the optics but otherwise are of a good quality. The images on the left are from among the first recorded, and the images on the right are from the last. There is no loss in quality or efficiency between them, indicating that many more than 80 could have been multiplexed.

### 2.6.3 Thick Material

At the same time as the first holographic plate was being developed, the first successful attempts at making an extremely thick material occurred. The previous attempts had been plagued by the formation of bubbles from residual gasses of the polymerization reaction. These bubbles would form and would then, because the material quickly becomes viscous when heated, be trapped as the material hardened, resulting in unusable substrates.



**Figure 2-8: First thick material successes**

Figure 2-8 shows the molds for the thick material that were made by the glassblowers at the Northwestern University machine shop. Although optical quality glass was used, the shop did not have the technology to assemble the four sides properly parallel to each other, and the molds were prone to distortion from the heat used to join them together. The material process involves the shrinking of the polymer from evaporation and the natural shrinking that occurs as the polymerization takes place. This is the reason the molds appear to not be fully filled. As the

process continues, the polymer hardens and tends to expand enough to crack the molds. For the samples shown in Figure 2-8, the process had been refined enough to get properly transparent material with dye (no bubbles). The differing colors of the samples are the result of tests of different amounts of dye.

By obtaining a strengthened cell from the machine shop, we were able to create a sample with dimensions of 1.5 cm square with a depth of 1.3 cm. This sample is shown in Figure 2-9 and has good optical clarity in the center.



**Figure 2-9: 1.5x1.5x1.3 cm sample**

Further development of this technique resulted in a 3.8 cm by 1.7 cm cell with sufficient depth for recording. A grating was recorded in this sample using 532 nm light, written for readout using a wavelength-tunable Coherent dye laser. Figure 2-10 illustrates the result of the frequency scan using the dye laser.

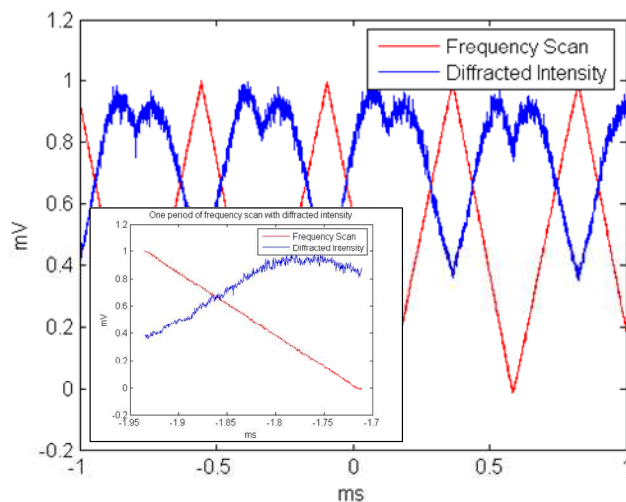


**Figure 2-10: Result of dye laser frequency scan**

The hologram was mounted on a stable platform, and the dye laser was set to 590 nm and Bragg angle-matched to the grating. The dye laser was set to scan at its maximum width, which was 29.999 GHz. The inset picture in Figure 2-10 shows the material response to one full scan. Fitting this data to an exponential distribution, we can estimate the full-width half-maximum (FWHM) bandwidth to be 40 GHz. The diffraction efficiency was measured to be 14.6%. Further work in developing narrow holographic filters can be found in Chapter 3.

The idea of a PMMA-based dye-doped photopolymer material for holographic materials was originally proposed and studied by Veniaminov at the Vavilov Optical Institute.<sup>52-56</sup> Further development has continued at Northwestern University under Shahriar<sup>22, 23, 27</sup> as well as at the California Institute of Technology<sup>57, 58</sup> and at the National Chiao Tung University (NCTU).<sup>59-61</sup> The work done at Caltech and NCTU suggests that this material behaves differently depending on the baking schedule used to set the polymer. One possible process uses a maximum temperature of 45°C, while the other reaches 80°C. The difference in temperature results in a different amount of PMMA and MMA groups left in the material. When the recording light

interferes inside the material, the photo-activated PQ dye groups have a preference for attaching to MMA groups rather than PMMA groups. This tendency, along with the difference in the amount of PMMA and MMA between the two methods, results in different post-processing dynamics.

In the material that was baked to 80°C, there is a very small amount of MMA, and so most of the PQ dye attaches to the PMMA matrix. The result is the dynamics described previously; namely, there are two gratings formed, one by the attached dye and the other grating formed by the absence of dye that has been activated, which is exactly out of phase with the first grating. This leads to a very weak initial diffraction efficiency as the two gratings negate each other. Once baked for a period of time, the un-activated dye can diffuse evenly, destroying the out-of-phase grating and amplifying the desired grating.

In material that has only baked to 45°C, there is an abundance of MMA groups. Upon interaction with light, the dye molecules tend to attach to these MMA groups, creating a very strong grating. However, during baking the MMA-PQ groups can also diffuse, so that baking actually degrades these types of gratings, instead of amplifying them. Depending on the desired application, either method may be chosen. The former type are more stable; however, the latter are much easier to mold into thicker gratings.

The thick grating that was written for use with the dye laser was initially baked to 45°C before recording. After recording and testing, it was baked for 4.5 hours at 45°C. The diffraction efficiency dropped from a maximum of 28% to 2.72%. This drop in efficiency is expected given the previous analysis.

The final improvement to the development of thick gratings was the use of a new optical cell as the mold. Type 3 fluorometer cells from Starna Cells were used. They have optical

quality sides all around, and dimensions of 12.5 mm x 42.5 mm x 45 mm. A sample created in one of these cells is shown in Figure 2-11.

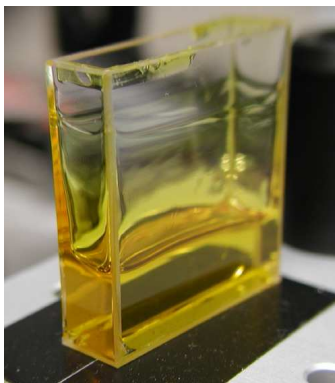


**Figure 2-11: Sample created in fluorometer cell**

These cells were used to create a set of holographic filters, and the details can be found in Chapter 3. Although the fluorometer cells have optical quality glass on all sides, as well as stable rectangular dimensions, there can be scattering from the joints and corners of the cell. In an attempt to gauge the impact of this scattering, a container cell was built and filled with index-matching fluid. In this manner, the optical beams would only interact with one air-glass interface. The glass-material interface is still present, but the index of refraction difference between these two materials is quite small, and so the effects of scattering can be tolerated. The experimental index matching setup is shown in Figure 2-12.

The development of a thick photopolymer material has reached the stage where consistently useable samples can be constructed. Future development should move towards a fabrication method that would allow the samples to be removed from their molds easily. In addition, modification of the dye profile (apodization) will allow the creation of better holographic filters.

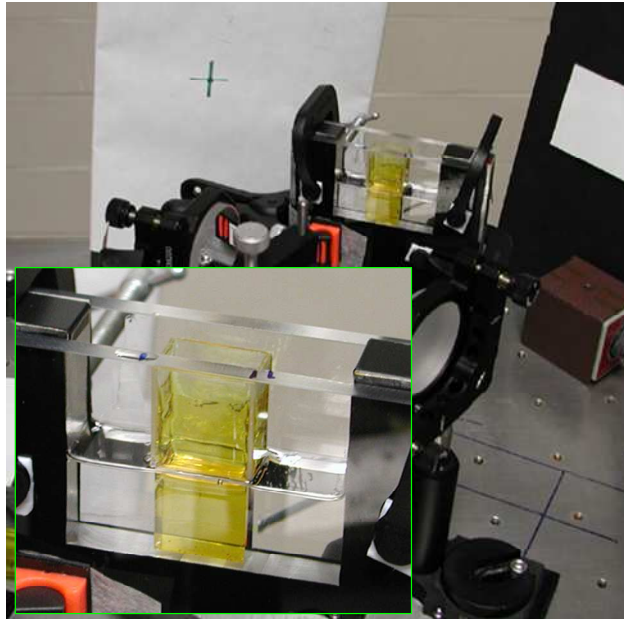


Figure 2-12: Index matching setup

## 2.7 A Simple Technique for Determining the $M_{\#}$

The dynamic range of a holographic medium is an important parameter in determining the storage density and diffraction efficiency for holographic memory systems and holographic beam combiners (1-4). In these applications, many holographic gratings are multiplexed in the medium at the same spatial location. The  $M_{\#}$  is a parameter that defines the dynamic range of the holographic medium; it is essentially  $\pi/2$  times the ratio of the maximum achievable index modulation and the index modulation corresponding to a unity diffraction efficiency grating. The existing techniques<sup>14</sup> to measure the  $M_{\#}$  require one to write many holograms on the material. In this section, I discuss a potentially simpler technique to determine the  $M_{\#}$  for a holographic recording material and present simulated and experimental results for a photopolymer-based holographic recording medium.

Typically, illumination of a holographic substrate with a spatially periodic, sinusoidal intensity pattern produces a periodic index modulation  $n(x) \equiv n_o + n' \cos(Kx)$

where  $n_o$  is the spatially averaged index of refraction of the medium,  $n'$  is the index modulation depth, and  $K$  represents the wave number of the grating. When a laser beam of wavelength  $\lambda$  illuminates this grating at the Bragg angle, the diffraction efficiency  $\eta$  is given by:<sup>6</sup>

$$\eta = \frac{I_d}{I_o} = \sin^2 \left( \frac{\pi n' \alpha d}{\lambda} \right) \quad (2.5)$$

where  $I_o$  is the input intensity,  $I_d$  is the diffracted intensity,  $d$  is the thickness of the substrate, and  $\alpha$  is the obliquity factor determined by the orientation of the grating. A characteristic scale for the index modulation is  $n_c \equiv \lambda / (2\alpha d)$ , so that  $\eta$  becomes:

$$\eta = \sin^2 \left( \frac{\pi n'}{2 n_c} \right), \quad \eta = 1 \quad \text{for} \quad n' = n_c \quad (2.6)$$

In many situations the modulation depth (4) can be modeled as

$$n' = n_m \left[ 1 - \exp \left( -\frac{t}{\tilde{\tau}} \right) \right] \quad (2.7)$$

where  $t$  is the exposure time,  $\tilde{\tau}$  is a time constant that depends on the material sensitivity and the intensity of the writing laser beams, and  $n_m$  is the maximum index modulation. A convenient way to quantify the value of  $n_m$  is through the use of the  $M_{\#}$ , which can be defined as

$M_{\#} = (\pi n_m) / (2n_c)$ . For notational convenience, we define a scaled version of this expression:

$$Q \equiv \frac{n_m}{n_c}, \quad \text{so that} \quad M_{\#} = \left( \frac{\pi}{2} \right) Q \quad (2.8)$$

When  $Q$  is an integer, it represents essentially the maximum number of orthogonal, unit diffraction efficiency gratings that can ideally be written in a given spatial location.

Consider a situation where  $N$  equalized diffraction efficiency gratings are multiplexed on a single substrate using the Bragg (angle or wavelength) orthogonality condition. For  $N \gg Q$ , the diffraction efficiency for each grating can be approximated by  $\eta \equiv \left(\frac{\pi^2}{4}\right) \left(\frac{Q}{N}\right)^2$ . More generally, if the diffraction efficiencies of the gratings are not identical, it is possible to define and measure the  $M_{\#}$  of the material from the relation:

$$Q \approx \sum_{i=1}^N \sqrt{\eta_i}, \quad \eta_i \ll 1 \quad (2.9)$$

Although one can measure the  $M_{\#}$  using one exposure for certain cases, in general to measure the  $M_{\#}$  using this approach may require one to write many holograms. As an alternative method, one can also use the fact that the diffraction efficiency of a single grating in the small index modulation limit is a quadratic function (to a first order) of the exposure time, described by:

$$\eta(t) \approx Q^2 \left(\frac{t^2}{\tilde{\tau}^2}\right) \left(\frac{\pi^2}{4}\right) \quad (2.10)$$

which follows directly from equations (2.6), (2.7), and (2.8). The  $M_{\#}$  can thus be determined from the curve that defines the diffraction efficiency of a single hologram as a function of exposure time. This method also requires recording many successive holograms with different exposures on the holographic substrate.

In this paper, we offer a potentially simpler approach to determine the  $M_{\#}$  from a single recording on the holographic medium. To illustrate this method, we first combine equations (2.6) and (2.7) in order to express the diffraction efficiency as a function of time:

$$\eta(t) = \sin^2 \left[ \frac{\pi}{2} Q \left[ 1 - \exp\left(-\frac{t}{\tilde{\tau}}\right) \right] \right] \quad (2.11)$$

Now, according to the generalized optical pumping model,<sup>31</sup> the saturation rate ( $\tilde{\tau}^{-1}$ ) depends

linearly on the intensity of the radiation for writing the grating:  $\tilde{\tau}^{-1} = \beta \tilde{I}$ , where  $\beta$  is the sensitivity of the medium, and  $\tilde{I}$  is the amplitude of the intensity modulation defined as:

$$I \equiv \tilde{I}(1 + \cos(\mathbf{K}_G \cdot \mathbf{x})) \quad (2.12)$$

with  $\mathbf{K}_G$  being the grating vector. For typical values of  $\tilde{I}$  used, the value of  $\beta$  can be assumed to be a constant. If the value of  $\tilde{I}$  depends on position  $\bar{\mathbf{r}}$  as well, then we can write:

$$\eta(t, \bar{\mathbf{r}}) = \sin^2 \left( \frac{\pi}{2} Q \left[ 1 - \exp(-\beta \tilde{I}(\bar{\mathbf{r}}) t) \right] \right) \quad (2.13)$$

As a specific example, let us consider a situation when two equal intensity, coherent Gaussian beams write a grating in the holographic medium. The intensity distribution will be:

$$I(\bar{\mathbf{r}}) = 2I_0 \exp\left(-\frac{2r^2}{\omega_0^2}\right) \left[ 1 + \text{Cos}(\bar{\mathbf{K}}_G \cdot \bar{\mathbf{r}}) \right]; \quad \bar{\mathbf{K}}_G = \bar{\mathbf{K}}_1 - \bar{\mathbf{K}}_2 \quad (2.14)$$

where  $\bar{\mathbf{K}}_1$  and  $\bar{\mathbf{K}}_2$  are the propagation wave vectors,  $I_0$  is the intensity at the center of each beam, and  $\omega_0$  is the Gaussian beam radius of each writing beam. Comparing equation (2.14) with equation (2.12), we find:  $\tilde{I} = 2I_0 \exp\left(-\frac{2r^2}{\omega_0^2}\right)$ . When this expression is used in equation (2.13)

, the resulting diffraction efficiency is given by:

$$\eta(t, \bar{\mathbf{r}}) = \sin^2 \left( \frac{\pi}{2} Q \left[ 1 - \exp\left(-f(r) \frac{t}{\tau}\right) \right] \right); \quad 0 \leq f(r) \leq 1 \quad (2.15)$$

where  $f(r) = \exp\left(-\frac{2r^2}{\omega_0^2}\right)$ , and  $\tau = \frac{1}{2\beta I_0}$ . Across the spatial profile of the writing beams, the value of  $f(r)$  varies from 1 in the center for  $r = 0$  to a value of 0 for  $r \gg \omega_0$ .

Now, if  $\frac{t}{\tau} \approx 5$ , for example, then at  $r=0$ ,  $\exp\left(-f(r) \frac{t}{\tau}\right)$  approaches zero. However, for  $r \gg \omega_0$ ,  $f(r) \ll 1/5$ , and  $1 - \exp\left(-f(r) \frac{t}{\tau}\right)$  approaches unity. This argument holds for larger value

of  $t/\tau$  as well. Thus for  $t/\tau \geq 5$ , the quantity  $1 - \exp(-f(r) t/\tau)$  varies *monotonically* from one to zero. Therefore, the total number of circular fringes is on the order of  $Q/2$  for  $t/\tau \geq 5$ . Accordingly, we note that for the proper exposure time one can be sure to observe the full number of fringes. To be more precise, let us express  $Q$  as follows:

$$Q = 2m + n + \alpha; \quad \alpha < 1, \quad n = 0, \text{ or } 1 \quad (2.16)$$

In this notation,  $\alpha$  is the fractional part of  $Q$ , while  $n$  determines if  $Q$  is odd or even. Consider first the case where  $n=0$ , and  $\alpha=0$ . In this case, for  $t/\tau \geq 5$ , the number of full circular fringes equals  $m$  with a null at the center. Consider next the situation where  $n=1$ , and  $\alpha=0$ . In this case, the number of full circular fringes will still be  $m$ , but there will be a peak at the center. Finally, for  $\alpha \neq 0$ , the efficiency at the center will have a dip if  $n=1$ , and a peak if  $n=0$ . The actual value of the efficiency at the center reveals the value of  $\alpha$ .

We studied the phenomenon using simulations. Figure 2-13 shows the result for exposure time dependence of the diffraction efficiency for an even  $Q$  value material with a plane wave read-out. This result shows the expected dark center for an even  $Q$  material.

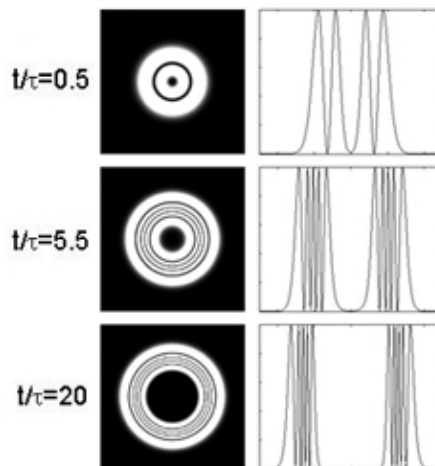


**Figure 2-13: Simulation result showing the evolution of diffracted pattern as a function of holographic exposure for an even Q ( $m=5$ ,  $n=0$ ,  $\alpha=0$  in equation (2.16) value material with a plane wave read-out beam. Normalized diffraction efficiency is plotted versus radial distance.**

Figure 2-14 shows the simulation result for diffraction for a material with an odd Q value plus a fractional part. As expected there is an intensity peak at the center of the diffraction pattern and a dip due to the fractional part. The value at the center yields the value of the fractional  $\alpha$  as 0.2, resulting in a Q value of 11.2 which corresponds to an  $M_{\#}$  value of 17.584.

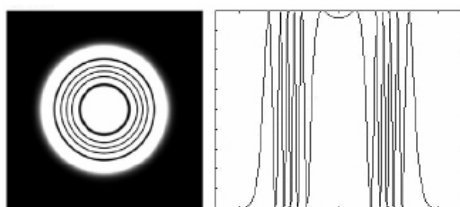


**Figure 2-14: Simulation result for the diffraction pattern for fractional Q with a plane wave read-out beam ( $m=5$ ,  $n=0$ ,  $\alpha=0.2$  in equation 10). Normalized diffraction efficiency is plotted versus radial distance.**

To show the principle of operation experimentally, we used a dye-doped polymeric Memplex®<sup>62</sup> material. This material had a Q value of 6 as claimed by the manufacturer. Figure 2-15 shows the combined setup for hologram writing, and readout. Writing was done with a frequency doubled Nd:YAG laser ( $\lambda=532$  nm), and readout was performed with a He-Ne laser operating at 632.8 nm. This material required baking after holographic exposure. During the experiment, the exposure times were gradually increased. After the exposure, the material was baked until the number of observable interference fringes reached the maximum.

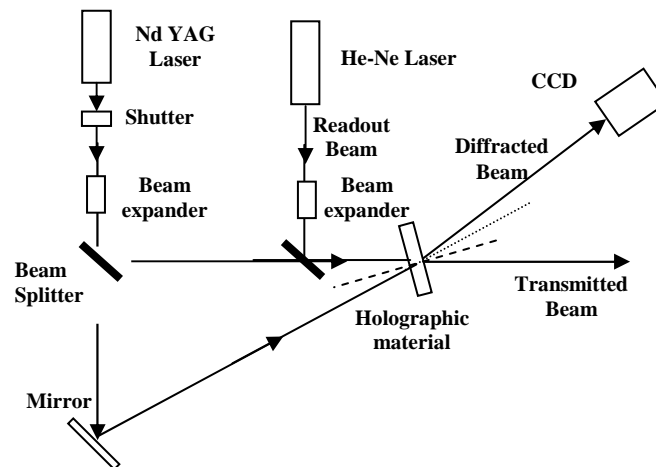
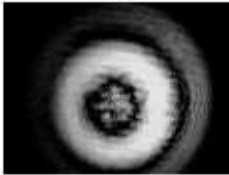
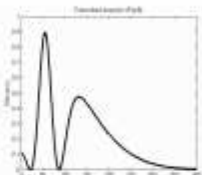
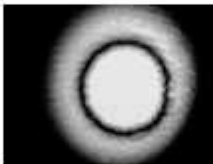
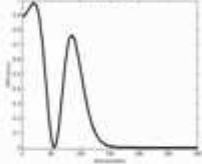
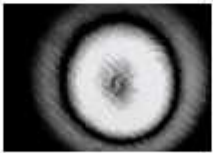


Figure 2-15 :Writing and Read-out Geometry

Table 2-3 shows the results for a series of exposures for the holographic substrate. It shows that as we reach the optimum limit for holographic exposure, the number of interference fringes visible in the diffracted beam reach a maximum (3 in this case). Thus, the  $Q$  for our material is  $\sim 6$ . This value of  $Q$  yields the  $M_{\#}$  of the material as 9.42.

S.N.	Exp. Time (Sec)	Diffracted Images*	Profile of the Diffracted Image
1	26 *Transmitted image		
2	26		
3	52		
4	120		

**Table 2-3: Experimentally observed diffraction pattern for 4 different exposures. As one reaches the optimum limit for holographic exposure, the number of interference fringes visible in the diffracted beam each a maximum.**

To summarize, we have demonstrated a simple approach to determine the  $M_{\#}$  parameter for any holographic recording material. This easy-to-use technique will be very attractive for holographic data storage, where *a-priori* knowledge about the storage material is valuable in determining the storage density and recording schedule for the holograms.

## ***2.8 Conclusion and Next Steps***

The development of holographic materials at Northwestern University has led to processes that can create material for two separate types of applications. Holographic plates for data storage applications have been successfully and repeatedly created, and thick samples for holographic filters have also progressed to the point where application details can be considered. In the future, work will need to be done to find a method of creating samples so that they may be easily removed from their molds as well as to find a way to ensure a higher degree of consistency between samples.

## 3 Holographic Spectral Filters

### 3.1 Introduction

One of the unique properties of a volume (also called a thick or Bragg) grating is that the diffraction efficiency has a spectral and angular bandwidth that is strongly dependent on the effective width of the grating.<sup>6</sup> In other words, the amount of diffracted light drops quickly as the angle or wavelength deviates from the Bragg angle and wavelength. The measured bandwidth at FWHM is approximately proportional to the grating period over the effective width of the grating. In addition to allowing the storage of multiple gratings or holograms in the same location (holographic multiplexing), this angular and spectral selectivity can be used to create novel holographic elements for other purposes, including spectral filters for optical communications.<sup>44, 63-71</sup>

Modern optical communications networks are fiber-based and have replaced copper lines for almost every long-haul and high-bandwidth transport scenario. These systems use wavelength-division multiplexing (WDM) techniques to increase the number of channels that can be used on any given fiber link. These WDM techniques can be classified as “coarse” or “dense” depending on the channel spacing. Current techniques for DWDM can provide a channel spacing of as little as 25 GHz. Using very narrow holographic spectral filters, one can reduce that channel spacing by five to 5 GHz. The ability to carry five times more channels on a fiber provides an important part of the solution to the so-called “last mile problem”. As the bandwidth needs of individual homes increase with the availability of technologies like voice-over-IP (VoIP), digital video delivery systems, and increasingly data-heavy Internet services (such as YouTube and iTunes), the future need for a high-bandwidth link to individual homes

cannot be underestimated. Although the problem of providing this high-speed link to users (the “last-mile problem”) is a public-policy problem as much as it is a technological problem, the political process will advance much quicker once a viable technology is developed. This type of technology can also be used in a military or scientific setting to provide a high-speed link to multiple sites that may have differing needs and capabilities.<sup>72</sup>

With this in mind, our laboratory has been developing a very narrow holographic spectral filter for optical communications. Here I will first present a physical and theoretical view of the nature of the spectral selectivity in volume holograms, and then present my experimental results.

## **3.2 Theoretical Background**

The spectral and angular selectivity of a volume, or Bragg, hologram can be derived in more than one way.<sup>6, 35, 73</sup> Here, I will first show a simple method for deriving the Bragg selectivity that provides a good physical understanding of the process, and also draws analogies to another type of optical device, the Fabry-Perot cavity. Then I will show the basic results from the coupled-wave theory by Kogelnik and others, focusing on the most useful results.

### **3.2.1 Simple Bragg Method**

We consider here the case where a volume holographic grating is formed by the interference of two plane wave beams inside a light-sensitive medium, creating regions of varying index of refraction. The resulting grating is shown in Figure 3-1.

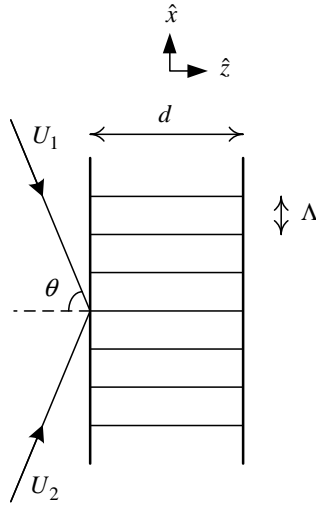


**Figure 3-1: Volume Holographic Grating**

For this case, an unslanted grating, created by beams with symmetric writing angles, is used. The grating period is  $\Lambda$  and the angle of the writing beams is  $\theta$ . The complex amplitudes of the electric field of the two plane waves that created the grating can be written as:

$$\begin{aligned} U_1 &= e^{j(\vec{k}_1 \cdot \vec{r})} \\ U_2 &= e^{j(\vec{k}_2 \cdot \vec{r})} \end{aligned} \quad (3.1)$$

where  $\vec{k}_1 = -\hat{x} \sin \theta + \hat{z} \cos \theta$  and  $\vec{k}_2 = \hat{x} \sin \theta + \hat{z} \cos \theta$ . When the two waves interfere inside the medium, the material response is proportional to the intensity of the interference pattern:

$$|U_1 + U_2|^2 = |U_1|^2 + |U_2|^2 + U_1 U_2^* + U_1^* U_2 \quad (3.2)$$

The first two terms in equation (3.2) are non-varying DC terms, while the last two terms are the so-called interference terms, and can be written as a cosine with spacing  $\Lambda$ , where  $\Lambda = \lambda_B / 2 \sin \theta_B$ . Here, we notate the Bragg wavelength and Bragg angle as  $\lambda_B$  and  $\theta_B$ .

For a physical understanding of the diffraction from a volume grating, it is useful to visualize the process as shown in Figure 3-2. Here we continue to consider the symmetric

grating case. The grating is conceptualized as infinitely thin slices of a different index of refraction, spaced  $\Lambda$  apart.

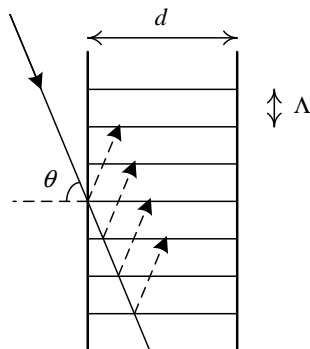


**Figure 3-2: Multiple Reflections from a Bragg grating**

An incoming beam partially reflects from each of the grating planes it encounters as it traverses the medium. For the case where the incoming beam is at the same angle as the writing beams, all of the reflections add up in phase to produce a diffracted beam at a specific angle. This is called Bragg-matched diffraction, and is shown in Figure 3-3a. Each reflection is assumed to have the same magnitude  $r$  and an integer multiple of  $2\pi$  phase difference. The summation of all the reflection leads to the full diffracted beam, shown by the long arrow. This is analogous to a Fabry-Perot resonator. In the Fabry-Perot case, a single beam also generates multiple reflections that can interfere constructively or de-constructively, depending on the path length difference (phase difference).

When the incoming beam is no longer Bragg-matched to the grating (Figure 3-3b.), the phase difference  $\Delta\phi$  is no longer a multiple of  $2\pi$ . When all the reflections are summed, the resultant vector is now shorter than it would be for the Bragg-matched case. In other words, the phase-mismatch has led to lower diffraction efficiency. Bragg mismatch can occur when the angle and the wavelength (either separately or simultaneously) deviate from the angle and

wavelength at which the grating was written. This is analogous to changing the spacing between the mirrors of the Fabry-Perot resonator.

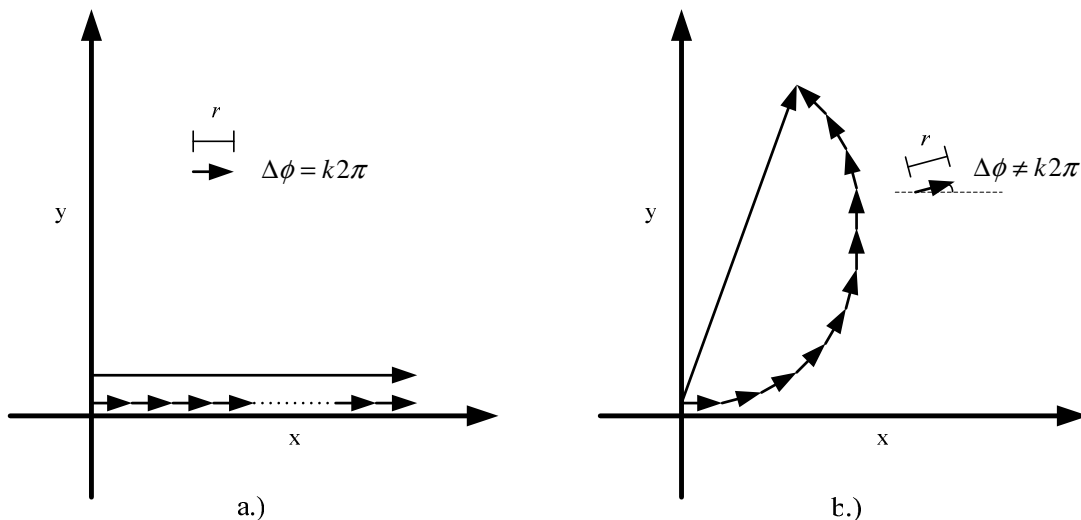


**Figure 3-3: a) Bragg-matched and b) Bragg-mismatched vector summations**

It is important to note that it is possible for the wavelength and angle phase deviations to offset each other, so that for a certain non-Bragg angle, there may be a non-Bragg wavelength that allows the diffracting beam to be Bragg-matched, and vice-versa.

Using the idea of multiple reflections, we can also predict the appearance of sidebands that will diminish in amplitude as the Bragg mismatch increases. Consider the cases shown in Figure 3-4. For the purposes of this figure, only eight reflections are used, although for a typical volume grating the number of reflections would be much higher.

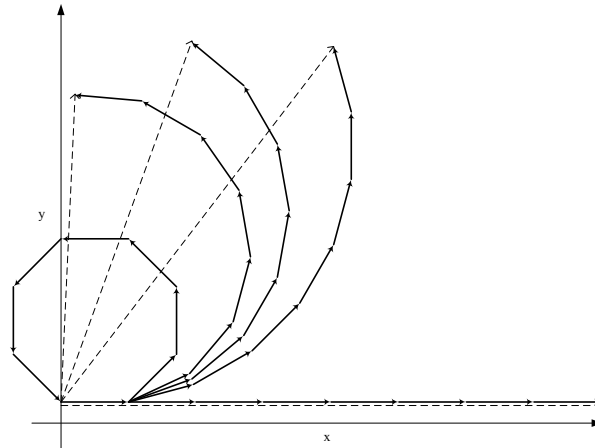


**Figure 3-4: Summation showing first null**

Figure 3-4 shows the resultant diffracted vector for increasing phase-mismatch. As the figure shows, increasing the phase-mismatch will reduce the diffraction efficiency until we reach a point where the resultant vector is null, corresponding to zero diffraction efficiency. For the example shown in Figure 3-4, this happens for a phase mismatch of 45 degrees. In general, there is always an amount of phase mismatch that will result in a null in the diffraction efficiency. For a phase-mismatch larger than this value, there will again be a diffracted vector, thus creating the first sideband, although it will be smaller than the previous maximum. This is shown in Figure 3-5.

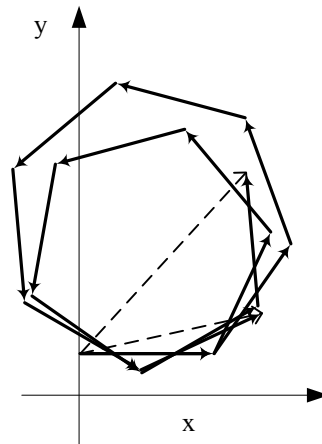


**Figure 3-5: Summation showing first sideband**

Eventually the phase mismatch will again reach a value that will lead the vectors to form a closed loop, creating another null. Thus, this qualitative way of examining the multiple reflections leads us to understand how phase mismatching in Bragg gratings leads to lowered diffraction efficiency and sidebands in the angular or spectral selectivity.

To determine the effects of a phase-mismatch (the spectral and angular selectivity), we first derive the path-length difference using Figure 3-6.

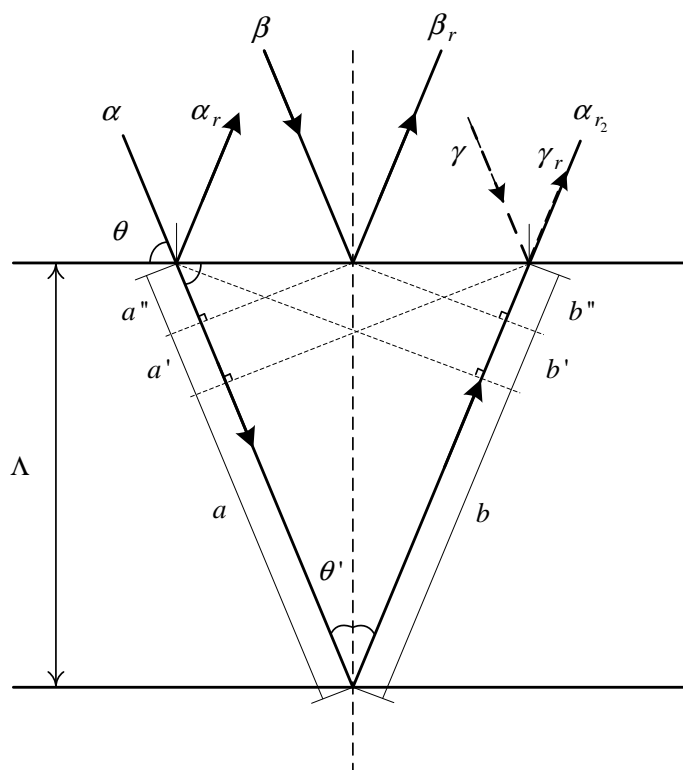


**Figure 3-6: Key reflections from the grating planes**

In this figure, two grating planes are shown along with several rays ( $\alpha, \beta, \gamma$ ) along a plane wave front. Their respective reflections are ( $\alpha_r, \beta_r, \gamma_r, \alpha_{r_2}$ ). In this diagram, the angle of incidence is denoted  $\theta$ , and the wavelength of the incident beam is  $\lambda$ . First, we measure the

path difference between the reflection  $\alpha_r$  and  $\alpha_{r_2}$ . The difference is  $(a+a'+a'')+b$ . Using the geometry of Figure 3-3, we see that:

$$\begin{aligned} (a+a'+a'') &= \frac{\Lambda}{\sin \theta}, \quad b = (a+a'+a'') \cos(2\theta') = \frac{\Lambda}{\sin \theta} \cos(2(90-\theta)) \\ \Delta L &= \frac{\Lambda}{\sin \theta} (1 - \cos(2\theta)) = \frac{\Lambda}{\sin \theta} (1 - (1 - 2\sin^2 \theta)) \\ \Delta L &= 2\Lambda \sin \theta \end{aligned} \quad (3.3)$$

Next we measure the path difference between  $\beta_r$  and  $\alpha_{r_2}$ . Using Figure 3-3 along with the results from equation (3.3):

$$\begin{aligned} \Delta L &= a + a' + b + b' \\ a + a' &= \Lambda \cos \theta' = \Lambda \sin \theta = b + b' \\ \Delta L &= 2\Lambda \sin \theta \end{aligned} \quad (3.4)$$

Finally, in the same manner as above, we see that the path difference between  $\alpha$  and  $\gamma_r$  is  $(b+b'+b'')+a$ , and that this is again equal to  $2\Lambda \sin \theta$ .

The phase difference between each layer is then (where  $k$  is the wave number of the incident beam):

$$\begin{aligned} \Delta \phi &= k \Delta L \\ \Delta \phi &= \frac{2\pi}{\lambda} 2\Lambda \sin \theta \\ \Delta \phi &= \frac{2 \sin \theta}{\lambda} \cdot \Lambda \cdot 2\pi \end{aligned} \quad (3.5)$$

From the result of equation (3.5), it is obvious that when  $\theta$  and  $\lambda$  are equal to  $\lambda_B$  and  $\theta_B$ ,  $2 \sin \theta / \lambda$  will equal  $\Lambda$ , and the phase difference is simply  $2\pi$  (or an integer multiple thereof). This is the Bragg-matched case. The quantities  $\lambda$  and  $\theta$  are now allowed to differ from the angle and wavelength used to create the grating. Any deviation from the Bragg angle or Bragg wavelength will result in a path-length difference between the multiple reflections. This in turn

leads to smaller amplitude of the diffracted beam, since there is some destructive interference.

For the case where there is a deviation in either the read wavelength or read angle or both, the phase difference may no longer be an exact multiple of  $2\pi$ . We can sum all the reflections taking care to include the phase difference to determine an expression that will include the effects of de-phasing:

$$U_{\text{diffracted}} = r_0 + r_0(1-r_0)e^{i\Delta\phi} + r_0(1-r_0)^2 e^{i2\Delta\phi} + \dots + r_0(1-r_0)^{n-1} e^{i(n-1)\Delta\phi}$$

$$U_{\text{diffracted}} = \sum_{n=1}^N r_0(1-r_0)^{n-1} e^{i(n-1)\Delta\phi} \quad (3.6)$$

In equation (3.6),  $N$  is the total number of reflections, which is simply  $\lfloor d \tan \theta / \Lambda \rfloor$ . Evaluating the sum in equation (3.6), we find:

$$U_{\text{diffracted}} = \frac{r_0 \left( 1 - (1-r_0)^N e^{iN\Delta\phi} \right)}{1 - (1-r_0) e^{i\Delta\phi}}$$

$$I_{\text{diffracted}} = \frac{r_0^2 \left[ 1 + (1-r_0)^{2N} - 2(1-r_0)^N \cos(N\Delta\phi) \right]}{1 + (1-r_0)^2 - 2(1-r_0) \cos(\Delta\phi)} \quad (3.7)$$

The final expression for the intensity of the diffracted beam versus  $\Delta\phi$  can now be plotted and compared with the results from theory.

The result of equation (3.7) was calculated from the comparable equation from coupled-wave theory for non-absorbing transmission gratings:<sup>6</sup>

$$\eta_{\text{diffracted}} = \frac{\sin^2 \left( \sqrt{\nu^2 + \xi^2} \right)}{1 + \xi^2 / \nu^2} \quad (3.8)$$

The variables  $\nu$  and  $\xi$  are as defined in reference 6, where  $\nu$  is proportional to the grating strength and  $\xi$  is proportional to the de-phasing. Both equations were used to plot normalized

diffracted intensity versus  $\Delta\phi = \Delta\theta$  using the same parameters: an incident angle of 30 degrees, an index modulation of  $1 \times 10^{-4}$ , and an index of refraction of 1.5. The coupled-wave theory result (CWT) and the simple Bragg theory (SBT) are plotted in Figure 3-7.

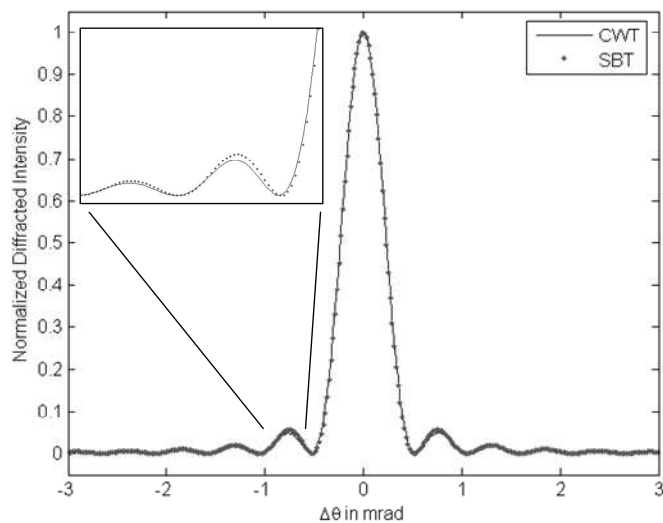


**Figure 3-7: Comparison between the CWT and SBT for an index of modulation of  $1e-4$**

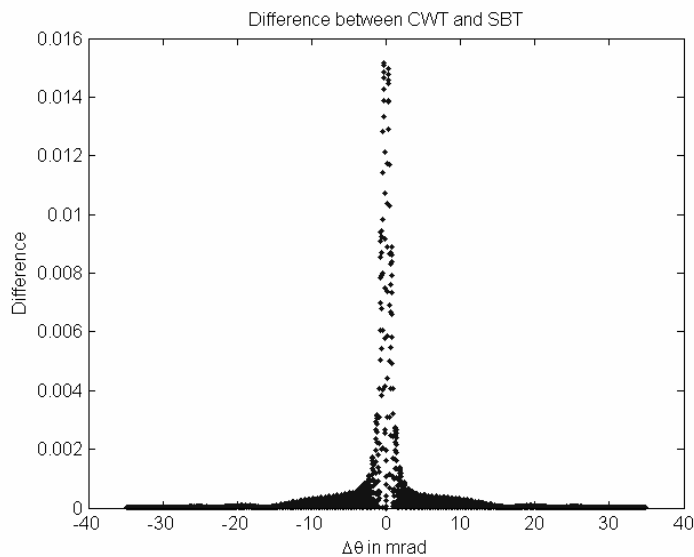


**Figure 3-8: Difference between the CWT and SBT in Figure 3-7**

For this index modulation, the agreement between the two theories is very good, with a maximum error of about 1.5%. The absolute value of the difference between the two is shown in Figure 3-8. Figure 3-9 shows the result using a smaller index modulation of  $1 \times 10^{-5}$ . Figure 3-10 indicates that for smaller values of the index modulation, the agreement is even better. The same results were obtained for the two theories using  $\Delta\phi = \Delta\lambda$ , as one would expect since equation (3.7) or equation (3.8) depend on the phase difference ( $\Delta\phi$  and  $\xi$ , respectively), which can be caused by a change in angle or wavelength independently.

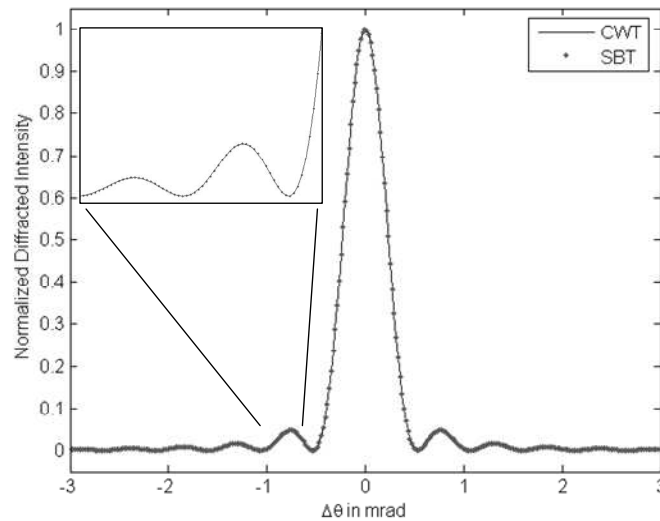


**Figure 3-9: Comparison between the CWT and SBT for an index of modulation of  $1e-5$**

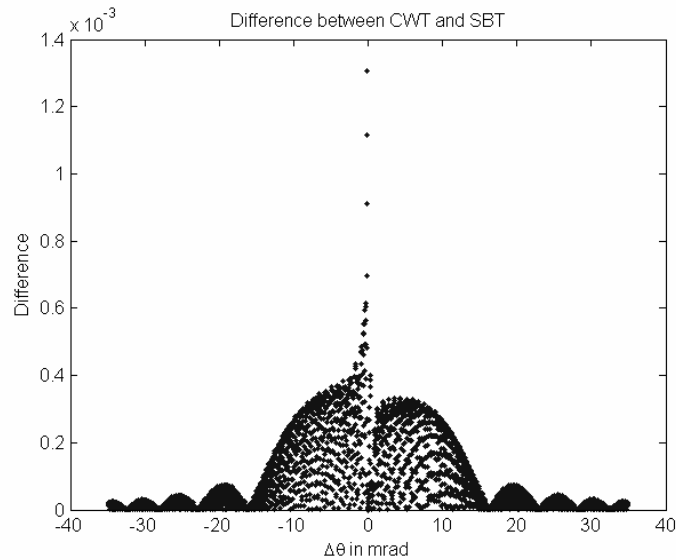


**Figure 3-10: Difference between the CWT and SBT in Figure 3-9**

This simple method for Bragg diffraction thus provides a good physical insight into the Bragg diffraction process, and compares well with the more rigorous CWT as well. For our calculations, we will use the coupled-wave theory in order to ensure a more complete match, as well as to provide a theoretical match for certain cases such as reflection and slanted gratings that are not covered by the simple Bragg method.

### 3.2.2 Coupled-Wave Theory Results

The SBT shown previously provides a good physical picture of the nature of the Bragg selectivity. In this section, I summarize the results that are obtained by using the more rigorous approach of the coupled-wave theory. For a full treatment, see references<sup>6, 74</sup> or Appendix 10.1.

The coupled-wave equations are found by assuming the interaction of two waves inside the medium—the incoming wave  $R$  and the diffracted wave  $S$ . All other orders are assumed to violate the Bragg condition strongly and are ignored. The slowly-varying envelope approximation is also made, and the resulting equations can be solved for the cases of

transmission and reflection gratings, slanted or unslanted, and with or without loss. Our experiments use lossless gratings so I will focus on that case here. The geometry in Figure 3-11 shows the notation used in the coupled-wave results. By performing the same analysis as found in Section 3.2.1, we find that the grating spacing  $\Lambda$  is equal to  $\lambda/2\sin\theta$ , where  $\theta$  is the writing angle for symmetric writing beams.

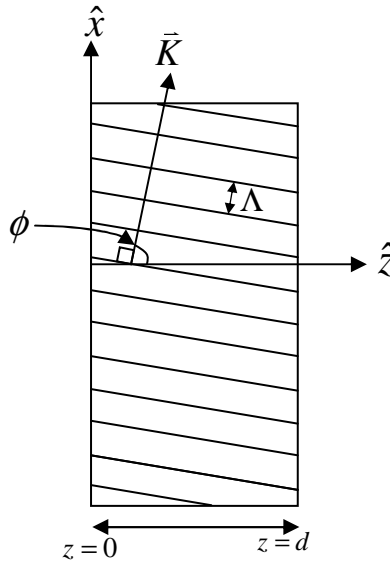


**Figure 3-11: Geometry for Coupled-Wave results**

For a lossless transmission grating, these equations lead to the following expression for the diffraction efficiency:

$$\eta = \frac{\sin^2(v^2 + \xi^2)^{\frac{1}{2}}}{\left(1 + \xi^2/v^2\right)} \quad (3.9)$$

In equation (3.9),  $v$  is related to the strength of the grating compared to the geometry of the grating, while the parameter  $\xi$  is proportional to the dephasing:

$$\begin{aligned}
\nu &= \pi n' d / \lambda (c_R c_S)^{\frac{1}{2}} \\
\xi &= \vartheta d / 2c_S \\
\vartheta &= \Delta\theta K \sin(\phi - \theta) - \Delta\lambda K^2 / 4\pi n
\end{aligned} \tag{3.10}$$

In equation (3.10),  $n'$  is the index modulation (grating strength),  $d$  is the grating thickness, and  $c_R$  and  $c_S$  are the obliquity factors that take into account the angle of the input beam and the slant of the grating. The dephasing parameter  $\xi$  can be related to the change in angle or wavelength through the parameter  $\vartheta$ .

For an unslanted, lossless transmission grating, the results of equation (3.9) can be simplified to the following rules of thumb:

$$\begin{aligned}
2\Delta\theta_{\frac{1}{2}} &\approx \frac{\Lambda}{d} \\
\frac{2\Delta\lambda_{\frac{1}{2}}}{\lambda} &\approx \cot\theta \frac{\Lambda}{d}
\end{aligned} \tag{3.11}$$

For a lossless reflection grating, the equations are similar:

$$\eta = \frac{1}{\left\{ 1 + \frac{\left( 1 - \frac{\xi^2}{\nu^2} \right)}{\sinh^2 \left( \nu^2 - \xi^2 \right)^{\frac{1}{2}}} \right\}} \tag{3.12}$$

where  $\nu$  has been slightly modified:

$$\nu = j\pi n' d / \lambda (c_R c_S)^{\frac{1}{2}} \tag{3.13}$$

For the transmission case it is important to re-derive the grating spacing  $\Lambda$  and note that the angle of the grating,  $\phi$ , is 0 for the symmetric case. This leads to a negative value for the  $c_S$  parameter and the relationship for  $\Lambda$  is now:

$$\Lambda = \frac{\lambda}{2 \cos \theta} \quad (3.14)$$

Equation (3.14) is very similar to the grating spacing for a transmission grating in equation (3.3) except that it is the cosine of the angle that is taken. The difference in grating spacing leads to a key difference in the angular and spectral bandwidths of these two types of gratings.

Using these results for the spectral bandwidth of transmission and reflection gratings, one can predict the expected performance of volume holographic grating filters. From the rules of thumb in equation (3.11), we see that one way to create a more selective filter is to increase the thickness  $d$  of the grating. Reducing the grating spacing  $\Lambda$  also helps to reduce the bandwidth. For a fixed reading wavelength, this is equivalent to changing the angle to decrease the grating spacing. These rules hold for reflection gratings as well, and by plotting equation (3.9) and equation (3.12) for various parameters, we can determine several important characteristics. In Figure 3-12, the two equations are plotted for equal parameters. The writing and reading wavelength is 532 nm, inside a material with an index of 1.52 and thickness of 500 microns, at symmetric writing angles of  $30^\circ$  with an index modulation of  $1 \times 10^{-4}$ .

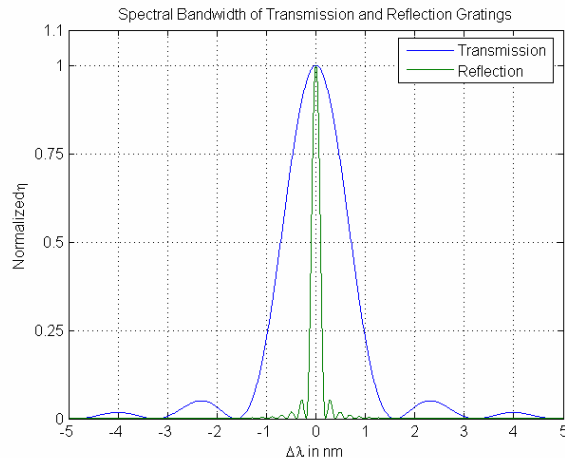


**Figure 3-12: Plot comparing the spectral bandwidth of transmission and reflection gratings**

From the plot it is visibly evident that the bandwidth of the reflection grating is much smaller than that of the transmission grating. The reason for this can be seen by comparing the grating spacing to grating thickness ratio in both cases. For the transmission case, the ratio  $\Lambda/d$  is approximately 0.001, while for the reflection case, the ratio is 0.00037, almost three times smaller. In other words, by using a writing geometry that tends to align the grating planes parallel to the writing surfaces of the medium, a larger effective thickness is obtained. That is to say, in the reflection geometry, an incident beam crosses more grating planes than in the equivalent transmission geometry. As we showed in Section 3.2.1, the spectral (and angular) bandwidth is dependent on the total phase difference accumulated over each reflection, and thus a larger number of reflections means a smaller deviation leads to the same phase difference.

For the same reflection grating used in Figure 3-12, a comparison between differing thicknesses shows the expected trend. An increase in grating thickness is accompanied by a corresponding decrease in bandwidth. This is illustrated in Figure 3-13.

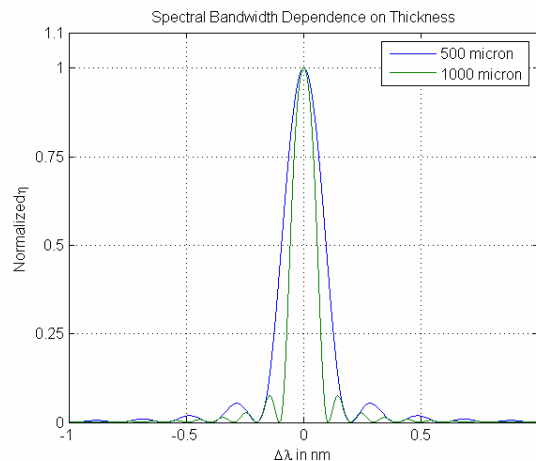


**Figure 3-13: Plot comparing the spectral bandwidth for differing grating thicknesses**

The equations shown here and the rules derived from them are useful guidelines in the construction of holographic spectral filters, and can be compared to experimental data as well.

### **3.3 Experimental Results**

There are many challenges in making an ultra-narrow holographic spectral filter. As I showed in Section 3.2, the spectral bandwidth is related to the effective thickness of the grating. More specifically, it is related to the grating period divided by the material thickness taking into account the angle at which the read beam is traversing the medium:

$$\frac{\Delta\lambda}{\lambda} \approx \cot \theta \frac{\Lambda}{d} \quad (3.15)$$

In other words, the selectivity increases for a smaller grating period ( $\Lambda$ ) as well as for a greater number of total grating periods, as seen by the read beam ( $\cot \theta/d$ ). Thus, increasing the usable thickness of the material can greatly enhance the selectivity. However, a greater thickness leads to increased absorption and an uneven grating profile due to the absorption of the writing beams as they traverse the medium. This can be countered by lowered the photosensitivity of the material, at the expense of overall sensitivity, which in turn leads to long write times or high powers during writing. Issues relating directly to the materials are discussed in Chapter 2.

In addition to the process of creating a thick material, there are additional material-imposed restrictions. The wavelength sensitivity of most holographic materials (the wavelength at which they must be written) is almost always in the visual range because most research into light-sensitive dyes has been done in the visible range. This is partly due to the fact that most commercial applications for dyes are aimed at the human visual system, and also partly due to the fact that lasers are available in mostly visible wavelengths. Fiber optic communications is carried out at 1550 nm, and although there are laser sources and amplifiers for this wavelength

range, there are no photosensitive materials available yet. This means that the holographic gratings for these devices will be operated at a different wavelength than the one at which they will be written.

In the following sections, I will describe the experiments I have carried out to date along with the challenges that have I have encountered.

### 3.3.1 First Test: Dye Laser

Because of its inherently higher spectral selectivity, reflection holograms are desired for spectral filtering. For the first test of the Laboratory for Atomic and Photonic Technologies (LAPT) thick material, a single reflection grating was written. In order to test its spectral selectivity, a scanning laser source was needed. For this test, a Coherent 800 series dye laser was used at a center wavelength of 590 nm, which was different from the writing wavelength of 532 nm. This experiment tested the optical quality of the first thick material sample, the reflection holographic filter geometry, and the ability to write gratings at one wavelength and read them at another.

The writing geometry is shown in Figure 3-14. A beam from a 5.5W Coherent Verdi Nd:YAG laser at 532 nm is sent through a spatial filter to create a more uniform beam profile and expand the size of the beam. A collimating lens captures the expanded beam, and a beamsplitter is used to create the recording arms. Mirrors are used to direct the writing beams to the holographic material at an external angle of incidence of  $\theta_{W_{ext}} = 45^\circ$ . The index of refraction of the material has been measured at 1.482, and so the angle inside the medium from Snell's law is  $\theta_{W_{in}} = 28.54^\circ$ . The holographic substrate is mounted on a stable platform that can be rotated about the z-axis. This is done so that a small angle of rotation may be introduced to create a

slanted grating. The reason for using this slight deviation from the symmetric case is that for a symmetric (unslanted) reflection hologram, the diffracted beam will be overlapped with the reflected beam. By introducing a small slant angle, the diffracted beam may be separated from the reflected beam, so that a direct measurement of the diffracted beam is possible.

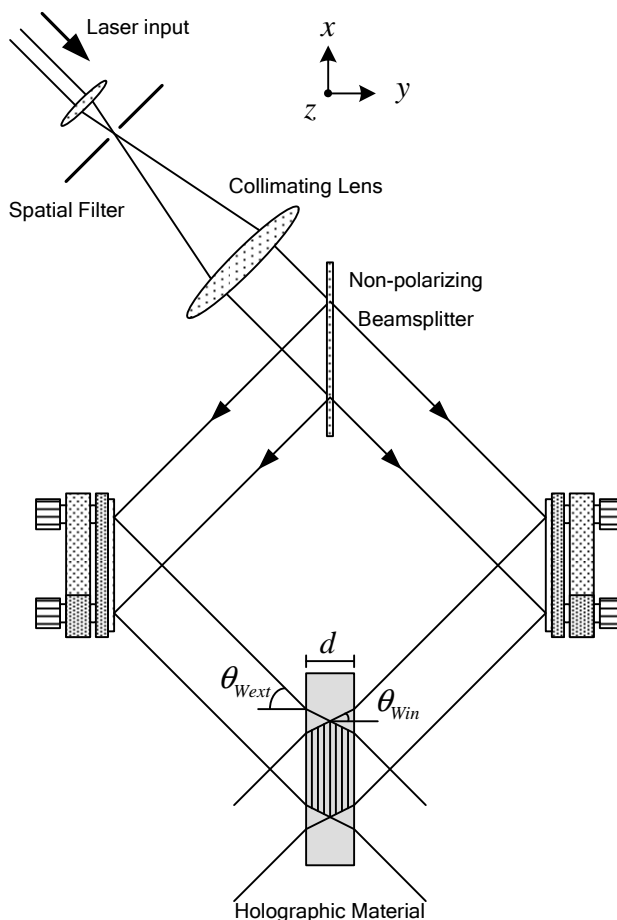


**Figure 3-14: Writing setup for holographic filter**

The holographic material that was used was made with a low amount of photosensitive dye to limit absorption effects. This made the material fairly insensitive, so a 20 second exposure was necessary. After recording, a peak diffraction efficiency of 27% was measured. The material was then tested for spectral selectivity using the dye laser. The maximum available sweep was 29.999 GHz total. A photodiode was used to measure the diffracted power. The trace from the

oscilloscope is shown in Figure 3-15. The red plot is the frequency scan (29.999 GHz at 590 nm center), and the blue plot is the photodiode signal. From the figure, one can see that the full bandwidth of the diffraction efficiency is larger than the scan width, and that the diffracted beam was not properly centered. However, there is enough information to extrapolate the full-width half-maximum of the spectral bandwidth.

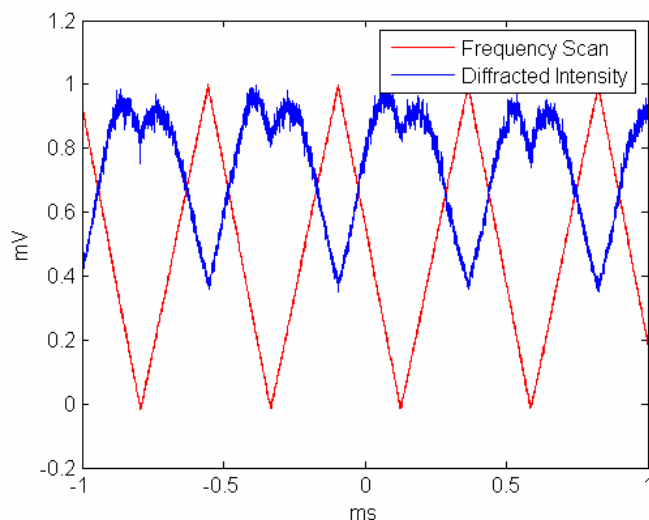


**Figure 3-15: Oscilloscope trace showing frequency scan and diffracted power**

Given that one full sweep is about 30 GHz, we estimate the FWHM bandwidth of this grating to be between 40 and 45 GHz. The coupled-wave theory result for a sample of the thickness used here indicates that a bandwidth of approximately 25 GHz should be expected. The difference is most likely caused by the actual grating interaction length being shorter than anticipated due to the Gaussian nature of the writing beams and the material absorption.

### 3.3.2 Six Holographic Spectral Filters for 1550 nm

In order to test the ability to create gratings that could actually be used in a fiber optic network, the next experimental step was to create reflection gratings for the 1550 nm wavelength

band. Unlike the previous experiment, where the wavelength difference between writing and reading was small (532 nm to 590 nm), writing gratings with a 532 nm source for use at 1550 nm required a modified approach.

Because of the large difference in wavelength, these gratings must be written at 532 nm in transmission geometry, and read at 1550 nm in reflection geometry. The grating spacing  $\Lambda$  for transmission geometry is:

$$\Lambda = \frac{\lambda_w}{2 \sin \theta_w} \quad (3.16)$$

In equation (3.16),  $\lambda_w$  is the writing wavelength, and  $\theta_w$  is the half-angle between the two writing beams, measured from the normal to the surface of the medium. If the grating is being written with non-symmetric angles, this must be taken into account as in Appendix 10.4. The corresponding expression for reflection geometry is:

$$\Lambda = \frac{\lambda_r}{2 \cos \theta_r} \quad (3.17)$$

where the reading wavelength and angle are now denoted with a subscript  $r$ . Equating equations (3.16) and (3.17) allows one to solve for the writing angle necessary to create a reflection grating at the read wavelength, using the write wavelength in transmission geometry.

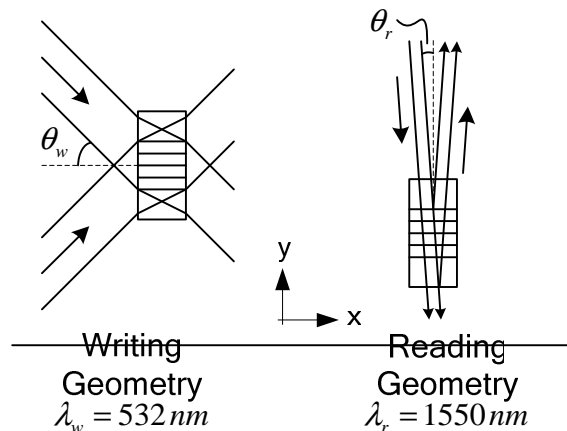


**Figure 3-16: Transmission write/Reflection read geometry**

This geometry is shown in Figure 3-16. Writing is done in transmission, and reading is done in reflection mode. In practice, this geometry offers some advantages but also introduces some problems. If beams with sharply-defined edges are used for writing, such as those that are produced when the incoming beam is apertured, the crossing pattern of the beams will produce a grating profile that is undesirable. It will present an un-even front to an incoming beam in reflection mode. This can be mitigated by using apodized beams. Using Gaussian writing beams, for instance, can help reduce this problem by gradually reducing the grating strength at the edges of the grating; however, the effective length of the grating is also reduced. A full treatment of apodization and apodizing methods should be considered necessary for the future development of these filters.

Another problem that was encountered involved the material construction. The samples that were used in these experiments were created at Northwestern University and consisted of a glass cell filled with a polymer material. The glass of the cell and the polymer had different indices of refraction, and both differ from the index of air. The glass cell was not anti-reflection (AR) coated because of the particular process of creating these samples. Because the samples are so much thicker than are normally obtained for this type of material, the procedure for creating them has not yet been perfected. Often times the cell would crack along the edges, leaving the sample usable for our purposes but not reusable. Cells that did not crack could be reused by dissolving the hardened sample using trichloroethylene and cleaning the glass with methanol. AR coatings would be prohibitively expensive for cells that could only be used once, and so it was not pursued.

However, the lack of an AR coating led to multiple reflections that could then interfere amongst themselves and create ghost and noise gratings. These ghost and noise gratings lead to phantom diffraction spots and lower the overall efficiency of the desired grating. In addition, the corners of the cell where the glass sides were fused created scattering surfaces that led to scattered, diffuse light throughout the volume of the sample. In order to reduce this noise without resorting to AR coating each cell, an index-matching solution was pursued. A large glass cell of the same index of refraction as the sample cells was constructed and filled with an index matching fluid. This effectively created a very large glass cell with the material sample inside it. The primary reflection to be eliminated is the large reflection from the glass-air interface on the opposite side of the writing beams. With no AR coatings and no index matching, the large refractive index difference between the glass and air creates a strong reflection back into the holographic material, as shown on the left side of Figure 3-17. Only one of the writing beams is shown in the figure, but the other writing beam will have the same problem. Because of the large coherence length of the source laser, these reflections will be in phase and can interfere to create ghost gratings. In addition, the reflections may reflect from the joints between the sides of the cell, continuing to interfere and create noise gratings as well as use up part of the photosensitive dye in the material.

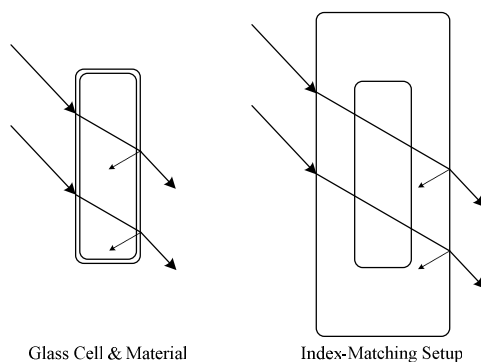


**Figure 3-17: Glass cell and index matching setups with primary reflection**

On the right side of Figure 3-17, the large index-matched cell does not eliminate reflections; however, by spacing out the effective sides of the cell, the reflections do not all reflect back into the material. The effect of the joints is also reduced greatly. The experimental setup is shown in Figure 3-18.

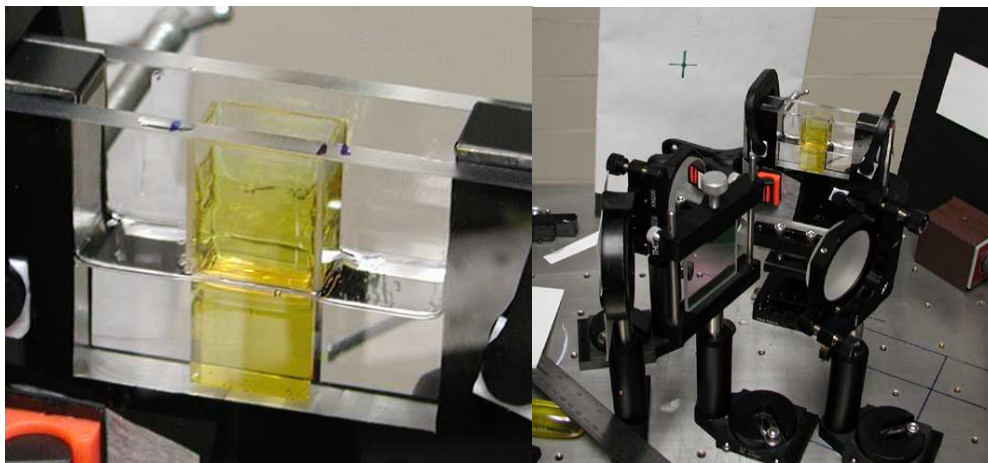


**Figure 3-18: Index Matching Setup**

Overall, the index-matching setup did allow a better quality of grating to be written. However, once the material creation process is perfected, it is more desirable to use AR coatings to reduce the magnitude of the reflections rather than try to contain them. A good AR coating can reduce the reflections to less than 0.1%, a level at which they will not be strong enough to create significant ghost or noise gratings.

Once the writing setup had been tested, we attempted to create a set of holographic filters for use at 1550 nm. For this experiment, six gratings were written in separate substrates. Each substrate was made using the LAPT PMMA material as described in Chapter 2. The material was poured into fluorometer cells and then hardened before use. The cells were of optical quality on all four sides, which is important for using the transmission write/reflection read

geometry as beams must be incident on the material from all sides. The six cells can be seen in Figure 3-19.

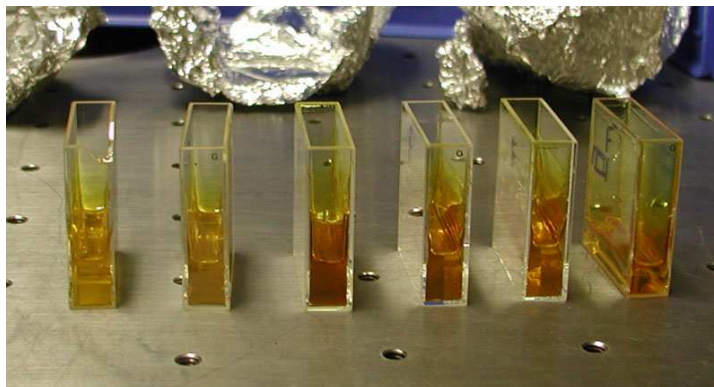


**Figure 3-19: Six holographic spectral filters**

The spectral bandwidth of the six gratings was measured using an Agilent tunable source. The source resolution was 0.01 nm, and the gratings were measured for efficiency and spectral width. The results are shown in Figure 3-20. As the data shows, filters 4 and 5 have a larger bandwidth than 1, 3, and 6, which are all similar, while filter 2 is narrower than the rest. This variation is partly due to the fact that each substrate was different. The differences, especially in dye concentration, led to gratings with a varying efficiency. Figure 3-20 shows the normalized results of the test, but the diffraction efficiency varied from as low as 22% to as high as 71%.

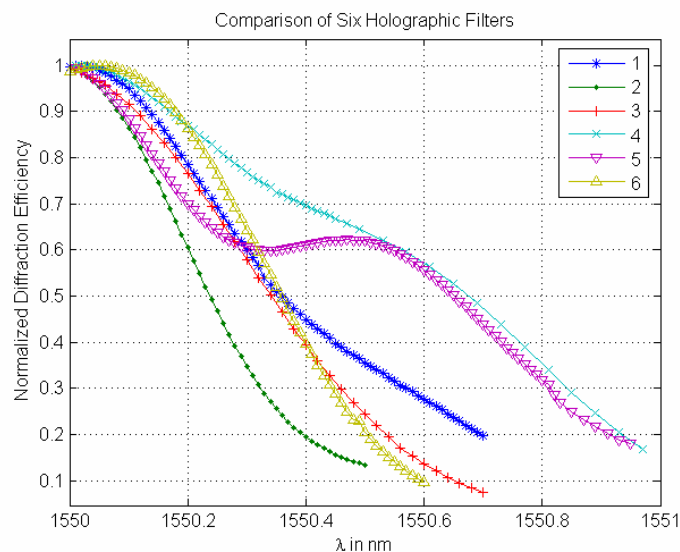


**Figure 3-20: Comparison of six holographic filters**

### **3.4 Conclusion and Next Steps**

These six filters are the first step in realizing ultra-narrow holographic spectral filters for optical communications. The best result obtained was 71% diffraction efficiency and a 0.2 nm spectral bandwidth. These results demonstrate the feasibility of holographic spectral filters using the LAPT material. Gratings in the material have been created at up to 99% diffraction efficiency, which would be a requirement for minimizing insertion loss in optical communications systems. Aside from diffraction efficiency, the bandwidth of the filters must also be reduced. As discussed in this section, the bandwidth is most dependent on the effective interaction length between the read beam and the grating. In order to increase this length, higher quality material samples are required. Once high-quality, AR-coated samples can be created consistently, beam widths can be almost as wide as the length of the sample without fear of reflections causing an unacceptable level of noise. One promising approach to further this goal would be to reduce the horizontal thickness of the samples. Referring to Figure 3-16, in read

mode the small angle means that a wide grating is not necessary; it must simply be long in the y direction. A thinner sample will require less material which will allow easier processing. In addition, less material in the x direction will result in less distortion of the writing beams due to absorption.

In summary, the preliminary work for holographic gratings for optical communications at 1550 nm has been performed. Further development of the holographic material will allow very narrow spectral filters that in turn can be used for super-dense wavelength division multiplexing, a key enabling technology in solving the "last-mile" problem.

## 4 Holographic Stokesmeter

### 4.1 Introduction

Polarimetric imaging<sup>75-77</sup> takes advantage of the fact that a given object emits and scatters light in a unique way, depending on its polarimetric signature. Identifying the polarimetric signature is equivalent to identifying the scattered Stokes vector.<sup>78, 79</sup> An active polarimetric sensor is used in applications such as target recognition, vegetation mapping, pollution monitoring, geological surveys, and medical diagnostics.<sup>80-82</sup>

Current polarization imaging systems include mechanical quarter-wave plate/linear polarizer combinations,<sup>83</sup> photo-detectors with polarization filtering gratings etched onto the pixels, and liquid crystal variable retarders. The speed of the mechanical sensor is limited because each Stokes parameter is determined sequentially and the wave plate/polarizer combination must be re-oriented precisely between parameters. At this time, the etched photo-detector systems cannot resolve the complete Stokes vector at this time. The liquid crystal retardation is very similar to the mechanical sensor but has a liquid crystal display that replaces the wave plates and polarizers. This method is still sequential and is restricted by the time it takes the display to re-orient itself, typically on the order of 100 ms per scan. This limits the throughput to  $\sim 10$  Hz.

To examine the advantages of the proposed architecture and to quantify its speed, we examine each component (see Figure 4-1). A typical thick hologram ( $\sim 1$  mm) has a channel bandwidth on the order of 1 nm (and an angular bandwidth of  $\sim 1$  mrad), corresponding to an optical response time of  $\sim 10$  ps. The signal manipulation can be accomplished with pre-calibrated field-programmable gate arrays (FPGA) or programmable logic arrays (PLA) and does

not require real-time processing. These devices perform at roughly the speed of the logic gates, typically on the order of 1 ns. The detector array response time is determined in part by the desired signal to noise ratio (SNR). The SNR is proportional to  $\sqrt{\eta I \tau}$ , where  $\eta$  is the quantum efficiency,  $I$  is the intensity, and  $\tau$  is the average time. For a typical SNR of 10, the response time is then given by the detector-specific parameters and the amount of light reflected by the target. It should be noted that the constraints imposed by a given SNR and the detector array are common to all of the methods discussed here. The advantage of our design is that it can determine the complete Stokes vector in parallel, so that the detector and not the sensor is the limiting factor in determining the speed of the device.

## **4.2 Basic Architecture**

The architecture is shown in Figure 4-1. The incoming image is split into two copies using a beam splitter. The first beam is diffracted into two beams using two multiplexed holographic gratings. The second beam passes through a quarter-wave plate before diffracting from a similar set of multiplexed holographic gratings. The diffracted beams are projected onto four CCD arrays. Their intensities are summed with pre-determined weights to compute each component of the Stokes vector. These weighting factors are determined by using the parallel and perpendicular polarization components of diffraction to formulate the Mueller matrix that describes the transformation of the initial Stokes parameters by grating diffraction. This design takes advantage of the fact that a hologram is sensitive to the polarization of the incident light, and the weighting factors can be determined analytically by using a Mueller matrix analysis of the architecture.

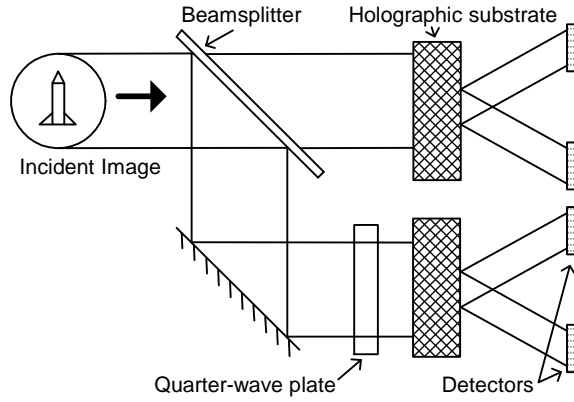


**Figure 4-1: Holographic Stokesmeter Architecture**

For an arbitrary image pattern, the diffraction efficiencies depend also on the range of spatial frequencies. Here, we restrict our analysis to the simple case of a plane wave incidence, which can be extended easily to analyze the general case. Figure 4-2 illustrates the progression of the light through a thick hologram.

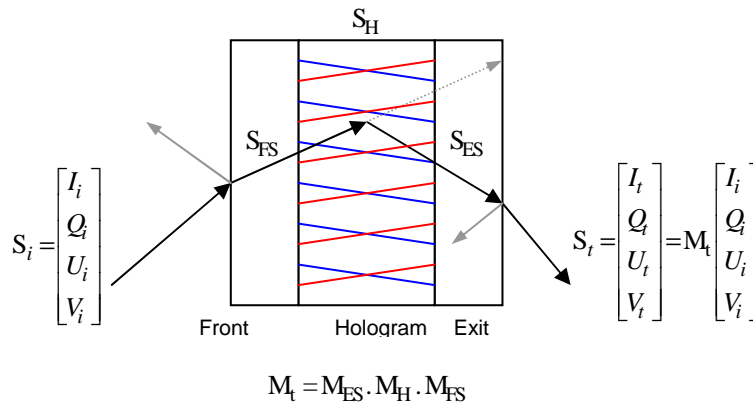


**Figure 4-2: Mueller matrix representation of holographic diffraction**

This process is represented mathematically by a series of Mueller matrices<sup>84, 85</sup> that describe the transformation of the input Stokes vector  $S_i$ . The Stokes vector  $S_{FS}$  of the transmitted beam through the front surface of the hologram is:

$$\mathbf{S}_{\text{FS}} = \mathbf{M}_{\text{FS}} \mathbf{S}_i = \frac{1}{2} \begin{bmatrix} t_{\parallel}^2 + t_{\perp}^2 & t_{\perp}^2 - t_{\parallel}^2 & 0 & 0 \\ t_{\perp}^2 - t_{\parallel}^2 & t_{\parallel}^2 + t_{\perp}^2 & 0 & 0 \\ 0 & 0 & 2t_{\parallel}t_{\perp} & 0 \\ 0 & 0 & 0 & 2t_{\parallel}t_{\perp} \end{bmatrix} \begin{bmatrix} I_i \\ Q_i \\ U_i \\ V_i \end{bmatrix} = \begin{bmatrix} I_{\text{FS}} \\ Q_{\text{FS}} \\ U_{\text{FS}} \\ V_{\text{FS}} \end{bmatrix} \quad (4.1)$$

where  $\mathbf{M}_{\text{FS}}$  is the Mueller matrix for the transmission from the front surface, and  $t_{\parallel}$  and  $t_{\perp}$  are the Fresnel transmission coefficients corresponding to the components of linearly polarized light parallel and perpendicular to the plane of incidence. One can describe the Mueller matrix for the exit surface of the hologram in the same manner.

In order to construct the Mueller matrix for the grating itself,  $\mathbf{M}_{\text{H}}$  in Figure 4-2, we describe the amplitude of the diffracted beam for parallel and perpendicular incidence in a manner analogous to the Fresnel reflection/transmission case. For our purposes here, we need to describe only the diffracted beam and not the transmitted component. The relevant parameters are illustrated in Figure 4-3.

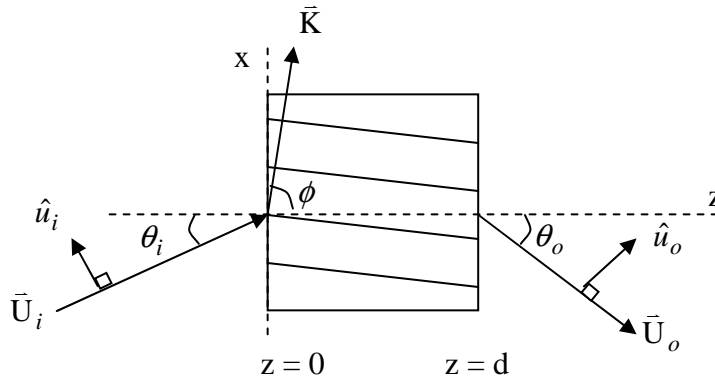


**Figure 4-3: Volume grating diffraction**

$\bar{U}_i$  is the input beam, and  $\bar{U}_o$  is the output beam, where  $\hat{u}_i$  and  $\hat{u}_o$  are the respective polarization vectors normal to the direction of propagation.  $\bar{K}$  is the grating vector, which makes an angle  $\phi$  with the  $z$  axis. We recall that the amplitude of the diffracted beam is given by:<sup>86</sup>

$$\frac{U_o}{U_i} = -i\alpha \sin \left( \sqrt{\frac{(\kappa(\hat{\mathbf{u}}_i \cdot \hat{\mathbf{u}}_o)d)^2}{\gamma}} \right) \quad (4.2)$$

$$\alpha = \sqrt{\frac{\cos \theta_i}{\cos \theta_o}} \quad \gamma = \cos \theta_i \cos \theta_o \quad \kappa = \pi n' / \lambda$$

Here,  $n'$  is the index modulation depth. For the special cases of polarizations parallel and perpendicular to the plane of incidence, the dot product in (4.2) can be simplified as:

$$\frac{U_o}{U_i} (d)_\perp = u_\perp = -i\alpha \sin \left( \sqrt{\frac{\kappa^2 d^2}{\gamma}} \right) \quad (4.3)$$

$$\frac{U_o}{U_i} (d)_\parallel = u_\parallel = -i\alpha \sin \left( \sqrt{\frac{\kappa^2 \cos^2 2(\theta_i - \phi) d^2}{\gamma}} \right)$$

The Mueller matrix for the hologram ( $\mathbf{M}_H$ ) and the transformation of the Stokes vector  $\mathbf{S}_i$  are given by

$$\mathbf{S}_H = \mathbf{M}_H \mathbf{S}_i = \frac{1}{2} \begin{bmatrix} u_\parallel^2 + u_\perp^2 & u_\perp^2 - u_\parallel^2 & 0 & 0 \\ u_\perp^2 - u_\parallel^2 & u_\parallel^2 + u_\perp^2 & 0 & 0 \\ 0 & 0 & 2u_\parallel u_\perp & 0 \\ 0 & 0 & 0 & 2u_\parallel u_\perp \end{bmatrix} \begin{bmatrix} I_i \\ Q_i \\ U_i \\ V_i \end{bmatrix} = \begin{bmatrix} I_H \\ Q_H \\ U_H \\ V_H \end{bmatrix} \quad (4.4)$$

For the architecture proposed above, we must describe the diffraction amplitudes from two multiplexed gratings. These gratings must be specially designed so that they have the same Bragg angle  $\theta_B$ . Following our previous analysis,<sup>31</sup> we can design two orthogonal gratings such that they each share the same Bragg angle. The amplitude of the diffracted beam from the  $j^{\text{th}}$  grating is given as:

$$\frac{U_o}{U_i}(d)_j = -i \frac{\kappa_j (\hat{\mathbf{u}}_i \cdot \hat{\mathbf{u}}_{oj})}{\cos(\theta_{oj}) \xi_0} \sin(\xi_0 d) \text{ for } j=1,2 \text{ where} \quad (4.5)$$

$$\xi_0 = \sqrt{\frac{1}{\cos(\theta_i)} \left[ \frac{(\kappa_1 (\hat{\mathbf{u}}_i \cdot \hat{\mathbf{u}}_{o1}))^2}{\cos(\theta_{o1})} + \frac{(\kappa_2 (\hat{\mathbf{u}}_i \cdot \hat{\mathbf{u}}_{o2}))^2}{\cos(\theta_{o2})} \right]}$$

We can evaluate the parallel and perpendicular polarization cases as in (4.3) and obtain the proper coefficients  $u_{\parallel}$  and  $u_{\perp}$ .

The proposed architecture can now be completely analyzed using the Mueller matrices found above. The Mueller matrix for one grating of the hologram is:

$$\mathbf{M}_t = \mathbf{M}_{ES} \cdot \mathbf{M}_H \cdot \mathbf{M}_{FS} \quad (4.6)$$

where  $\mathbf{M}_{FS}$  is the matrix for the front surface, and  $\mathbf{M}_{ES}$  is the matrix for the exit surface. Using (4.1) and (4.4) in (4.6) we find that the transformation of the input Stokes vector is given by:

$$\frac{1}{2} \begin{bmatrix} A+B & A-B & 0 & 0 \\ A-B & A+B & 0 & 0 \\ 0 & 0 & 2\sqrt{AB} & 0 \\ 0 & 0 & 0 & 2\sqrt{AB} \end{bmatrix} \begin{bmatrix} I_i \\ Q_i \\ U_i \\ V_i \end{bmatrix} = \begin{bmatrix} I_t \\ Q_t \\ U_t \\ V_t \end{bmatrix} \quad (4.7)$$

$$A = t_{FS\perp}^2 u_{\perp}^2 t_{ES\perp}^2 \quad B = t_{FS\parallel}^2 u_{\parallel}^2 t_{ES\parallel}^2$$

Equation (4.7) shows the Stokes vector that is diffracted from one grating. The second grating will produce an equation of the same form but with different grating coefficients  $u$ . Both equations have the same Stokes vector as input, but because the grating parameters  $u$  differ, they will produce different output. Note that by using intensity detectors and given the form of the Mueller matrix in (4.7), we can only determine the first two Stokes parameters. In order to determine the other Stokes parameters, we must have a Mueller matrix with non-zero off-diagonal elements in the third and fourth column. This can be achieved, for example, by a

rotation of the holographic grating about the z-axis and by a similar rotation of the polarization axis of the incident light. This simple rotation is described by the following Mueller matrix:

$$\mathbf{M}_{\text{RZ}}(\gamma) = \begin{bmatrix} 1 & 0 & 0 & 0 \\ 0 & \cos 2\gamma & -\sin 2\gamma & 0 \\ 0 & \sin 2\gamma & \cos 2\gamma & 0 \\ 0 & 0 & 0 & 1 \end{bmatrix} \quad (4.8)$$

This is the optimal choice because it can be realized by simply rotating the device when in use. This rotation allows us to find two equations for the two beams diffracted by the first set of multiplexed gratings:

$$\begin{aligned} I_{t1} &= I_i (A_1 + B_1) + (Q_i \cos(2\gamma_1) - U_i \sin(2\gamma_1)) (A_1 - B_1) \\ I_{t2} &= I_i (A_2 + B_2) + (Q_i \cos(2\gamma_2) - U_i \sin(2\gamma_2)) (A_2 - B_2) \end{aligned} \quad (4.9)$$

where the subscripts 1 and 2 denote the two separate gratings. The angle  $\gamma_1$  denotes the angle of rotation for gratings 1 and 2. The next set of equations comes from the beams that pass through the quarter-wave plate and diffract from the third and fourth gratings. The quarter-wave plate adds a  $\pi/2$  phase shift that interchanges the U and V parameters of the Stokes vector:  $\cos(\epsilon) \rightarrow \cos(\epsilon + \pi/2) = -\sin(\epsilon)$  and  $\sin(\epsilon) \rightarrow \sin(\epsilon + \pi/2) = \cos(\epsilon)$ . The second set of equations is rotated an angle  $\gamma_2$  and is thus:

$$\begin{aligned} I_{t3} &= I_i (A_3 + B_3) + (Q_i \cos(2\gamma_1) + V_i \sin(2\gamma_1)) (A_3 - B_3) \\ I_{t4} &= I_i (A_4 + B_4) + (Q_i \cos(2\gamma_2) + V_i \sin(2\gamma_2)) (A_4 - B_4) \end{aligned} \quad (4.10)$$

Because the quarter-wave plate has changed U into V, we now have four equations involving all four Stokes parameters. We are required to measure the four diffracted intensities in order to determine the Stokes parameters. The grating coefficients  $u$  and the Fresnel reflection

coefficients can be measured to find the coefficient A's and B's, which in turn can be used to pre weigh the detector arrays for the imaging process.

To determine the constraints on the device parameters that are required for fully determining the complete Stokes vector, we write equations (4.9) and (4.10) together in matrix form as  $I_t = \mathbf{M}' S_i$ .  $\mathbf{M}'$  is the so-called measurement matrix,  $S_i$  is the input Stokes vector to be solved for, and  $I_t$  are the four measured intensities. For our material parameters, an example measurement matrix is given:

$$\mathbf{M}' = \begin{bmatrix} 0.24320 & -0.04187 & 0.23746 & 0 \\ 0.68596 & -0.03614 & 0.00637 & 0 \\ 0.28996 & -0.04897 & 0 & -0.27773 \\ 0.21291 & 0.11626 & 0 & 0.02050 \end{bmatrix} \quad (4.11)$$

We have verified numerically that this matrix determines the Stokes vector robustly for a range of input values. In the next sections, I show how the optimization of the condition<sup>87, 88</sup> of the matrix affects the robustness of the Stokesmeter.

### **4.3 Volume Grating Requirements**

In order to realize a practical holographic Stokesmeter, the performance of the Stokesmeter must be characterized as a function of its parameters. The polarization dependence of the diffraction efficiency is the most important parameter (and depends itself on many other factors), but others include the type and orientation of the holographic material, the characteristics of the waveplates and other optics used, and the sensitivity, or desired signal-to-noise ratio, of the detectors. In this section, I show the results of work done to understand the various factors that affect the noise tolerance of the Stokesmeter. In pure mathematical terms, the requirement for robust operation in the presence of noise is simple: the measurement matrix

must be well-conditioned. One requirement is that the matrix must be invertible. Other figures of merit have been defined and used to characterize the condition of a matrix,<sup>87, 88</sup> but for our purposes it is enough to simply try to maximize the value of the determinant of the matrix.

Using the Mueller matrix calculus described above, we can combine the effects of the Fresnel reflections, hologram diffraction, and substrate rotate angles into one measurement matrix:

$$\begin{bmatrix} I_{t1} \\ I_{t2} \\ I_{t3} \\ I_{t4} \end{bmatrix} = \begin{bmatrix} A_1 + B_1 & (A_1 - B_1)\cos(2\gamma_1) & (A_1 - B_1)\sin(2\gamma_1) & 0 \\ A_2 + B_2 & (A_2 - B_2)\cos(2\gamma_2) & (A_2 - B_2)\sin(2\gamma_2) & 0 \\ A_3 + B_3 & (A_3 - B_3)\cos(2\gamma_1) & 0 & -(A_3 - B_3)\sin(2\gamma_1) \\ A_4 + B_4 & (A_4 - B_4)\cos(2\gamma_2) & 0 & -(A_4 - B_4)\sin(2\gamma_2) \end{bmatrix} \begin{bmatrix} I \\ Q \\ U \\ V \end{bmatrix} \quad (4.12)$$

The coefficients  $A_i$  and  $B_i$  depend on perpendicular and parallel components of the diffraction efficiency for the  $i$ th grating and  $\gamma_j$  are the angles of rotation.  $I_{t1-4}$  are the four measured intensities that are required, and  $I, Q, U,$  and  $V$  are the four Stokes components to be determined. In order for the matrix in (4.12) to be well-conditioned,<sup>87, 88</sup> the diffraction efficiencies of the four gratings need to be chosen properly along with the other parameters. Given that the coefficients of the matrix in (4.12) depend on polarization-sensitive diffraction, it can be seen that in order to design a robust system, one must be able to control the amount of diffraction for each polarization very carefully. For example, it may be desirable for A-B to be a large negative quantity, which requires a grating that ideally diffracts only p- polarized light. One might also require A-B to be a large positive quantity, requiring a grating that ideally diffracts only s- polarized light. We demonstrate preliminary results for such gratings and show that the polarization dependence of these gratings can be accurately described by coupled-wave analysis.

The derivation of the coupled-wave equations for arbitrary polarization is straightforward and can be found in reference 17. Here we present the result:

$$\begin{aligned}\cos \theta_i \frac{\partial}{\partial z} U_i &= -i\kappa(\hat{u}_i \bullet \hat{u}_d) U_d \\ \cos \theta_d \frac{\partial}{\partial z} U_d &= -i\kappa(\hat{u}_i \bullet \hat{u}_d) U_i\end{aligned}\tag{4.13}$$

Note that for  $\hat{u}_i \bullet \hat{u}_d = 1$ , the equations reduce to the case of perpendicular polarization. The diffraction efficiency for general polarization follows from equation (4.13):

$$\eta = \sin^2 \left( \kappa(\hat{u}_i \bullet \hat{u}_d) \frac{d}{\sqrt{\cos \theta_i \cos \theta_d}} \right)\tag{4.14}$$

For the case of parallel polarization the dot product  $\hat{u}_i \bullet \hat{u}_d = -\cos(2(\theta_i - \phi))$  and the equations for the diffraction efficiency of each polarization are as follows:

$$\begin{aligned}\eta_{\perp} &= \sin^2 \left( \frac{\pi n'}{\lambda} \frac{d}{\sqrt{\cos \theta_i \cos \theta_d}} \right) \\ \eta_{\parallel} &= \sin^2 \left( \frac{\pi n'}{\lambda} \frac{d}{\sqrt{\cos \theta_i \cos \theta_d}} \cos(2(\theta_i - \phi)) \right)\end{aligned}\tag{4.15}$$

One can observe what can be considered a holographic Brewster angle for geometries such that  $\theta_i - \phi = 45^\circ$ .

Studies of the polarization dependence of the diffraction efficiency have been carried out for the case of achieving elimination of one unwanted polarization, using the holographic Brewster angle method, for the purpose of creating holographic optical elements.<sup>89, 90</sup> We are interested in establishing the precision with which the observed polarization diffraction contrast matches the analytic theory. In particular, this requires an indirect determination of the index modulation amplitude from the diffraction efficiency of one polarization. This value is then used to predict the diffraction efficiency at the other polarization, in order to compare with the experimental value.

The Memplex material we use is a dye-doped photopolymer with an index of refraction of 1.482 and a sample thickness of 2 mm. Given the index of this material, it is not possible to achieve the required  $\theta_i - \phi = 45^\circ$  condition using beams incident on the same surface. However, if one were to use a cubic geometry, the condition is easily achievable. The gratings used here were written at 532 nm with writing angles of 52.5 and 57 degrees to produce a slanted grating. Reading was done at the same wavelength and at 57 degrees. Six individual gratings were written using different exposure times. The diffraction efficiency was then measured for various angles of the polarization of the incident read beam. The readout setup is shown in Figure 4-4.

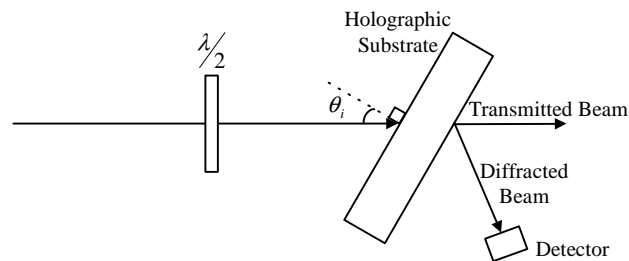


**Figure 4-4: Readout setup**

Theoretical results were calculated using equation (4.15). The value of  $n'$  was calculated using equation (4.15) with measured values of the diffraction efficiency and compensating for Fresnel reflection loss.

The gratings were read at the Bragg angle, so the angles of the incident and diffracted beam are known and were used to determine Fresnel reflections. These reflections were taken into account, and equation (4.15) was used to determine the theoretical diffraction efficiency. The theoretical and experimental results are plotted in Figure 4-5 without using any free fitting parameter.

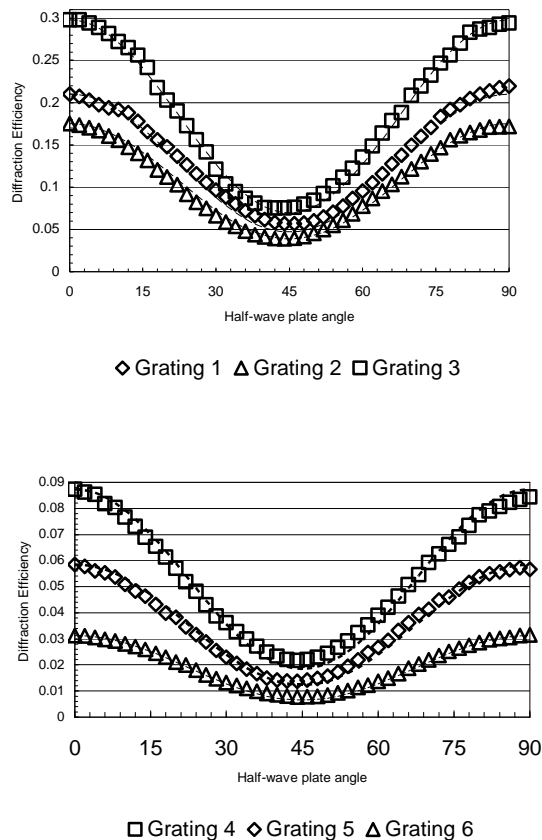


**Figure 4-5: Theoretical vs. Experimental polarization dependence of the diffraction efficiency**

Note that the experimental deviation from the coupled-wave theory is very small. These results also demonstrate a high degree of contrast in diffraction efficiency between the s- and p-polarizations, greater than 70% in some cases.

Two separate numerical simulations were performed in order to simulate the performance of the holographic Stokesmeter in the presence of noise. The first case considered the effect of additive white Gaussian noise (AWGN) added to the four intensity measurements. The measurement matrix is assumed to be known without error. The second case considers no noise in the intensity measurements, but includes noise in the measurement matrix itself. For each of these cases, a variety of Stokes vectors were tested. Shown here are the results for the Stokes

vector  $[1 \ -0.6 \ 0 \ 0.8]$  averaged over 200 runs. Percent error is plotted versus the contrast ratio of the gratings. The grating parameters used in the simulation were in favor of stronger diffraction of perpendicular polarization for the first and fourth grating and in favor of stronger diffraction of parallel polarization for the second and third grating. The rotation angles used were 5 and 40 degrees. Using these grating parameters leads to an improvement of the measurement matrix; however, these parameters do not necessarily represent the optimal set. A more exhaustive search through the entire parameter space is required to fully optimize the measurement matrix. The variance of the noise used was -25, -30, -35, and -40dB compared to a maximum normalized intensity of 1.

The results for case one are shown in Figure 4-6. We see from the figure that as the contrast ratio increases, the average percent error decreases, with limiting gains in the improvement past 50% contrast. These error results are specific to the chosen input Stokes vector, but the general trend is the same for an arbitrary input.

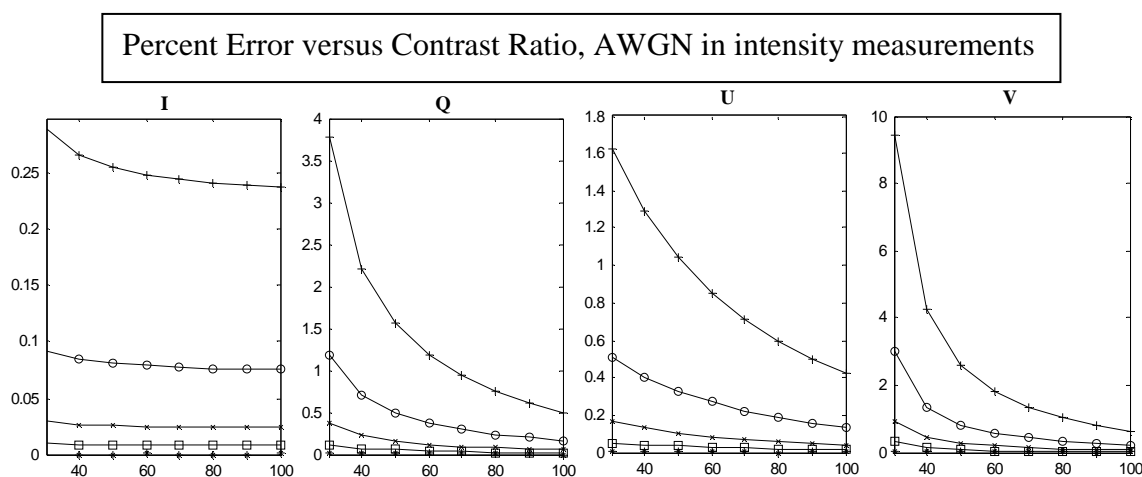


**Figure 4-6: Percent error plotted versus contrast ratio for each Stokes parameter for the case of AWGN in the intensity measurements. The separate lines in each graph represent the different noise levels: +=-25dB, o=-30dB, x=-35dB, □=-40dB, \*=no noise**

The results for case two are shown in Figure 4-7. This case shows the same trend of decreasing error as the contrast ratio increases.

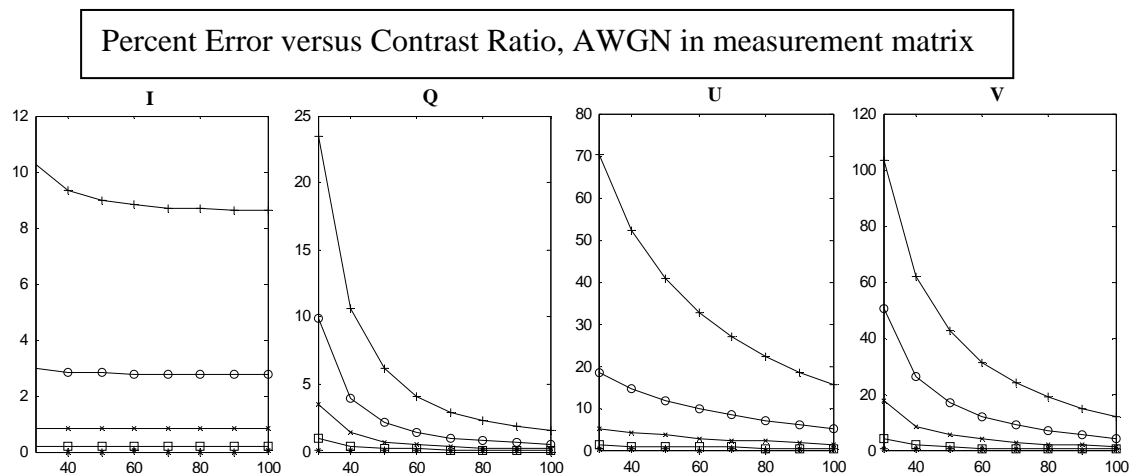


**Figure 4-7: Percent error plotted versus contrast ratio for each Stokes parameter for the case of AWGN in the measurement matrix. The separate lines in each graph represent the different noise levels: +=-25dB, o=-30dB, x=-35dB, □=-40dB, \*=no noise**

Note the unusually large error for contrast ratio values less than 50% in this case. This is due to the fact that the noise is added to the measurement matrix in this scenario, and for average noise values that are larger than the difference between the parallel and perpendicular polarization components of the diffraction efficiency, the sign of the terms  $A_i+B_i$  in equation 1 will change. This can lead to very large errors in the calculation. As the contrast ratio increases, this effect lessens and the percent error rates approach normal values.

As we can see from the data in Figure 4-6 and Figure 4-7, for contrast ratios of greater than 50%, a relatively noise-tolerant holographic Stokesmeter can be constructed depending on the noise level and the desired percent error. The gratings shown here demonstrated a contrast ratio of above 70%, indicating that they will be adequate for use in constructing a preliminary version of the holographic Stokesmeter.

If a further improvement in signal-to-noise ratio is desired, a heterodyne receiver configuration can be easily added to the holographic Stokesmeter architecture. This architecture is illustrated in Figure 4-8.

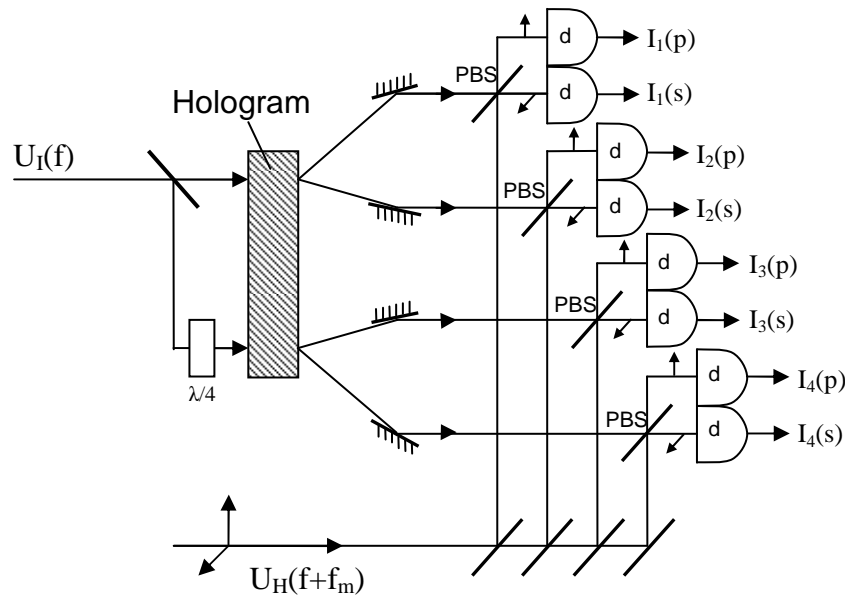


**Figure 4-8: Heterodyne receiver for holographic Stokesmeter**

The four diffracted beams represent the four intensities to be measured. These beams are mixed with a strong local oscillator using polarizing beamsplitters. The local oscillator is chosen to be linearly polarized at 45 degrees so that both the perpendicular and the parallel components of the diffracted light will be mixed with the local oscillator evenly. Each of the eight beams is then sent through a standard heterodyne receiver architecture, and the value of the perpendicular and parallel components of each of the four diffracted beams is recovered. These can then be used in conjunction with the measurement matrix to determine the four Stokes parameters. The heterodyne architecture is advantageous because it can help overcome the system noise and improves the signal-to-noise ratio by providing additional input intensity.

## 4.4 Holographic Beam Combiner for an Active Holographic

### Stokesmeter

In addition to the heterodyne receiver architecture for the holographic Stokesmeter, an active source configuration can also improve the signal-to-noise ratio. In a passive holographic Stokesmeter, the ambient light reflected by the target is used to generate the polarimetric image. If an active source is used to illuminate the target, a larger amount of light can be captured. A holographic beam combiner can be used to create a high-power source by combining several lower-power sources. In principle, an  $N \times 1$  coherent beam combiner (CBC) system with amplification can be implemented with a tree of conventional beam splitters as shown in Figure 4-9.<sup>91</sup>

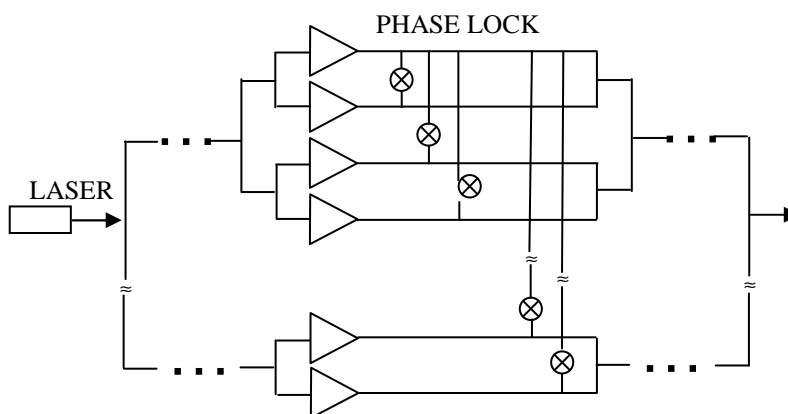


**Figure 4-9: Conventional phase-locked beam combiner system**

At every node of the tree there is a 50/50 beam splitter. The same tree of beam splitters operating in reverse combines the beams. Maximum output is ensured by phase locking, which can be implemented with, for example, electro-optical modulators (EOMs) with feedback. However, a much more robust system that requires fewer optical components can be constructed with coherent holographic beam combiners (CHBC) as shown in Figure 4-10.

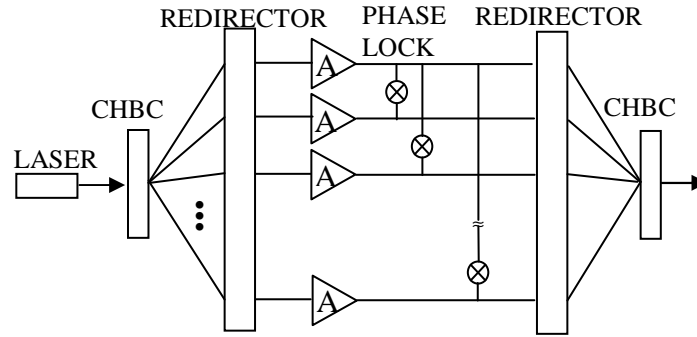


**Figure 4-10: Holographic beam combiner system**

In addition, we will show that a CHBC in our experimental setup can be used as a high precision surface sensor. A CHBC is a holographic structure with  $N$  superimposed common-Bragg-angle gratings that can be prepared by recording the holograms sequentially, with the reference wave incident at a fixed angle and the object wave incident at a different angle for each of the  $N$  exposures.<sup>31, 34, 92, 93</sup>

In this section, we demonstrate a CHBC using volumetric multiplexing of gratings in a thick polymeric substrate. Our experimental results compare well with the theoretical model based on the coupled-wave theory of multi-wave mixing in a passive medium.<sup>6, 9, 33, 94</sup> We assume that the gratings are recorded in a dielectric lossless material that is infinite in the  $x$  and  $y$  directions, and that all waves are propagating in the  $x$ - $z$  plane and are polarized in the  $y$  direction. A grating is described by the grating vector  $\vec{K}_m$  with an amplitude  $|\vec{K}_m| = 2\pi / \Lambda_m$ , where  $\Lambda_m$  is the period of the  $m^{\text{th}}$  grating. Propagation of monochromatic (angular frequency  $\omega$ ) scalar plane waves in the gratings is governed by the Helmholtz equation  $\nabla^2 E(x, z) + k^2 E(x, z) = 0$ , where  $E(x, z)$  is the scalar field assumed to be independent of  $y$ , and  $k$  is the wavenumber. The total electric field in the gratings can be written as:

$$E(x, z) = R(z) \exp(-j\vec{\rho} \cdot \vec{X}) + \sum S_m(z) \exp(-j\vec{\sigma}_m \cdot \vec{X}) \quad (4.16)$$

where  $R$  and  $S_m$  are the amplitudes of the reference and  $m^{\text{th}}$  diffracted waves and  $\vec{X} = (x, y, z)$ .

The wavevectors of these beams are related via the phase-matching equation  $\vec{\sigma}_m = \vec{\rho} - \vec{K}_m$ .

Assuming that  $\vec{\rho}$  is the input wavevector, we define  $|\vec{\rho}| = \beta$ , where  $\beta = (\omega/c)\sqrt{\epsilon_0}$  is the propagation constant in the medium. We restrict our analysis to the Bragg-matching condition, according to which  $|\vec{\sigma}_m| = \beta$ . Using phase-matching terms, in the slowly varying envelope approximation (SVEA),<sup>95</sup> the wave equation reduces to:

$$\begin{aligned} C_R \partial R / \partial z &= -j \sum \kappa_m S_m \\ C_{S_m} \partial S_m / \partial z &= -j \kappa_m R \end{aligned} \quad (4.17)$$

We define the obliquity factors  $C_R$  for the reference and  $C_{S_m}$  for the  $m^{\text{th}}$  diffracted waves as  $C_R = \rho_z / \beta$  and  $C_{S_m} = \sigma_{mz} / \beta$ , and the coupling constant  $\kappa_m = \pi n_m / \lambda$ , where  $n_m$  is the amplitude of spatial modulation of the refractive index defined by  $n(x, z) = n_0 + \sum n_m \cos(\vec{K}_m \cdot \vec{X})$ . The  $m^{\text{th}}$  grating is characterized by the grating strength  $\nu_m = \pi n_m d / (\lambda (C_R C_{S_m})^{1/2})$ , where  $d$  is the thickness of the material. We define the diffraction efficiency of the  $m^{\text{th}}$  grating  $\eta_m = (|C_{S_m}| / C_R) S_m(d) S_m^*(d)$ .

In the beam splitter mode, the input wave  $R$  illuminates  $N$  superimposed gratings at the common Bragg angle and couples into diffracted waves  $S_1 \dots S_N$ . The waves produced by the CHBC have equal and maximum diffraction efficiencies when the  $N$  grating strengths satisfy the condition  $(\sum \nu_m^2)^{1/2} = \pi/2$ . Therefore, the optimal grating strengths are  $\nu_1 = \nu_2 = \dots = \nu_N = \nu = \pi / (2\sqrt{N})$ . From time-reversal symmetry of Maxwell's equations, it follows that a beam combiner must show maximum diffraction efficiency for the same grating strengths that would yield maximum diffraction efficiencies for the beam splitter mode. The

boundary conditions for the gratings in a beam splitter mode at  $z=0$  can be written as  $R(0)=I$ ,  $S_1(0)=S_2(0)=\dots=S_N(0)=0$ . The solutions of the differential equations at  $z=d$  are  $R(d)=\cos(\sqrt{N}\nu)$  and  $S_m(d)=-j(1/\sqrt{N})\sin(\sqrt{N}\nu)$ . We see that when  $N$  superimposed holograms are considered as a single hologram, the effective grating strength is  $\sqrt{N}$  times the individual  $m^{\text{th}}$  hologram grating strength.

In the beam combiner mode the waves  $S_1 \dots S_N$  illuminate the superimposed gratings, each at the corresponding Bragg angle, thus producing a combined diffracted wave  $R$ . In the presence of a linear phase delay between the  $N$  input waves, the boundary conditions at  $z=0$  are  $R(0)=0$ ,  $S_1(0)=I$ ,  $S_2(0)=e^{j\phi}$ ,  $S_3(0)=e^{j2\phi}$ ,  $S_4(0)=e^{j3\phi} \dots S_N(0)=e^{j(N-1)\phi}$ , where  $\phi$  is the phase delay. Defining  $\gamma = \sum (\prod C_{S_m}) \kappa_m^2 / C_{S_m}$ , we obtain the solution at  $z=d$  to be given by  $R(d) = -j [\prod C_{S_m} / (C_R \gamma)]^{1/2} [\sum \kappa_m \exp(j(m-1)\phi)] \sin((\gamma / \prod C_{S_m})^{1/2} d)$ . The intensity of the output wave of a beam combiner is  $I = R(d)R^*(d)$ .

Our holograms were written and read with a frequency-doubled CW Nd:YAG laser operating at 532 nm. We recorded six angle-multiplexed holograms in the photopolymer-based Memplex<sup>®</sup> thick holographic material developed by Laser Photonics Technology, Inc.<sup>27, 96-98</sup> The incident angle of the reference wave  $R$  was held constant during every exposure. The beams  $S_1 \dots S_6$  were recorded at fixed angular intervals. During the readout, the reference beam  $R$  illuminated the holograms at the common Bragg angle, and the beams  $S_1 \dots S_6$  were reconstructed simultaneously. The numerical simulation results for beam profiles are presented in Figure 4-12(a). Figure 4-12(b) and (c) show the experimental transmitted ( $T$ ) and diffracted beam profiles.

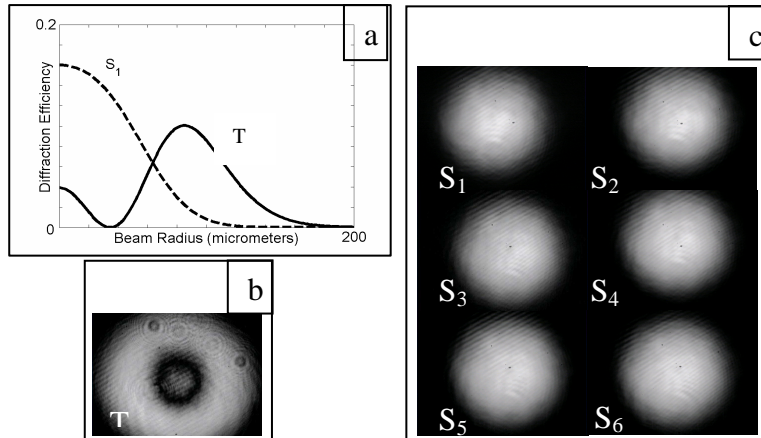


**Figure 4-11: a) Numerical simulation b) Transmitted beam c) Diffracted beams**

We estimated the value of  $\nu = 0.23\pi$  by fitting the numerical simulation curves to the experimentally observed beam profiles. This value is only slightly larger than  $\nu = \pi/2\sqrt{6} \approx 0.204\pi$ , at which the maximum diffraction efficiency is achieved.

The optical setup for demonstrating a six-beam combiner is presented in Figure 3. The input beam from the laser illuminates the hologram in the direction of reference  $R$ . The gratings act as a beam splitter, producing six diffracted waves indicated by solid lines in the diagram. The six waves are collimated by a lens, and reflected by a tilted mirror. The lens is placed a focal length away from both the CHBC and the mirror in order to create a diffraction-free  $4f$  imaging system.

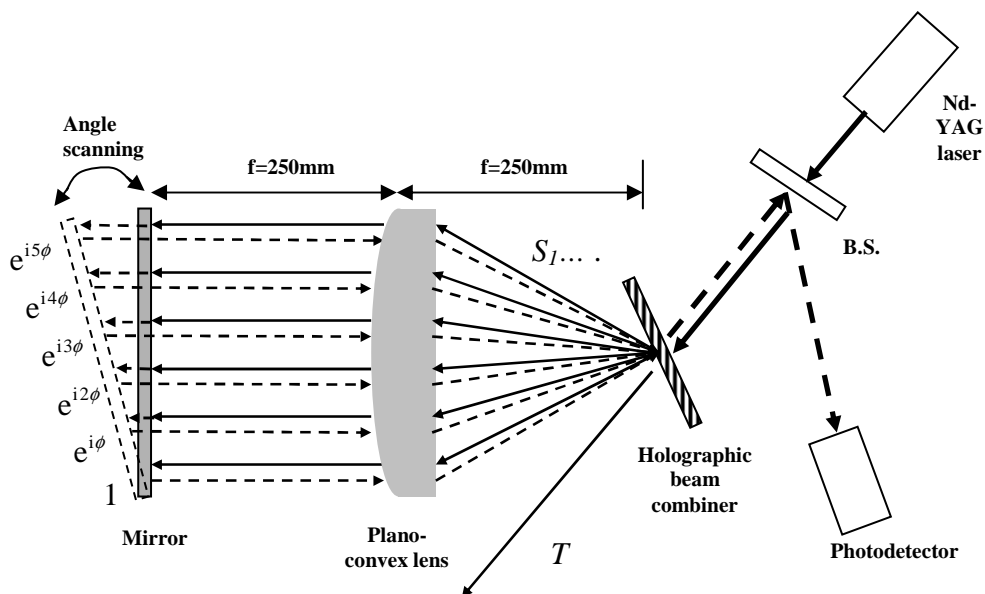
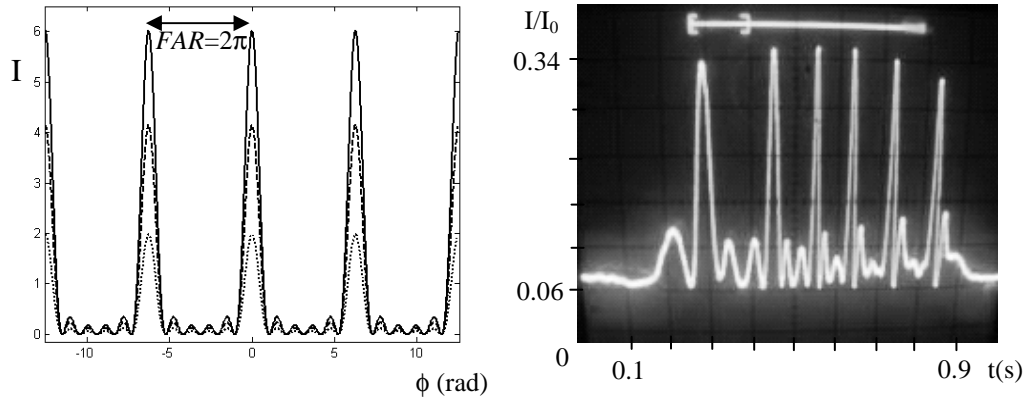


Figure 4-12: Experimental setup for holographic beam combiner

The mirror was rotated with a piezoelectric element by a small angle to vary the phase delay. The angle was small enough so that the reflected beams were Bragg-matched. The beams  $S_1 \dots S_6$  were recorded at fixed angular increments; therefore, the phase delay  $\phi$  between the adjacent waves is a constant for a given angle of the mirror. The six reflected waves represented by the dashed lines illuminate the hologram in the beam combiner mode. The combined beam is partially reflected by a 60% reflecting beam splitter, and monitored by a photodetector.

Figure 4-13(a) shows the numerical simulations of the above equations for the output intensity of a six-beam combiner with unit intensity input beams as a function of the phase delay  $\phi$  for three different values of  $\nu=0.204\pi$ ,  $0.123\pi$  and  $0.08\pi$ .



**Figure 4-13: a) Numerical simulation b) Experimental result**

We see that the intensity profile obtained by solving the coupled wave equations resembles the familiar multiple beam interference pattern. We estimate the finesse ( $F$ ) of the CHBC's by dividing the peak-to-peak angular bandwidth (called free angular range (FAR)) by the half-peak intensity angular bandwidth ( $\Delta\phi_{1/2}$ ). While the maximum intensity varies as a function of  $\nu$ , all three cases have the same finesse value of  $F=6$ . Note that this value is the same as  $N$ , the number of beams combined. This is to be expected, since the finesse of any resonator is directly related to the number of beams that contribute to the peak of the interference curve. Indeed, one can also show analytically that  $F \approx N$  for  $N$  coherent oscillators.<sup>99</sup> Figure 4-13(b) shows the intensity of the partially reflected combined beam measured by the photodetector. We estimate the finesse of this six-beam combiner to be 5.7, which is very close to the theoretical value of 6.

We denote by  $I_0$  the sum of the intensities of the diffracted beams  $S_1 \dots S_6$  measured just after the CHBC when it is operating as a beam splitter. Since  $\nu=0.23\pi$  for our CHBC, the peak of the output intensity of the six-beam combiner is calculated to be  $0.97I_0$ . Because we used a 60% reflection beam splitter (B.S), the detected intensity of the output beam from the six-beam

combiner, corrected for the Fresnel reflection from the hologram's surface, was expected to be  $\sim 0.5I_0$ . However, the height of the largest peak in Figure 4(b) was measured to be about  $0.4I_0$ . The discrepancy with the theoretically expected value is perhaps attributable to the residual imperfections in the experimental process as well as to the inherent assumptions in the coupled-wave theory analysis. For example, while the theoretical model assumes the use of the plane waves, the actual beams employed had transverse intensity distributions that are Gaussian in nature. In addition, the analysis assumes perfect Bragg matching which is difficult to achieve experimentally.

To summarize, we demonstrated a CHBC for six beams at 532 nm using volumetric multiplexing of gratings in a thick polymeric substrate. Our experimental results compare well with the theoretical model based on the coupled wave theory of multi-wave mixing in a passive medium. This work could be used to create a high-power source for an active holographic Stokesmeter, creating an all-holographic active polarization imaging system.

#### ***4.5 Conclusion and Next Steps***

The work that is documented here represents the development of a fundamental concept, the holographic Stokesmeter, towards a useful, realizable device. Work has been done to show the limitations and requirements of the device under noise, as well as to improve the performance of the device by adding an active light source. This work helped to form the foundation of our group's efforts in developing a holographic Stokesmeter, and my colleague Dr. Jong-Kwon Lee has continued this work and developed the imaging properties of the holographic Stokesmeter, as well as a spectrally-resolved Stokesmeter and a photonic-bandgap-based Stokesmeter that has the potential to operate at many wavelengths and to be the key component in a polarization-

discriminating laser radar (LADAR).<sup>18, 19, 21</sup> This polarization-discriminating LADAR could be used to add polarization sensitivity to a holographic smart eye, which is itself described in Chapter 8. Future work on the holographic Stokesmeter will center on the development of a Stokesmeter that operates in the same band as LADAR. Such a polarization sensitive LADAR could then be used to acquire query images for a holographic smart eye. This application is discussed in more detail in Chapter 8.

## 5 Super Parallel Holographic Architectures

### 5.1 Introduction

In many situations, it is necessary to identify a target rapidly.<sup>100</sup> For DoD scenarios, a target is typically detected using a synthetic aperture radar (SAR). This image is then compared with images stored in a database in order to ascertain the identity of the object in question. There are many techniques for performing this task. One technique employs digital signal processing (DSP),<sup>101</sup> wherein a DSP chip or a dedicated electronic circuit is used to compare the images bit-by-bit serially, thereby identifying the image with the highest degree of correlation to the target image.

An important alternative to this approach is a holographic optical correlator (HOC), which takes advantage of the inherent parallelism of optics. Specifically, the images comprising the database are stored in a hologram, via angular multiplexing. Using a spatial light modulator (SLM), the target image is transferred to an optical beam, which in turn illuminates the hologram while scanning its angle of incidence. If a match is found, a bright correlation beam is produced in a pre-specified direction, thereby identifying the target-match.<sup>32, 102</sup> HOCs are employed for many optical signal processing applications, including in pattern and character recognition, in computer/robotic vision for object tracking, and in the implementation of artificial neural networks.<sup>103-106</sup>

HOCs can perform correlations nearly three orders of magnitude faster than typical DSP-based correlators. This increase in speed results from the fact that in the HOC the bits are compared in parallel. However, the HOC is limited in terms of the number of images that can be queried at one time. Specifically, the maximum number of images that can be stored in a single

spatial location via angular multiplexing is typically limited to a few thousands.<sup>36, 37</sup> This problem can be overcome by spatial multiplexing, whereby different sets of images are stored in different spatial locations. Using a large holographic substrate, it may be possible to employ more than one thousand different spatial locations. A disadvantage of this approach is that the substrate must be translated in two dimensions in order to provide access to each location, thereby slowing down the effective speed of correlation significantly.

We have developed an architecture that overcomes this limitation.<sup>28, 30</sup> Specifically, we propose a design wherein the query image is split into many copies. This is performed by a highly efficient holographic multiplexer/demultiplexer (HMDX), which is produced by writing multiple high efficiency Bragg gratings in a thick substrate, with a common reference beam and multiple object beams at varying angles. Thus, multiple query images are formed, and each is presented to a different spatial location in the holographic memory unit (HMU). A series of optical elements are then used to decipher the resulting diffraction patterns. The net result is that the images in all the memory locations are queried, and a potential image match is achieved in the same amount of time it takes for the conventional HOC to query the images at one location. This super-parallel holographic optical correlator (SPHOC) exhibits a parallelism beyond that of conventional optics.

In addition, the SPHOC can be employed as a super-parallel holographic random-access memory (SPHRAM) by reversing the direction of the beams inside it. By running the SPHOC in reverse, a high-speed holographic memory can be created. Both the SPHOC and SPHRAM require a specialized optical component, the lenslet array. In this chapter, I summarize the work that has been done to realize this component and both the SPHOC and SPHRAM architectures.

## 5.2 Super Parallel Holographic Optical Correlator

### 5.2.1 Architecture

The architecture of the super parallel holographic optical correlator is designed to allow the correlation operation to take place at each (or many of) the spatial locations in a holographic database. Specifically, we propose a design wherein the query image is split into many copies. This is performed by a highly efficient holographic multiplexer/demultiplexer (HMDX), which is produced by writing multiple high efficiency Bragg gratings in a thick substrate, with a common reference beam and multiple object beams at varying angles. Thus, multiple query images are formed, and each is presented to a different spatial location in the holographic memory unit (HMU). A series of optical elements are then used to decipher the resulting diffraction patterns. The net result is that the images in all the memory locations are queried, and a potential image match is achieved in the same amount of time it takes for the conventional HOC to query the images at one location. This SPHOC exhibits a parallelism beyond that of conventional optics.

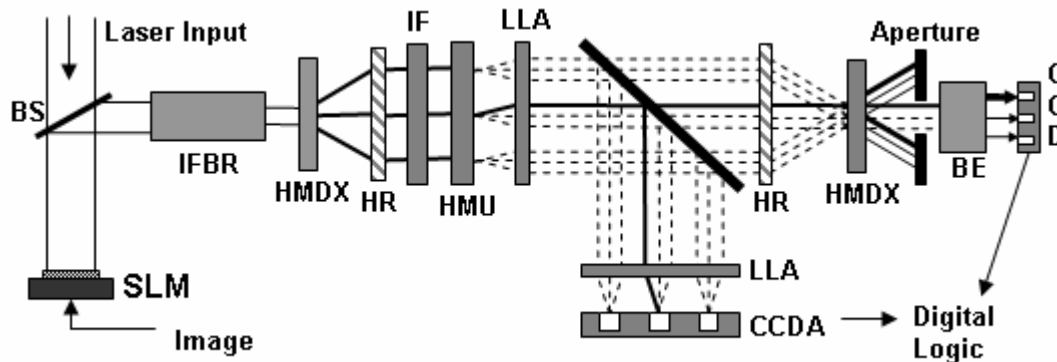


Figure 5-1: SPHOC Architecture

The architecture of the SPHOC is shown in Figure 5-1. This figure is a schematic only, not a representation of the actual dimensions or angles of the components or system. A laser

beam is sent to a SLM to pick up the query signal. Once the query image is imprinted on the optical beam, it is directed by a beamsplitter through an image flattening beam reducer (IFBR) which resizes the image and directs it towards a holographic multiplexer/de-multiplexer (HMDX). This component of the SPHOC is responsible for splitting the image into multiple copies (one for each spatial location). A holographic redirector (HR), which can also be a prism or other angle-changing optic, directs the beams to the holographic memory unit (HMU). Each spatial location of the HMU has many holograms stored using angle-multiplexing, and each location is being addressed simultaneously. Any correlations produced will exit the HMU at the angle at which they were recorded. A lenslet array then collects these correlation beams which are then split into two components using a beam splitter. One component gets focused by another lenslet array (LLA) onto an array of CCD elements (CCDA). Identifying the position of the detector element that sees the highest signal yields the information about the spatial location of the matching image. The other part of the beam goes through another HR. This HR redirects all the incident beams to a central point, without focusing the beams coming from the same spot with respect to one another, as shown.

These beams are now passed through another HMDX, which is identical to the one used at the input, but now operating in reverse. However, the reverse operation has the potential problem that additional beam patterns (weaker than the one generated along the axis) will also be produced. A simple aperture can be used to eliminate these unwanted beams. After the aperture, a beam expander is used to match the size of the second CCD array. The position of the element of the CCD that sees the brightest signal yields the information about the angle of the matched image. Data obtained from both CCD arrays, properly thresholded, can be sent through a digital logic circuit to identify the image that is matched.

## 5.2.2 Preliminary Experimental Data

Our experimental results were obtained using Memplex™ material produced by Laser Photonics Technologies in Amherst, MA. This material and variant thereof have been used previously for memory storage and non-spatial filtering applications. The substrates were 3.7 cm x 3.7 cm in lateral area and 2 mm thick. Our holograms were written and read using a frequency doubled Nd:YAG laser operating at 532 nm.

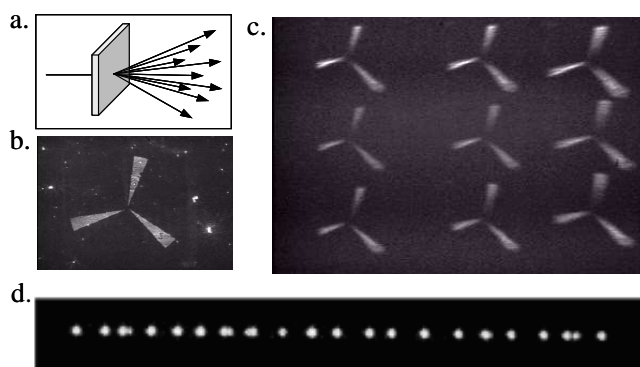


**Figure 5-2: HMDX test**

Figure 5-2 displays experimental images from two HMDXs that we produced. Figure 5-2 (a.) is a schematic of the 3x3 HMDX working as a 1x9 splitter. Figure 5-2 (b.) is a CCD capture of the SLM image that was used to illuminate the splitter, and (c.) is an image of the resulting output. The irregular bright spots in the background of Figure 5-2 (b.) is due primarily to dust contamination of the SLM surface and imaging optics. The irregular spacing of the far right column of images in Figure 5-2(c.) is a result of the imaging optics and was not due to the HMDX. Figure 5-2 (d.) is an image of the output of a 1x20 HMDX when it was illuminated with a plane wave beam.

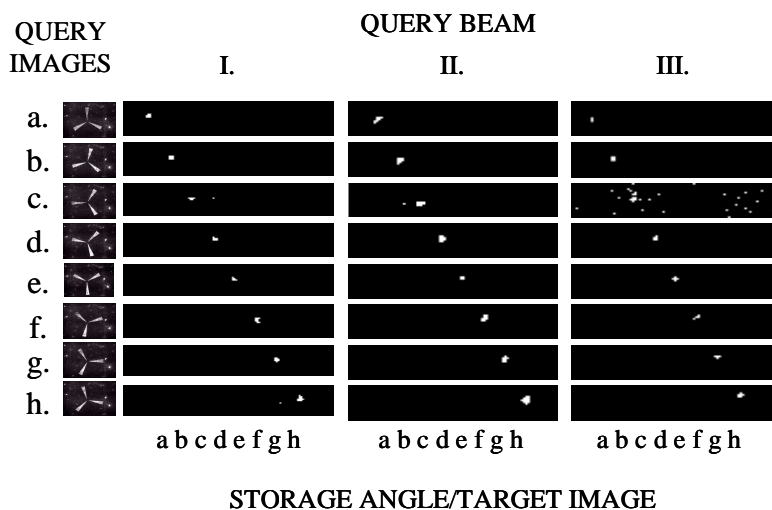


**Figure 5-3: SPHOC Initial Results**

Figure 5-3 displays experimental images obtained during testing of the HMDX and HMU components of the SPHOC architecture. The SLM query image was routed through a 1x3 HMDX. The three resulting images were then used to query three separate HMU locations, each containing an identical set of images. The column on the far left displays the query image used during correlation. The other three columns in Figure 5-3 display data collected using each of the three query beams. The eight images in each column are CCD captures of the diffracted beams that emerged from the HMU during correlation. The letters at the bottom of each column indicate the location of the diffraction spot that corresponds to a stored image. Taking the top image in column I. as an example, we see that image (a.) has excited a diffraction spot in position (a.) which is the matching image. The data clearly shows that the appropriate diffraction beam, or spot is being excited by each query image which demonstrates the way our architecture will identify the target images.

### **5.2.3 Conclusion**

Although the SPHOC architecture showed great promise with its ability to correlate in multiple locations at once, there are fundamental issues with the architecture that will most likely prevent it from maturing. One drawback of the design is that the correlation is performed in a thick media (the HMU) so that the correlation is not translation-invariant. A more serious problem is encountered when multiple partial correlations are considered. In the architecture described here, a number of partial correlations could possibly cause a false positive, or outweigh a true correlation. Although there may ultimately be a viable solution to these issues, we have instead focused on the very interesting system that is obtained by running the SPHOC “in reverse”.

## ***5.3 Super Parallel Holographic Random Access Memory***

### **5.3.1 Architecture**

The principle of operation of Super-Parallel Holographic Random Access Memory (SPHRAM) is similar to that of an SPHOC operated in reverse. The SPHRAM is shown in Figure 5-4.

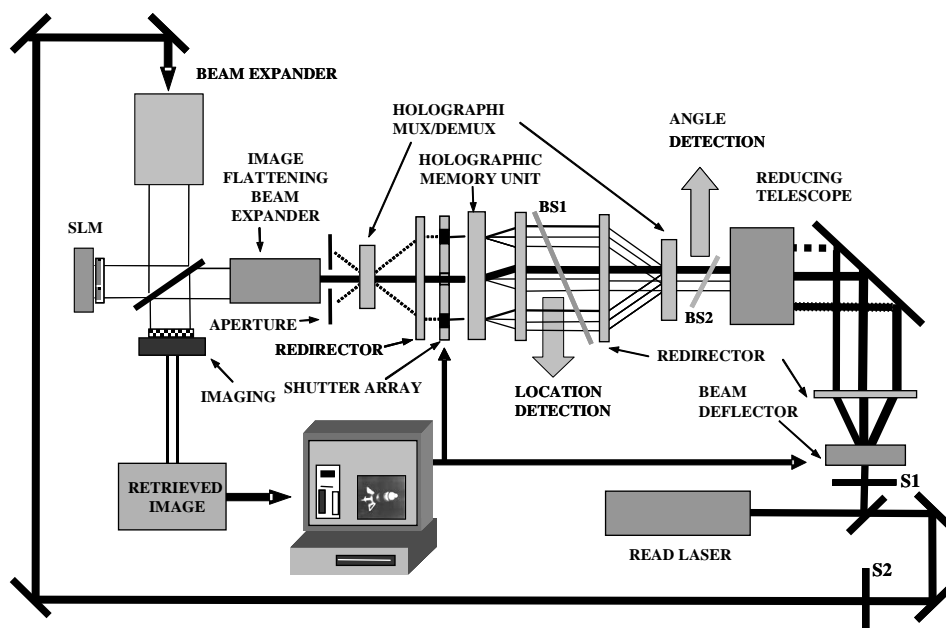


**Figure 5-4: SPHRAM Architecture**

During the SPHRAM operation, shutter S1 is open and S2 is closed. The HMU is recorded with the database of interest, using multiple spatial locations, each of which contains a set of images that are angularly multiplexed in two dimensions. When operating the RAM, the user enters the coordinates corresponding to the spatial position and the angle of storage for the image of interest. The position coordinate is used to open the corresponding element of a shutter array. The number of elements in the shutter array is the same as the number of spatial locations in the HMU, and the locations are matched. Shutter arrays of this type are available commercially, using individually addressable ferroelectric liquid crystals or MEMS based microdeflectors that can have fast switching times. Alternatively, one can use a two photon memory, such as bacteriorhodopsin, as a shutter, in which only the location of interest is illuminated by the activation laser frequency. These types of shutters can be stacked serially to provide the desired suppression ratio.

The angular coordinate for the image is sent to a beam deflector (e.g., a pair of acousto-optic deflectors), which orients the read beam at the desired angle, which in turn is translated to a specific position by the redirector. A combination of the reducing telescope, holographic multiplexer, redirector, and the lenslet array produces a copy of the read beam simultaneously at each of the locations on the HMU. The image stored at this angle would be recalled from each spatial location. The shutter array would block all but one of these images, and the redirector and the de-multiplexer would send the desired image on to the CCD camera.

### 5.3.2 Experiment

To demonstrate the feasibility of an SPHRAM, we used a simplified geometry as shown in Figure 5-5. A pair of galvo-mounted mirrors was used for deflection. The database comprised of an HMU with images multiplexed at 9 locations in a 3X3 arrangement.

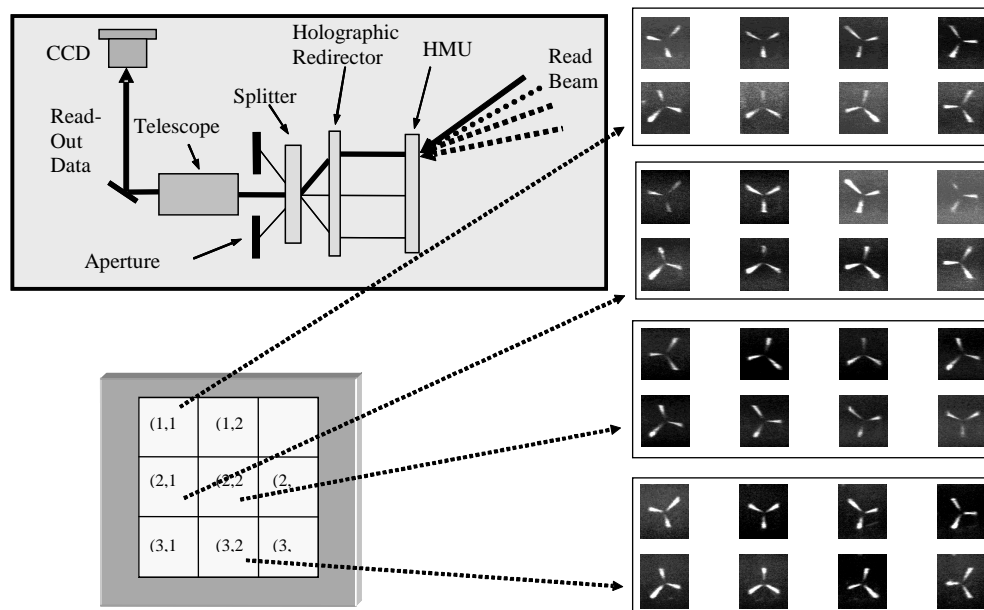


**Figure 5-5: SPHRAM Feasibility Experiment**

Each location contained 8 images multiplexed in one angular dimension. A holographic redirector and a multiplexer are used in the setup for producing the read beam. The bottom of

Figure 5-5 shows a typical set of 8 image data retrieved from the spatial location (3,2) using this setup. Similar data were also retrieved from the other locations.

### 5.3.3 Conclusion

The SPHRAM architecture has the same potential performance enhancements as the SPHOC; namely, that by bringing the read beams to each spatial location simultaneously, a large speed advantage can be realized. However, because in the SPHRAM a single image in one spatial location is desired, a set of electro-optic shutters can eliminate the unwanted interference that plagues the SPHOC design. In addition, because no correlation is being performed in the holographic memory unit, the thickness of the material is not constrained to be small enough to allow translation invariance.

The SPHRAM has the potential to be a high-speed memory for any type of all-optical processor. In Chapter 8, I discuss the specific application of the SPHRAM as the database source for a real-time optical correlator. In order to fully explore the potential capabilities of the SPHRAM, the full architecture must be developed. The feasibility experiment demonstrated approximately half of the architecture: readout of the HMU to the CCD camera. However, a non-trivial optical element, the lenslet array, plays a crucial role in allowing the *simultaneous* access to each spatial location. I will examine this component in greater detail in the next section.

## **5.4 Lenslet Array**

### **5.4.1 Introduction**

Here we examine the key component of the SPHOC/SPHRAM architecture, the lenslet array.<sup>20</sup> Although in our original design a single lens was used to represent the functionality of the lenslet array and bulk optics were used for the experiment, for a demonstration of the complete architecture a more complex structure is required.

In the case of the SPHOC, a single lens placed after the HMU in Figure 5-1 would be able to resolve any of the diffracted correlation beams. Each beam has a different angle, which would lead to an array of possible correlation spots in the focal plane of the lens. However, in order to determine the angle and location that is matched, the diffracted beams must pass through the rest of the architecture as shown in Figure 5-1 and described in reference.<sup>30</sup> For this, a more complicated lens structure is needed. For the operation of the SPHRAM, a single lens is not able to translate position to angle without also focusing the beam. Because spherical wave readout is not desired for the SPHRAM, this also indicates that a more complex optical device is necessary.

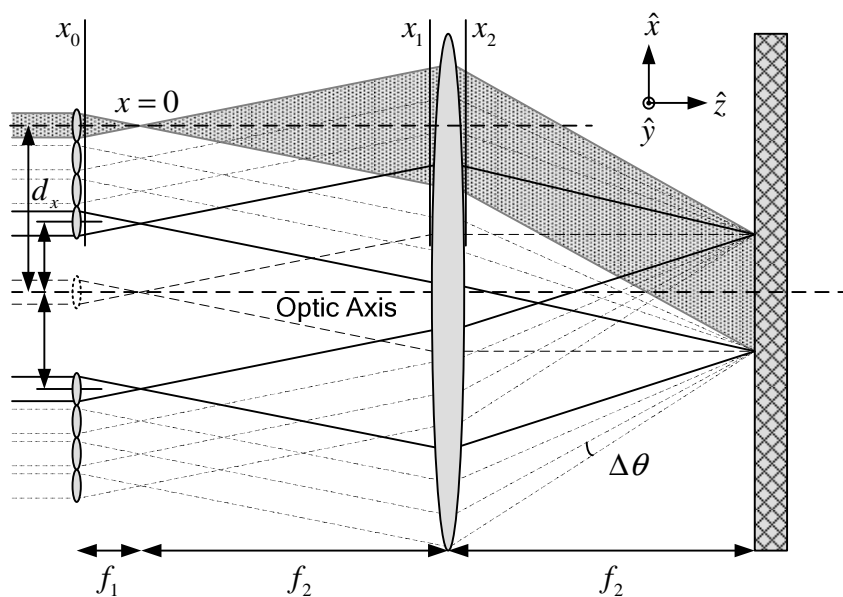
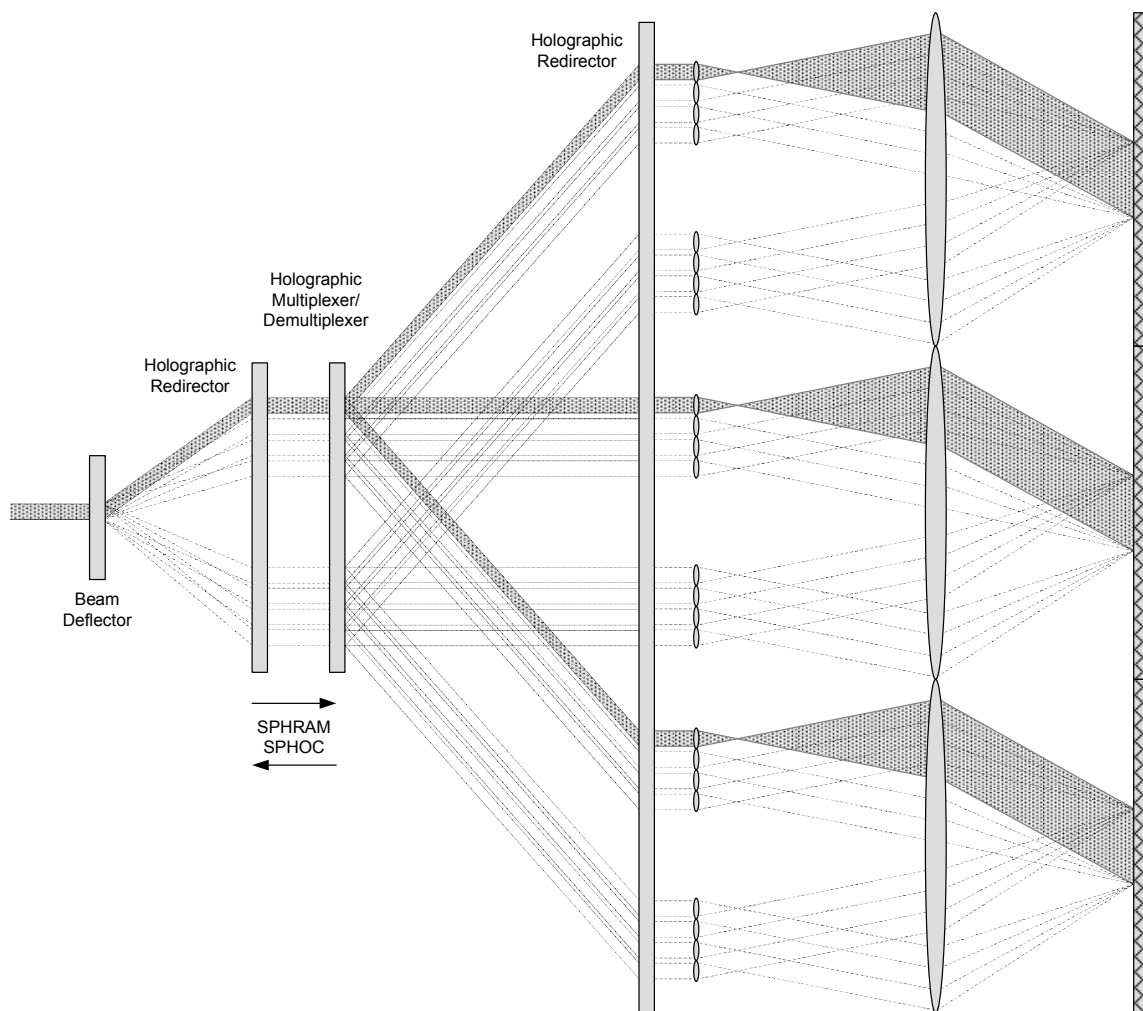


Figure 5-6: Details of a “unit cell” of the lenslet array

Figure 5-6 illustrates one unit of the LLA that corresponds to one spatial location of the HMU in an SPHRAM. The array of the lenslets is at  $z = 0$ , and there is a collection lens at  $z = f_1 + f_2$  to collect and collimate the reference beams and translate each beam's position into an angle. The optic axis is shown as a dashed line through the middle of the figure. The large collection lens will angle the beams according to their individual spatial frequencies as well as collimating them. On either side of the optical axis ( $z$ -axis), each angle must differ from its corresponding angle on the opposite side by an amount greater than the angular bandwidth of the HMU to avoid Bragg degeneracy. In other words, for the two beams shown in Figure 5-6 as solid lines, the lenslet on the  $+x$  side of the optic axis must be at a different distance than the corresponding lenslet on the  $-x$  side of the optic axis. In this manner, no angles will be repeated, and any two angles are at least  $\Delta\theta$  apart, where  $\Delta\theta$  is chosen based on the Bragg angle selectivity of the HMU.

Each spatial location of the HMU has a corresponding unit of the LLA to redirect and collimate the possible correlation beams. An example of a three spatial location HMU and corresponding LLA is shown in Figure 5-7.



**Figure 5-7: LLA in a 3-spatial-location HMU SPHOC/SPHRAM architecture. Beams propagate left to right for SPHOC operation, and right to left for SPHRAM operation.**

#### 5.4.2 Phase Transformation for Plane Waves

We use Figure 5-6 to analyze the phase transformation the diffracted beam undergoes as it propagates through the PCLLA. We consider a single spatial location with diffracted beams in two dimensions. The analysis proceeds left to right. The  $z$ -axis ( $x=0, y=0$ ) is presumed to run

through the center of the lenslet being analyzed. The beam path is shaded in the figure. The lenslet is allowed to be positioned anywhere in the  $x$ - $y$  plane, although the figure shows only the  $x$ - $z$  plane. A plane wave is incident on the lenslet with a focal length  $f_1$ . This lens imparts a quadratic phase to an incoming beam:

$$t_{lens}(x) = \exp\left(-i \frac{k}{2f_1}(x_0^2 + y_0^2)\right) \quad (5.1)$$

The field just before the collection lens ( $z = f_1 + f_2$ ) is given by:<sup>32</sup>

$$U_1(x_1, y_1) = \frac{e^{ikz}}{i\lambda z} e^{i\frac{k}{2z}(x_1^2 + y_1^2)} \iint U_0(x_0, y_0) e^{i\frac{k}{2z}(x_0^2 + y_0^2)} e^{i\frac{2\pi}{\lambda z}(x_1 x_0 + y_1 y_0)} dx_0 dy_0 \quad (5.2)$$

After completing the integration, we find that the field distribution is:

$$U_1(x_1, y_1) = \exp\left(i \frac{k}{2f_2}(x_1^2 + y_1^2)\right) \quad (5.3)$$

The collection lens imparts another quadratic phase factor; however this lens is off-axis with respect to the lenslet and so the modified phase factor is:

$$t_{lens}(x_2) = \exp\left(-i \frac{k}{2f_2} \left[ (x_2 - d_x)^2 + (y_2 - d_y)^2 \right] \right) \quad (5.4)$$

where  $d_x$  and  $d_y$  are the displacement from the optic axis in the  $x$  and  $y$  directions respectively. Expanding the quadratic term in equation (5.4), we find that the lens imparts a quadratic phase, a linear phase, and a constant phase:

$$t_{lens}(x_2) = \exp\left(-i \frac{k}{2f_2} \left[ (x_2^2 - 2x_2 d_x + d_x^2) + (y_2^2 - 2y_2 d_y + d_y^2) \right] \right) \quad (5.5)$$

We ignore the constant phase term, and the quadratic term exactly cancels the quadratic phase from the incoming beam in equation (5.3). The field after the collection lens is:

$$U_2 = \exp\left(i \frac{k}{f_2} (d_x x_2 + d_y y_2)\right) \quad (5.6)$$

We can express the complex amplitude of a plane wave traveling at an angle  $\theta$  by  $U = \exp(i2\pi v_x x) \exp(i2\pi v_y y)$ , where  $v_i = \sin \theta_i / \lambda$ ,  $v_x$  corresponds to the spatial frequency (angle) in the x direction, and  $v_y$  represents the spatial frequency (angle) in the y direction. Using this result, we recognize the phase distribution in equation (5.6) as a plane wave traveling at an angle  $\sin \theta_x = d_x / f_2$  with respect to the x-axis and  $\sin \theta_y = d_y / f_2$  with respect to the y-axis. In the paraxial approximation, this means that the beam from the lenslet will be collimated by the collection lens and angled so that it passes the z-axis at  $z=f_1+2f_2$ .

For an ideal thin collection lens with a parabolic phase delay, every beam will be redirected to the same spatial location. However, for a real system, any deviation from the thin lens idealization may introduce undesired effects. We have used a ZEMAX simulation, as described next, to study effects of such imperfections.

### 5.4.3 ZEMAX Simulation

Using the ZEMAX optical simulation program, we developed a custom surface type that would allow a lenslet array. We chose to design a lenslet array of 33 lenslets, each with a diameter of 30 microns and an F/# of approximately 10. For the simulation purposes, we used lenslets in one dimension only. The first simulation was done using the lenslet array and a collection lens with a diameter of 2 mm and a focal length of 4.86 mm using the paraxial surface type in ZEMAX. This allowed greater than 15x magnification of the input reference beam for a final spot size of 0.5 mm and simulated an ideal thin lens. The second and third simulations were done with a spherical bi-convex and plano-convex collection lens, respectively, of the same

diameter and focal length as the paraxial case. Finally, the fourth simulation used an aspheric lens.

Because the collection lens is used to collimate each beam to the same on-axis spatial location, the primary imperfection is due to spherical aberration. A plot of the  $W_{040}$  Seidel aberration coefficient for spherical aberration (measured in units of the tested wavelength, 532 nm) is shown in figure 5. As shown in the figure, for the paraxial lens case, spherical aberration is essentially zero, as expected. For bi-convex and plano-convex lenses however, it is nonzero with little difference between the two. Using an aspheric surface can virtually eliminate spherical aberration, and the aspheric collection lens clearly offers the best design. With aspherical lens shaping techniques becoming more widespread, this design is also feasible for implementation.

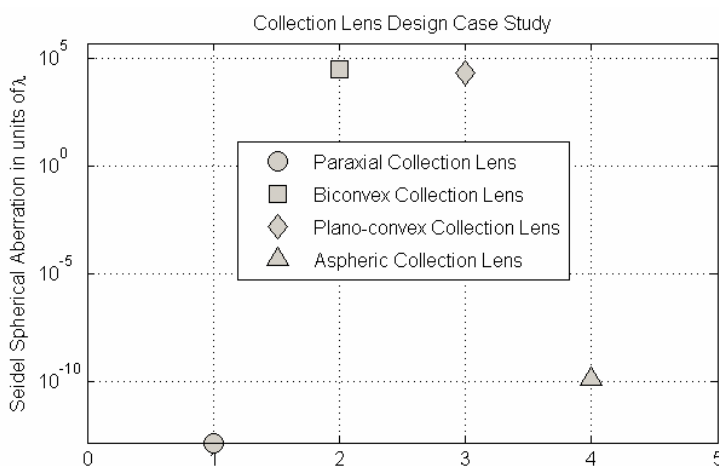


Figure 5-8: Seidel spherical aberration coefficient for each of four designs

#### 5.4.4 Conclusion

In conclusion, we have proposed a design for an LLA that will play a key role in super-parallel architectures for a holographic correlator/RAM. We have performed the analysis of the

required phase transformations of the beams using the Fourier optics approach. A lithographic LLA coupled with aspherical collection lens will provide the required performance. Current commercially available micro-optical manufacturing techniques can produce closely-packed lenses as small as 20 microns in diameter, and the industry is moving towards even smaller feature sizes. Techniques are available to make refractive and diffractive micro lenses in one- and two-dimensional arrays.<sup>107-111</sup> Using an aspheric lens as the collection lens can eliminate the problem of spherical aberration.

## **5.5 Conclusion and Next Steps**

The super-parallel architectures described here can offer a huge performance gain to any spatially-multiplexed holographic memory. The key component is an LLA with an aspheric collection lens. This component has been fully described here and can now be implemented. Lenslet arrays and aspheric lens can be ordered using the data analysis performed in ZEMAX and shown here. Once the LLA is manufactured and tested, the full architecture of the SPHOC/SPHRAM may be implemented.

Because of the lack of translation-invariance and the complex problems facing accurate correlation when non-orthogonal images are searched, the SPHOC will not likely be a useful tool for high-speed database search. However, the SPHRAM has the potential to become a very high-speed holographic memory. This type of memory can be used as the source database for a real-time optical correlator. Because the holographic database is separate from the correlator, the correlator itself can use a thin material and thus perform translation-invariant correlations. This “holographic smart eye” can be used for the same applications as described here for the SPHOC. A working prototype of the smart eye was developed and is discussed in Chapter 8.

## 6 Disc-based Holographic Memory System

### 6.1 Introduction

The SPHRAM can be used to create a high-speed real-time holographic smart eye. The SPHRAM serves as the high-speed image database for this search system, while a real-time Vanderlugt correlator performs the translation-invariant correlations. Chapter 7 details the efforts to develop the real-time correlator, while the SPHRAM is still being developed, as described in Chapter 5. Concurrently with the development of the SPHRAM, we have constructed a disc-based holographic memory system to fulfill the needs of the real-time correlator.

Several institutions and corporations, most notably the PRISM and HDSS consortiums, have already created read-only holographic memory systems.<sup>13, 17, 112-116</sup> Their body of research is extensive, and we have tried to incorporate proven methods and techniques where resources permit.<sup>12, 15, 16, 38, 105, 117-138</sup> However, the focus of this project was not to create a state-of-the-art holographic data storage system—the SPHRAM can potentially exceed the performance of those systems once it is complete. Rather, it is to determine the viability of a real-time correlation system using a variety of materials and techniques. In order to advance this goal, we have created a disc-based holographic memory. The following purposes are served by this: First, it serves as a holographic database providing images for use in the real-time correlator. The SPHRAM design has a higher potential performance, but before the SPHRAM can be built, the LLA component must be built and tested. During this time, the real-time correlator can be tested using a simpler disc-based holographic memory.

Second, the disc-based holographic memory system allows the exploration of various materials available for usage as HMUs. The system was designed with three materials in mind: the Aprilis CROP media, the Memplex polymer media, and our own LAPT disc media. Any media that can be mounted onto a standard CD-ROM size mount can be used in the system.

Finally, the system allows for the testing of different holographic multiplexing techniques, most notably angle-multiplexing and shift-multiplexing. The system described here uses angle-multiplexing, but can be easily expanded to include shift multiplexing with the addition of a few optical elements.

The holographic disc memory is a read-only memory. There is currently active development of erasable, read-write, holographic materials. However, at this time there are none that are commercially available, nor are the developmental materials ideal for a robust holographic disc-based memory system. Although a read-write holographic memory system would add a certain degree of engineering complexity to the system, the bulk of the research issues and performance benchmarks can be accomplished with a read-only system.

## **6.2 *Design Overview***

### **6.2.1 Write Architecture**

The holographic memory disc writing architecture is shown in Figure 6-1. The system is controlled by a computer program running on a standard personal computer. The user interface is at the left of the diagram. Positioning offsets can be set to control the exact position of the disc relative to the writing beams. The user chooses which image data is to be written in which locations, as well as the number of locations on the disc to write and the start and end locations. In this way, portions of the disc may be written separately. An exposure schedule can also be

specified. Once the user parameters are set, the recording may begin. The write architecture is composed of a rotation stage to spin the disc, a translation stage to move along the axis of the disc, two galvanometer mirrors to change the angle of incidence of the reference beam for angle multiplexing, a spatial light modulator, and a shutter to control the exposure times.

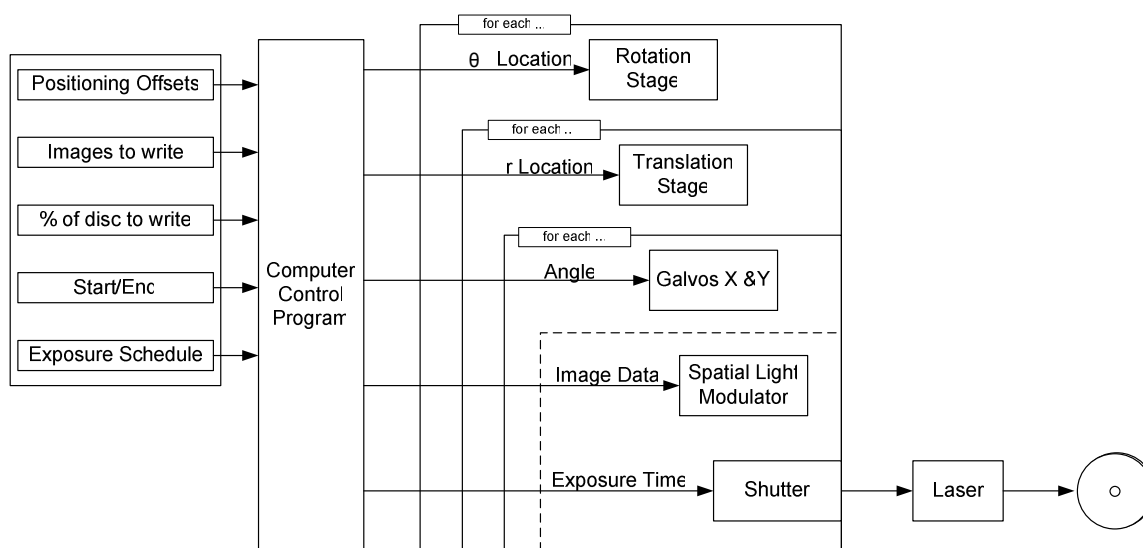


**Figure 6-1: Block Diagram of the Write Architecture**

A typical recording would proceed as follows. After entering the required user data, the computer control program automates the rest of the recording process. The rotation stage spins the disc to the first  $\theta$  position, and the translation stage moves to the first  $r$  position (each recording location is specified in polar coordinates). At each recording location, the control program sets the galvo mirrors into their start position. Image data is sent to the SLM, and after a short delay to allow the electronics to present the SLM screen with the image data, the shutter is opened. The amount of time for each exposure is controlled by the computer control program, which reads the exposure data from the file provided by the user and sends the correct exposure time to the shutter. When the shutter is opened, half of the laser light illuminates the SLM and

carries the image data to the disc, while the other half traverses a path through the galvo mirrors and creates a reference beam. Both beams are incident on the disc at the writing location, and a hologram is created. The control program then closes the shutter, moves the galvos to the next location, changes the data on the SLM screen to the next image, and then opens the shutter for the next exposure. This process is repeated until all the images for the location are written. The translation stage is then moved to the next axial position, and the process is repeated. When all axial locations are completed, the rotation stage moves to the next  $\theta$  position, and the entire process repeats until the recording is complete.

### **6.2.2 Read Architecture**

The read architecture of the disc-based holographic memory system is described here. A block diagram of the system is shown in Figure 6-2. The read architecture consists of a control program running on a personal computer. The control program has a user interface from where the user may select a location at random to read data. The control program takes the location information (angle, position, and galvo angle), and sends the appropriate commands to the motion stage hardware and galvo controller. A CCD camera captures the image output and sends it to the control program.

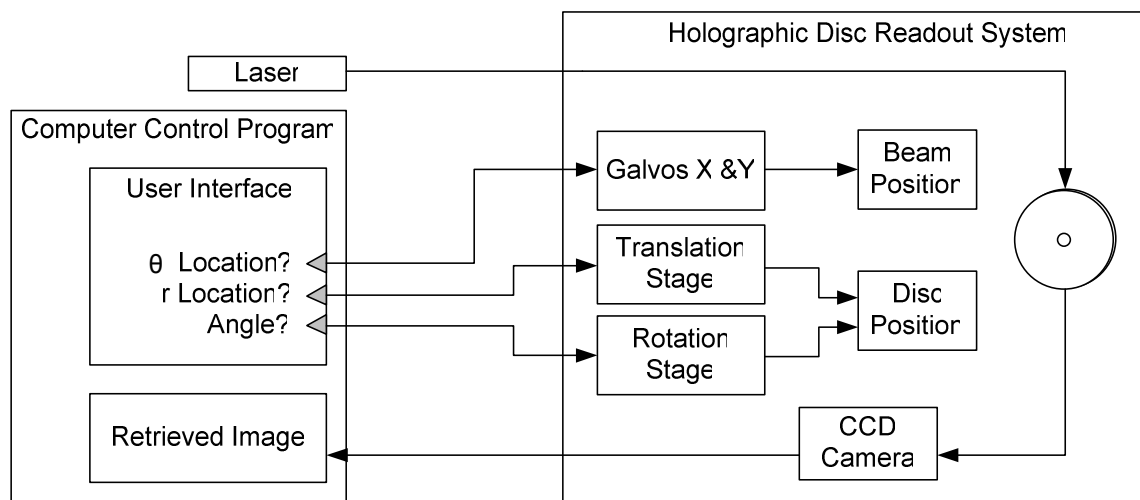


**Figure 6-2: Block Diagram of the Read Architecture**

The memory may be operated in random-access mode, where the user selects any memory location to read, or it may be operated in a sequential mode, where all memory locations are read out sequentially. The latter mode is useful for the holographic smart eye system, described in Chapter 8.

### **6.3 LAPT Disc-based Holographic Memory System**

#### **6.3.1 Overview**

The disc-based holographic memory system was designed to provide as much flexibility as possible. The system can use a projector-based digital light projection (DLP), an SLM, or a ferroelectric liquid crystal-based SLM (FLC-SLM). The HMU is mounted on a motorized rotation stage, which is then mounted on a motorized linear translation stage. Additional micrometer-driven stages between the components allow the precise positioning of the holographic material at the recording plane (the plane where the image and reference beams overlap). The rotation stage allows shift-multiplexing to be used, while a pair of galvanometer mirrors placed in the reference beam path allows for angle-multiplexing. The HMU mount

allows for one of three different types of materials to be used: an Aprilis holographic media disk, a Memplex holographic coupon, and a LAPT-manufactured square holographic plate. The system has so far been successfully tested with all three material types, both SLM types, and angle-multiplexing.

The implementation of the LAPT disc-based holographic memory system is shown in Figure 6-3. The media in use are all sensitive to blue-green light, so the chosen light source is a frequency-doubled Nd:YAG laser at 532 nm with a linearly-polarized output. The laser beam is sent through a spatial filter to expand the beam to 2" and to create a uniform beam profile. A polarizing beamsplitter cube is used to divide the beam into a reference beam and an image beam. This is done so that a half-wave plate can be used to control the amount of light that is directed to either path, which is necessary to control the ratio of power between the reference and image beams. To ensure that both beams are of the same polarization at the holographic disc, another half-wave plate is used.

The reference beam is bounced off of two galvanometric (galvo) mirrors. The two galvos are placed in an equilateral triangle with the recording spot at the holographic disc. This is done so that when one mirror is rotated, the other can also be rotated to change the angle of incidence at the recording spot without displacing the reference beam from that spot. This is the principle of angle-multiplexing. If shift-multiplexing is desired, the galvo mirrors can be held in place.

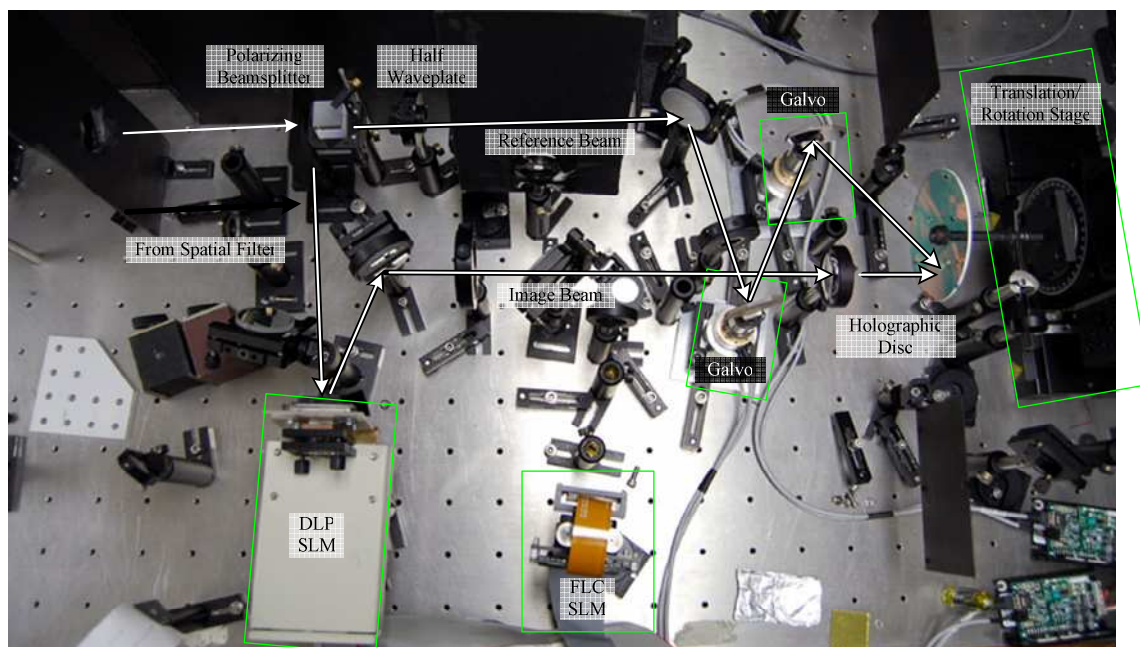


**Figure 6-3: Disc-based Holographic Memory**

The image beam is sent to an SLM. Pictured in Figure 6-3 are both the DLP projector SLM and the Boulder Nonlinear FLC SLM. Both SLM's are reflection type and a series of flip mirrors can be used to select one or the other. After reflecting from the SLM carrying the image, the beam is sent through a  $4f$  optical imaging system to the recording spot. The  $4f$  system is designed to reduce the image size by half. After the holographic disc, another set of  $4f$  optics is designed to bring the read out image to a CCD camera.

The galvos, SLM, translation/rotation stages, and the CCD camera are all controlled through a LABVIEW-enabled PC. A shutter for the laser is also controlled by the PC. LABVIEW programs were written to control writing, readout, and correlation search of the holographic disc.

### 6.3.2 Beam Conditioning

The laser used for this system is a Coherent Verdi V5 5.5 W frequency-doubled ND:YAG laser. It is linearly polarized vertically with respect to the optical table, which is s-polarization in the plane of rotation of the optics. The beam at the laser output is only 2.25 mm in diameter, so before it can be used with either SLM or as a reference beam, it must be expanded so that it covers the entire frame of either SLM. The beam is expanded using a microscope objective. A pinhole aperture is placed at the focal spot to perform spatial filtering of the beam to remove any artifacts and leave an undistorted beam. The spatial filter is from Edmund Optics and is shown in Figure 6-4.

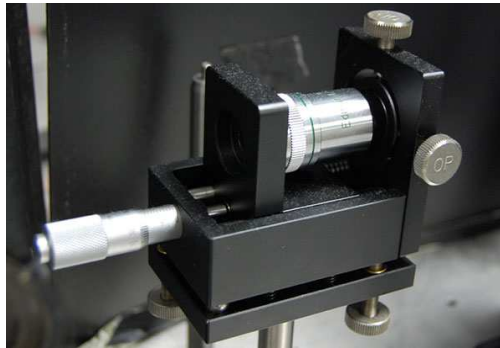


**Figure 6-4: Spatial Filter**

A 2" lens is used to collimate the expanded beam after it has passed the spatial filter. 1" optics are used throughout the rest of the architecture, but using a 2" lens to collimate the beam allows a more uniform beam distribution and allows us to use just the center of the collimated beam, avoiding the diffraction effects from the edge of the collimating lens. The spatial filter must be checked for alignment before proceeding each time, because even a small shift in the beam's position as it enters the microscope objective can lead to a large reduction in output power and beam quality.

After passing through the spatial filter, the beam passes a 1" square mask, and a polarizing beamsplitter cube splits the beam into reference and image beams. The mask shields unwanted stray illumination from reaching the rest of the optical system. A half-wave plate placed in the optical path prior to the polarizing beamsplitter allows the rotation of the polarization of the beam, which in turn determines the percentage of light that is passed and reflected from the splitter.



**Figure 6-5: PBS cube, Mask, and Half-wave Plate**

The polarizing beamsplitter cube reflects s-polarized light and transmits p-polarized light. In other words, it breaks the linearly polarized light up into its component vectors with respect to the optical axis of the beamsplitter. So that the polarization of the reference and image beam is the same, a half-wave plate is also used after the beamsplitter, in the path of the transmitted beam, so that both beams are s-polarized. The mask, polarizing beamsplitter cube, and half-wave plate are shown in Figure 6-5.

### **6.3.3 Image Beam: Spatial Light Modulator**

After the light is split into image and reference beams, the image beam falls on one of two possible spatial light modulators. The SLM that is used is many of the experiments

described here is a modified DLP projector. DLP technology uses a Digital Micromirror Device (DMD) to create an image. Each pixel is a micromirror mounted on a silicon backplane. Each pixel can be set to a voltage that causes the mirror to rotate towards or away from the exit aperture, thus either showing a light pixel or a dark pixel in varying degrees.

The DLP SLM was created by removing the DMD chip and substrate from the body of a projector, and mounting them on a suitable support. Instead of the light bulb from the projector, the laser light is reflected off the DMD chip and the reflected light carries the image. Just like a normal projector, it displays whatever is connected to it. The SLM is connected to a PC, and to display an image on it, the desired image is simply shown on the PC screen. The DLP SLM is shown in Figure 6-6.

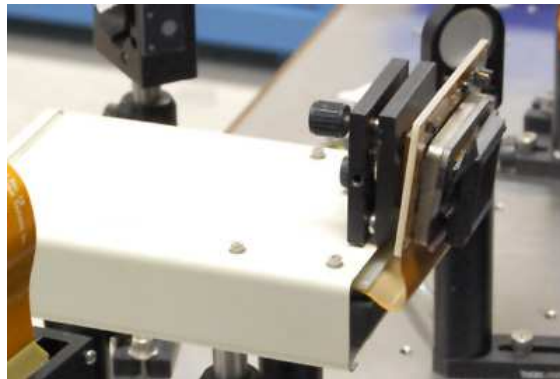


**Figure 6-6: DLP SLM**

This SLM works as a reflection device. A small angle of incidence is necessary, and apertures are necessary to block multiple orders. Computer control of this SLM is performed by using a section of custom C code in LabVIEW to display the desired image full-screen on a secondary display. The computer system has a video card that allows multiple displays, so while the primary display shows the control program, the secondary display is connected to the projector body and can display the image data. The display has 800x600 pixels and can display 256 values of grayscale.

The holographic memory can also be used with a Boulder Nonlinear FLC SLM. This SLM is shown in Figure 6-7. It is a 512x512 pixel device that can display in 256 values of grayscale as well. It uses a ferroelectric liquid crystal screen as a voltage-variable polarization rotator. Because of this, it also requires some type of polarizer to display proper images.



**Figure 6-7: FLC SLM**

The FLC SLM operates in the following manner. The FLC display acts like a half-wave plate that can rotate its fast axis. In other words, it is a variable polarization rotator. Any given pixel in the display will rotate the polarization of the incident light in proportional with the applied voltage, with a maximum rotation of  $+\pi/8$  or  $-\pi/8$ . A half-wave plate is used to orient the incoming linearly polarized E-field at  $-\pi/8$  with respect to the normal fast axis position. If the fast axis is shifted  $-\pi/8$ , the fast axis will be in line with the E-field and a uniform half-wave phase modulation will be applied to the E-field, and no change will be observed through a polarizer. However, if the fast axis is rotated  $+\pi/8$  instead, it will now be aligned with the y-component of the E-field and perpendicular to the x-component. This will cause the y-component to see a phase shift while the x-component is unchanged, leading to a rotation of 90 degrees of the polarization of the reflected light. This is shown in Figure 6-8.

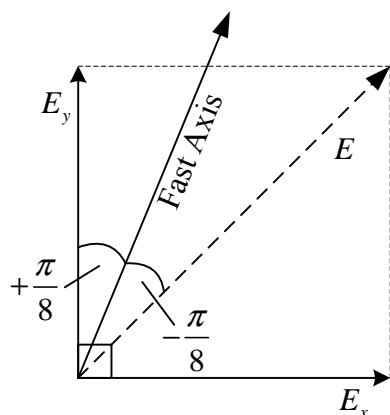


**Figure 6-8: FLC SLM Polarization Rotation**

When viewed through a polarizer, pixels that have had their polarization rotated can be discriminated from those that have not. A voltage that causes a rotation between plus and minus  $\pi/8$  will lead to grayscale values. The architecture for the FLC SLM is shown in Figure 6-9.

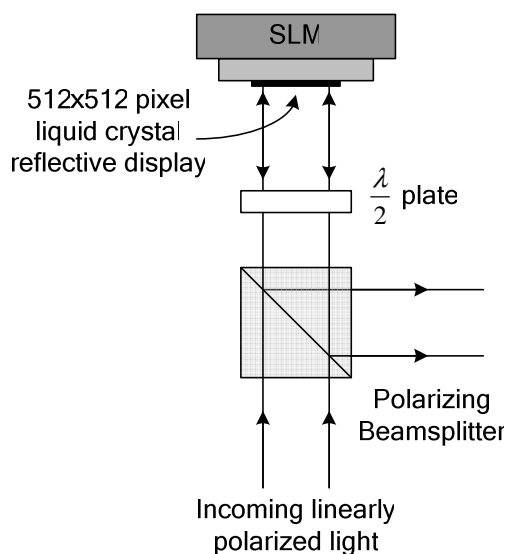


**Figure 6-9: FLC SLM Architecture**

The FLC SLM has its own control program and control board inside the PC. The control board is a PCI board that also has two signal lines for controlling an external shutter. Because the device is an FLC type SLM, it must be DC-balanced. A negative image must follow each

positive image in order to avoid any net voltage, which could damage the display. The PCI board control lines output a square-wave signal corresponding to the positive and negative image timing, so that a shutter may be used to allow only one or the other. The control lines are connected to the data acquisition board of the PC, and LabVIEW is used to control the timing of the shutter, opening the shutter for each positive image and closing it during the negative image. This way the holographic material sees only the positive image.

### 6.3.4 Image Relay Optics

Both SLM's have displays that are made of discrete elements, or pixels. Because these pixels have a finite size with some small space in between them, they act as a diffraction grating when light is incident upon them. They are designed to reflect most of their light into the 1<sup>st</sup> reflected order; however, the other orders are still present along with the main order as the image propagates away from the screen. These orders may be filtered out, but they carry a significant portion of energy with them (~%20 for the BNS SLM). In addition, the small pixel size means that diffraction affects the image quickly. To solve both of these problems, a set of image relay optics are used to transport the image beam from the SLM face to the holographic disc. This is a common optical system called a  $4f$  imaging system (see Appendix 10.3).

In fact, at any point where an image is being transferred optically from one location to another, we make use of this image relay system to prevent diffraction effects from blurring and distorting the image. Such points include from the SLM to the holographic disc during writing, from the holographic disc to the CCD camera during readout, from the holographic disc to the optical correlator as part of the holographic smart eye device, and from the SLM to the optical correlator in the smart eye device.

The  $4f$  system is also useful because it can reduce the size of an image without introducing distortion. The system is shown in Figure 6-10.

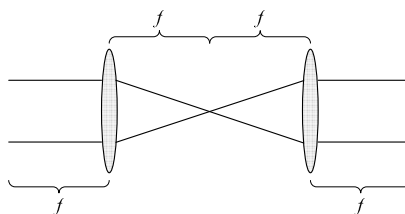


**Figure 6-10: Basic  $4f$  System**

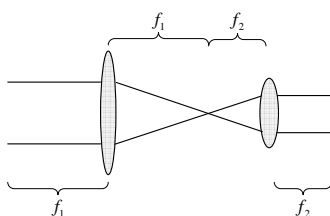


**Figure 6-11:  $4f$  System to reduce/expand image size**

Figure 6-11 shows the configuration for reducing or expanding the beam. The  $4f$  imaging system consists of two lenses spaced apart by the distance of their focal lengths. The image and object are also a focal length away, so the total imaging distance is four focal lengths. If the focal lengths differ, as in Figure 6-11, then the image is magnified or de-magnified by the ratio of the focal lengths.

### 6.3.5 Reference Beam Optics

As described in Section 6.3.2, the polarizing beamsplitter cube divides the conditioned beam into reference and image beams. The reference beam is directed to the holographic disc by a set of galvanometer mirrors (galvos). The galvo mirrors are from GSI Lumonics. They can be controlled through a LabVIEW interface. One of the two mirrors is shown in Figure 6-12.



**Figure 6-12: Galvo mirror**

The two galvos are arranged in a roughly equilateral triangle with the recording spot on the holographic disc. Changing the first galvo by an angle  $\theta$  and the second by an angle  $2\theta$  will result in an angle change at the recording spot without shifting the recording spot. This arrangement is shown in Figure 6-13.

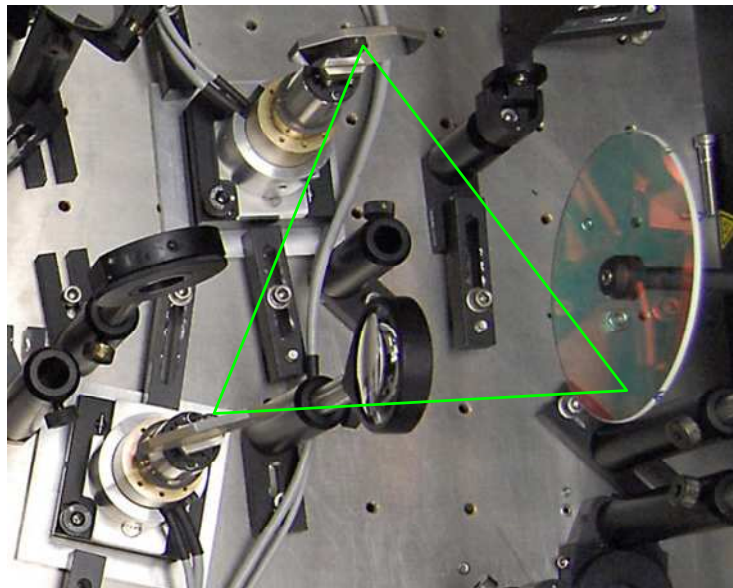


**Figure 6-13: Equilateral Triangle Arrangement of the Galvo Mirrors**

The galvos have 32768 different addressable positions and a total angular rotation of 20 degrees. The galvos are accurate to 0.01%, which leads to a minimum resolvable angle of about 0.1 mrad. For a 1 mm thick holographic material, the Bragg angular selectivity for 30 degrees angle of incidence is about 0.5 mrad.

### 6.3.6 Exposure Schedule

As discussed in Chapter 2, the response of a photosensitive medium to light is a nonlinear-shaped curve. At first, the material response is roughly linear while the light is absorbed by the photosensitive agents. As the amount of photosensitive agent decreases, the amount of absorbed light also decreases until there is none left and the material becomes transparent. This is shown in Figure 6-14, which is a plot of the cumulative grating strength (sum of all grating strengths) as a function of the cumulative exposure (sum of grating exposures).

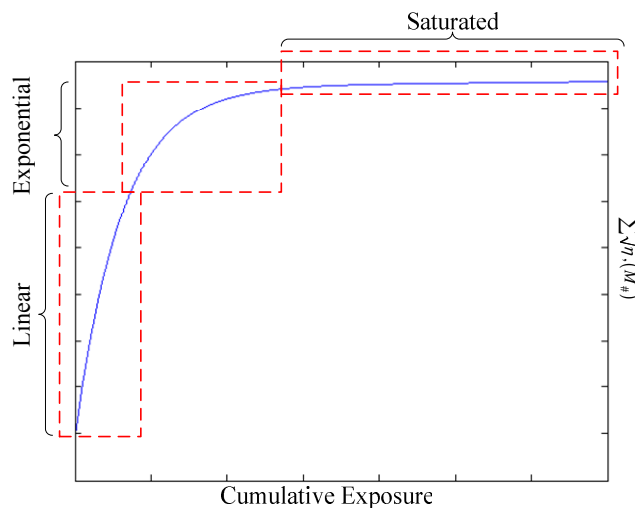


**Figure 6-14: Typical Material Response Curve**

For co-locational holograms, the dynamic range of the material must be divided up amongst all the holograms. If the holograms are all written with equal exposure energy, the amount of

dynamic range given to each hologram will vary throughout the recording process, and the diffraction efficiency of the holograms will differ greatly. This is shown in Figure 6-15 using the material response curve for the Aprilis CROP material. The vertical dashed lines represent the exposure value for each hologram. Each hologram is given an equal exposure of  $50 \text{ mJ/cm}^2$ . The horizontal dotted lines intersect the exposure values at the material response curve and show the amount of dynamic range allotted to each hologram. For example, the first hologram is allotted just over 4 units of grating strength, while the second receives only 2, and the third uses less than 1. The equal exposure value of  $50 \text{ mJ/cm}^2$  is chosen to exaggerate the effect of this problem, but it would be apparent even if the equal exposure value was chosen to be smaller.

The solution to this problem is to implement a recording schedule such that each hologram receives an equal portion of the dynamic range (grating strength). This is shown using the same Aprilis material response curve in Figure 6-16. Now the usable amount of the dynamic range is decided, and then this amount is divided by the number of holograms to be written. In this example, seven holograms are multiplexed in one location. The usable dynamic range is determined to be 7. Although the material curve shows that the cumulative grating strength runs all the way to 7.5 or so, the amount of energy required to achieve the extra dynamic range is deemed unnecessary. A series of long exposures could be used to take advantage of the entire dynamic range, but this would have two negative effects. First, the writing time for each spatial location would increase drastically, as would the writing time of an entire disc. Second, because it is impossible to keep adjacent spatial locations completely protected from stray light during a disc recording, these long exposures would pre-exposure adjacent areas, de-sensitizing them.

We divide the dynamic range equally among the holograms: the horizontal lines are equally spaced to divide the dynamic range among the gratings, and then the vertical lines are

drawn to show the different exposure values. The figure shows that the initial exposures will be shorter than the later exposures to compensate for the nonlinear response of the material curve.

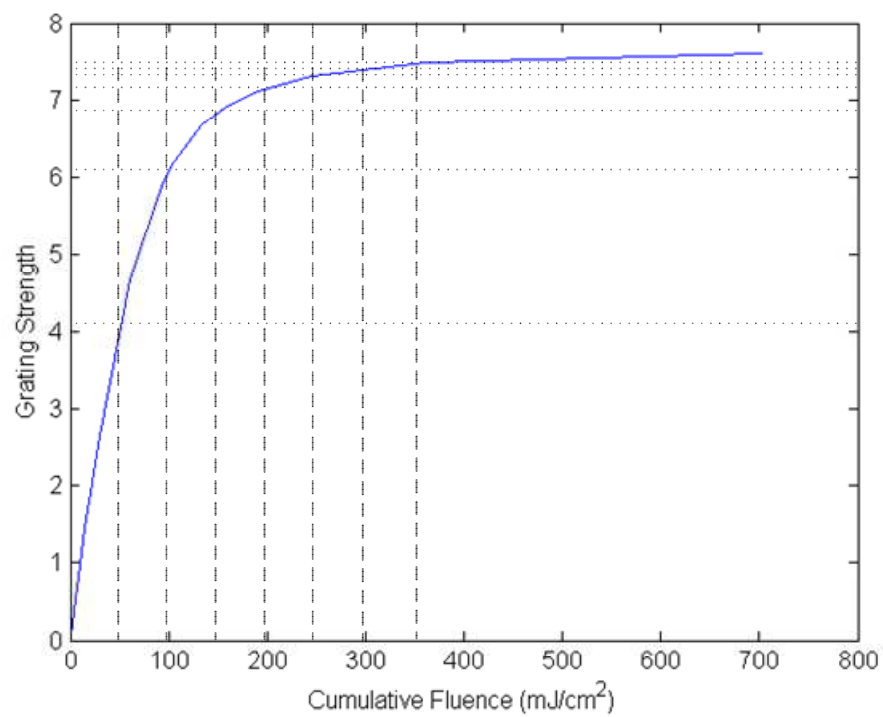


**Figure 6-15: Equal exposure holograms**

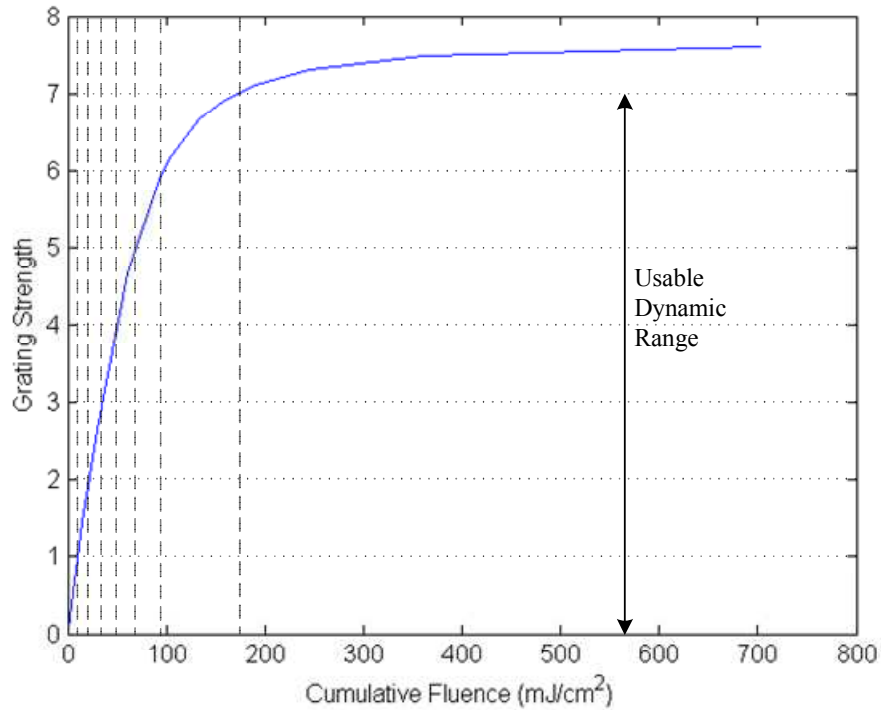


**Figure 6-16: Equal grating strength holograms**

The recording schedule can be calculated graphically as shown above or analytically. If the cumulative grating strength (M/#) of the material is  $A_{sat}$ , and  $A(E)$  is the function describing the curve in Figure 6-16, then each hologram should receive  $\frac{A_{sat}}{M}$ , where  $M$  is the total number of holograms to be multiplexed. Then it is evident that:

$$\frac{A_{sat}}{M} = A(E_n) - A(E_{n-1}) \quad (6.1)$$

$$A(E_n) = A(E_{n-1}) + \frac{\partial A(E_{n-1})}{\partial E} E_n$$

and so:

$$\frac{A_{sat}}{M} = \frac{\partial A}{\partial E} \Big|_{E=\sum_{i=1}^{n-1} E_i} E_n \quad (6.2)$$

Equation (6.2) can be re-written in terms of the exposure time  $t_n$ :

$$t_n = \frac{A_{sat}}{I * M * \left. \frac{\partial A}{\partial E} \right|_{E=\sum_{i=1}^{n-1} E_i}} \quad (6.3)$$

where  $I$  is the total intensity of the writing beams.

Equation (6.3) provides a recording schedule for a photosensitive material. However, this method ignores the fact that in some recording materials, subsequent exposures can partially erase previous exposures. To take this effect into account, the procedure above (either graphical or analytical) can be iterated, using the new cumulative grating strength versus cumulative exposure curve each time. For writing the holograms in the Aprilis discs, a recording schedule was provided by Aprilis.

### 6.3.7 Holographic Disc Material

The holographic disc-based memory was designed to accommodate any holographic memory that could be formed into or mounted onto a CD-sized disc (120 mm diameter with a 1 cm mounting hole). The system was tested with two different materials: the Aprilis Cationic Ring-Induced Photopolymer (CROP) material and the Laser Photonic Technologies (LPT) photochromic polymer, Memplex™.

The Memplex photochromic polymer is a dye-doped poly(methyl methacrylate) material. It is formulated as a 1.5" by 1.5" square coupon that is 2 mm thick. The thickness makes it an excellent candidate for high-density storage, although the sensitivity of the material is quite low. The Memplex material is mounted in an aluminum frame for mounting as a disc. The material and mount are shown in Figure 6-17.

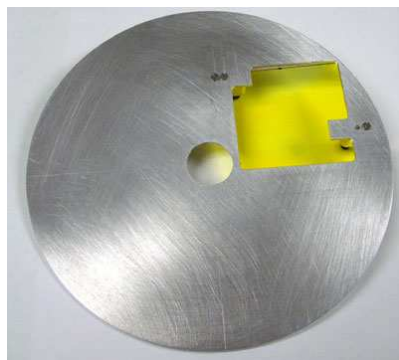


**Figure 6-17: Memplex™ in Disc Mount**

The Aprilis material is a 400 micron thick photopolymer pressed between two anti-reflection coated glass substrates. The material has a sensitivity of 1.5 cm/mJ and an  $M_{\#}$  of 6.8.



**Figure 6-18: Aprilis CROP Media Disc**

The Aprilis disc is shown in Figure 6-18. The high sensitivity of the Aprilis material required a series of baffles and masks to ensure that no stray laser light would hit the disc during the writing. Further improvement could be gained by utilizing optics that are anti-reflection coated for 532 nm.

### **6.3.8 Writing Procedure**

The writing of the holographic discs is controlled through a LabVIEW program running on a standard personal computer. There is a data acquisition and control card that can control multiple digital outputs and read multiple analog and digital inputs. The LabVIEW control

program controls the shutter for exposure control, the SLM display, the galvo mirrors for angle-multiplexing, and the translation and rotation stages. The images to be written are collected ahead of time and an exposure schedule is calculated as shown in Section 6.3.6. Offsets for the rotation and translation stages as well as the galvo can be entered to precisely align the recording. This is done in a test recording with a dummy media disc prior to the actual recording. The intensity of each beam is measured using an iris diaphragm of a set diameter with the detector perpendicular to the beam. For measuring the SLM beam, a blank white image is used to measure the maximum intensity in the SLM beam.

The disc is mounted to the rotation stage using a custom-built shaft. Once mounted, a series of baffles and masks are positioned to shield the disc from stray light. After this step, the optical table is allowed to settle. It is mounted on vibration isolation legs, and the air pump is switched off to prevent it from operating during the write. The holographic write program is shown in Figure 6-19.

**Figure 6-19: Holographic Disc Write Program**

Once the writing process begins, it is fully automated. The program automatically looks for images and exposure schedules in a pre-set directory structure. Each rotation angle is indexed from 0-31, and each rotation angle directory contains a sub-directory for each spatial location. An example location for a set of images would be C:\source\0\3\. This folder would reference the third spatial location in the 0 angle directory. Inside this directory would be a list of bitmap images, also indexed from 0. In addition, an exposure schedule file is contained in the directory. This allows each set of images to use a different exposure schedule if desired.

The writing process can be paused and restarted, or completed in increments. Once the disc is finished, it can be left on the mount or removed. A helium neon laser aimed at the edge of the disc allows re-alignment.

### 6.3.9 Results

There were several problems with the first Aprilis disc that was written. The mask that was in place in front of the disc did not adequately constrain the horizontal width of the beam. Therefore, portions of the adjacent spatial locations were pre-exposed, leaving images that were unevenly exposed on the sides. In addition, in the chosen geometry the reference beam clipped part of the rotation mount during some angles and scattered stray light into the disc. These problems were corrected by adjusting both the mask and the writing geometry so that the reference beam did not clip on any part of the mount and was the proper size. Because the reference beam angle changes with respect to the disc during angle multiplexing, so does its horizontal size. The maximum angle has the maximum corresponding width, and this width was used to calculate the proper spacing between spatial locations.



**Figure 6-20: Image from the first disc**

Finally, a miscalculation in the actual angles of the reference beam led to an incorrect angular bandwidth calculation. Images exhibited crosstalk noise as shown in Figure 6-20. Beyond correcting these problems, the laser power was increased to reduce the write time of the disc.

In the second disc, a series of different types of images were stored and retrieved. These are shown in Figure 6-21. They show the range of images that were stored. Binary data, silhouettes, aerial photographs of buildings and landscapes, and resolution charts were all stored in the second disc. Comparing Figure 6-21 and Figure 6-20, we can see that most of the crosstalk noise has been eliminated from the images.



Figure 6-21: Data Retrieved from the second Aprilis Disc

## 6.4 Conclusion and Next Steps

The disc-based holographic data storage system described here was designed and built as a first generation system. Further improvement to the system to increase read and write speed as

well as image quality can be achieved by a combination of additional hardware and software.

Here, I describe some of the limitations of the current system along with possible solutions.

In general, with highly-sensitive media such as the Aprilis CROP media, stray reflection can reduce the available  $M_{\#}$  of the material in addition to causing readout noise. Anti-reflection coatings for all optics would be a significant step in reducing these reflections. Most of the optics used in this system have a broadband AR coating, which reduces reflections to less than 1%. A V-coat designed specifically for 532 nm could reduce the reflection to less than 0.05%, a 20x improvement.

For greater image density and a faster write time, the preferred SLM is the Boulder Nonlinear SLM. This SLM has a smaller pixel pitch as well as the ability to display images at up to 1 KHz. Currently the SLM is not controlled by the LabVIEW software. The BNS software is used to load the desired image sequence, and the PCI card control lines are used to time the shutter and galvo movement so that the holographic material is only exposed to the positive image. This has several drawbacks. The most severe is that no recording schedule can be used because this feature is not available in the BNS software. This becomes an issue when many images are recorded, which is the case in many desirable applications. In addition, faster recording times can be gained when using this SLM. The SLM is capable of a 1 KHz refresh rate, which would lead to a 500 Hz (because of the positive-negative image) writing operation. However, because the control lines must exit the PCI card and be re-acquired through the DAQ card, the software cannot accurately control the shutter and galvo timing this precisely. In the future, obtaining the source code from BNS would allow a custom C module to be written and used in LabVIEW to access the timings directly. This would allow for the implementation of both faster writing and an exposure schedule using the BNS SLM.

Currently the lenses used in the disc-based holographic memory are all spherical singlet lenses, usually in a  $4f$  configuration. No aberration correction has been attempted. In order to provide a higher quality beam, aberration control should be implemented using pairs of positive and negative lens for beam expanders, and achromat doublet lenses for all  $4f$  imaging systems. Precision achromats are corrected for nearly zero spherical aberration and coma, and, although designed to offer good performance at a range of wavelengths, work just as well at a single wavelength. In addition, a pair of achromat doublets with a low  $F/\#$  could be used to replace the pair of galvo mirrors with just one galvo mirror. This could allow a larger total angle range for angle multiplexing.

These improvements along with adjustments to the code should allow a much higher-speed operation of the holographic memory hardware to further test the real-time correlator until the SPHRAM is ready for use.

## 7 Real-time Vanderlugt Correlator

### 7.1 Introduction

The idea of correlation, or of a correlator, is not restricted to holography or even optics. Correlation is a mathematical operation that can be defined as:

$$\int_{-\infty}^{\infty} f(x)g(x-y)dx \quad (7.1)$$

The correlation operation determines how similar the functions  $f$  and  $g$  are to each other. The autocorrelation is the correlation of a function with itself, and has some usefulness that I will describe later. In any type of random search, where one is trying to match a given set of data with something that may or may not be in a database, the correlation function can be used. For instance, if one has an image (really just a two dimensional bit pattern), the correlation operation can be used with that image and every image inside a database to try to find a match. If there is a similar or exact match, the result of the correlation function is 1 or close to 1 (assuming normalization). Otherwise the correlation operation will return a value less than one, depending upon the similarity between the images.

This type of correlation operation is extremely useful in applications such as face recognition, fingerprint identification, target identification and tracking, and visual navigation and machine vision. Current techniques for correlation rely on electronic microchips to process the information serially and compare the images bit by bit. On the other hand, an optical correlator offers the ability to perform the correlation in parallel and can be constructed in a very simple and straightforward manner. This type of optical correlator was first described by Vanderlugt in 1963, and is known appropriately as the Vanderlugt correlator.<sup>139</sup> A similar

method was described by Weaver and Goodman in 1966 and is called the joint transform correlator.<sup>140</sup> These two configurations for optical correlators remain the most popular and used today.<sup>141-154</sup>

## 7.2 Vanderlugt Correlator

The traditional Vanderlugt correlator proceeds in two steps. In Step 1, a filter is created by recording the interference pattern formed between a reference beam, usually a plane wave, and the Fourier transform of a signal beam, the query image. These two steps are shown in Figure 7-1. The Fourier transform of the signal beam is obtained using a lens (see Appendix 10.2).

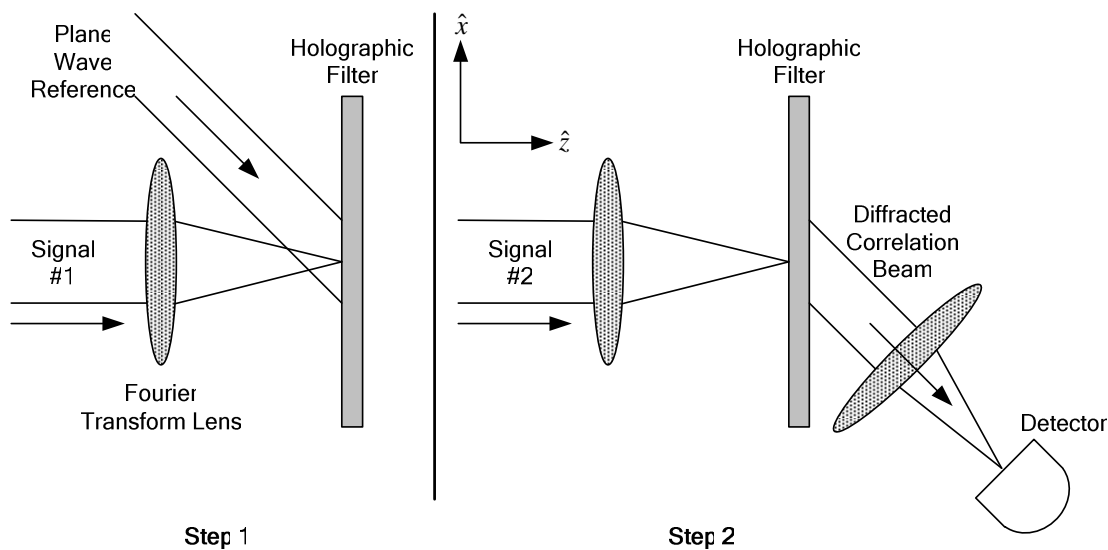


**Figure 7-1: Vanderlugt Correlation Steps**

Mathematically, we represent the reference beam as a plane wave traveling at an angle  $\theta$ :

$$U_{ref} = e^{-jk \sin(\theta)x} \quad (7.2)$$

where  $k$  is the wavenumber ( $2\pi/\lambda$ ). This can be re-written in the form  $U_{ref} = \exp(-j2\pi\alpha x)$

where  $\alpha = \sin(\theta)/\lambda$ . The signal beam image is represented by  $h(x, y)$  and is presumed to be

traveling normal to the holographic filter medium. The Fourier transform of  $h$  as obtained by the lens is  $H(x, y)$ .

At the holographic filter in Step 1, the interference of  $U_{ref}$  and  $H$  is formed. The material records the intensity of the interference pattern, and the transmittance of the filter becomes:

$$\begin{aligned} t_{filter} &= |U_{ref} + H(x, y)|^2 \\ t_{filter} &= |e^{-jk \sin(\theta)x} + H(x, y)|^2 \\ t_{filter} &= 1 + |H|^2 + e^{-jk \sin(\theta)x} H^*(x, y) + e^{jk \sin(\theta)x} H(x, y) \end{aligned} \quad (7.3)$$

In the second stage of the Vanderlugt correlation process (Step 2 in Figure 7-1), the filter created in Step 1 is read using the Fourier transform of a second signal. If the second signal is represented as  $g$  and its transform as  $G$ , then after the filter the field is:

$$\begin{aligned} U_{after} &= \left[ 1 + |H|^2 + e^{-jk \sin(\theta)x} H^* + e^{jk \sin(\theta)x} H \right] G \\ U_{after} &= G + G |H|^2 + e^{-jk \sin(\theta)x} H^* G + e^{jk \sin(\theta)x} HG \end{aligned} \quad (7.4)$$

The final lens in the correlator just before the detector performs a final Fourier transform on the field in equation (7.4). Ignoring the two terms that appear at 0 degrees, the field that is seen at the detector is:

$$U_{after} = F.T. \{ e^{-jk \sin(\theta)x} H^* G \} + F.T. \{ e^{jk \sin(\theta)x} HG \} \quad (7.5)$$

Using the convolution theorem transforms along with the Fourier transform pair  $F.T. \{ \delta(f - a/2) \} = e^{i\pi ax}$ , we see that the two terms in equation (7.5) are:

$$\begin{aligned} h(x, y) \otimes g(x, y) \otimes \delta(x + \alpha, y) \\ h^*(-x, -y) \otimes g(x, y) \otimes \delta(x - \alpha, y) \end{aligned} \quad (7.6)$$

The first term is the convolution of  $h$  and  $g$ , and the second term is the correlation of  $h$  and  $g$ .

The two terms are separated from the 0 degree terms in the plane of the detector by  $\alpha$ . The detector can be moved and fitted with an aperture so that only the correlation term is seen.

The Vanderlugt correlator as described has the potential to be useful as the key element of an optical database search, but the need to create a filter for each new query severely limits its application. However, if a material can be found where the filter can be refreshed dynamically, then after one query is finished, the filter can be erased, a new one created, and the process started anew.

In the Joint-Transform correlator, the Fourier transforms of both functions to be correlated are used to create a holographic filter. A plane wave beam is then used to record this filter and the diffracted beam is again proportional to the correlation. This architecture is shown in Figure 7-2.

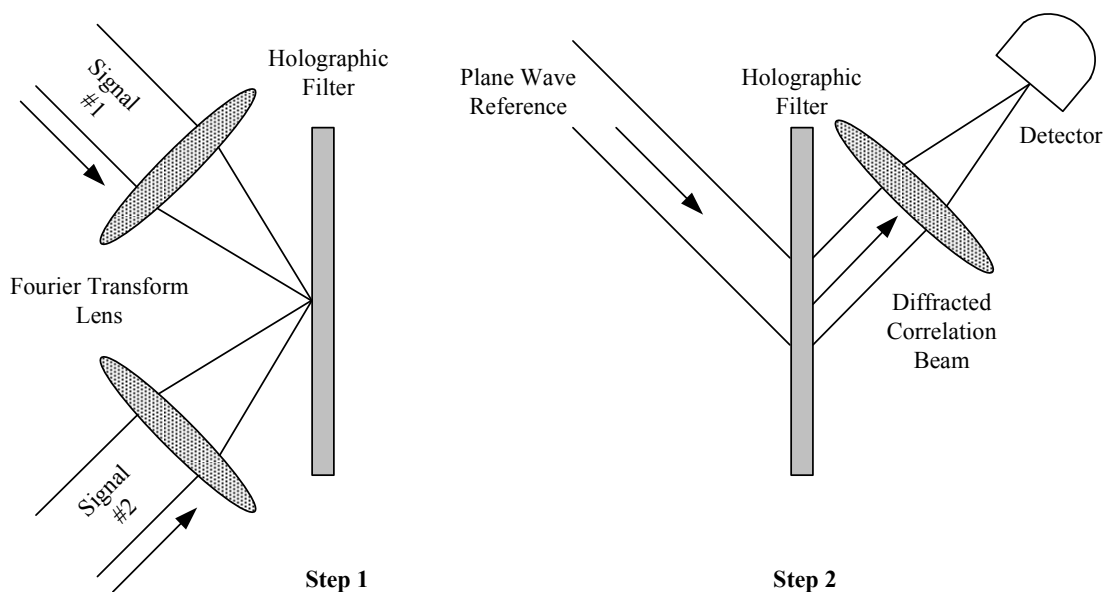


**Figure 7-2: Joint Transform Correlator**

In both cases, a lens is used to transform the images into their Fourier transforms. Although these figures show the architecture in two dimensions, the signal beams and reference beams extend in the third dimension. That is, each signal beam is a 2D “page” of data. Thus, the optical correlation operation processes the entire page of data at once. For a typical data page of 1024x1024 bits, this is equivalent to about 1 MB of data that can be correlated in parallel, in the time it takes light to traverse the system. For the type of optical correlator described above, either the Vanderlugt or Joint-Transform correlator can be used with no significant advantage to one or the other. However, in real-time correlation, the Vanderlugt architecture has a benefit, as discussed below.

### **7.3 Real-time Correlation**

In a real-time holographic material, the nonlinear response of the medium is fast enough to respond to the intensity of the fields present within milliseconds. The nonlinear response of the material creates an index of refraction modulation which creates a temporary hologram. While the beams are present, the grating is strong. Soon after the beams are removed the hologram decays. The response time and decay time are characteristic of the specific material being used.

For most materials, the response time is slow. Photorefractive crystals typically have response times of the order of seconds, while materials such as the NDT photorefractive polymer can have a response time of up to 15-30 ms. During real-time correlation, all four beams are present (two beams writing the filter/grating, one read beam, and one diffracted beam). If we choose to use the Joint-Transform correlator architecture as shown in Figure 7-2, each time the query image is changed, a new grating is written in the material. This would lead to

unacceptably slow performance. If however, we choose the Vanderlugt configuration, the query image can be used with the reference beam to create a holographic filter (in the form of a real-time grating) that can then be used to search an entire database. Once every image in the database has been correlated with the query image, the query can be changed and the search started anew. In this way, the response time of the material only plays a part in determining the speed of switching query images, not the speed of the database search.

### 7.3.1 Vanderlugt Configuration

Figure 7-3 shows the architecture for the real-time Vanderlugt correlator. The plane wave reference and signal beam #1 are both polarized in the same direction, ideally polarized perpendicular to the plane defined by the angle between them. The signal beam #2 is polarized in the plane of the figure, orthogonal to the reference and first signal beams. The material responds to the intensity of the interference pattern between the reference and signal beam #1 to create a grating. The signal beam #2 is incident in the opposite direction as signal beam #1 and diffracts off the grating along the same angle as the reference beam. A polarizing beamsplitter can be used to pick out the diffracted beam, which is orthogonal in polarization to the reference beam as well. The signal beams are chosen to be counter-propagating so that their respective Fourier transforms can be precisely aligned.

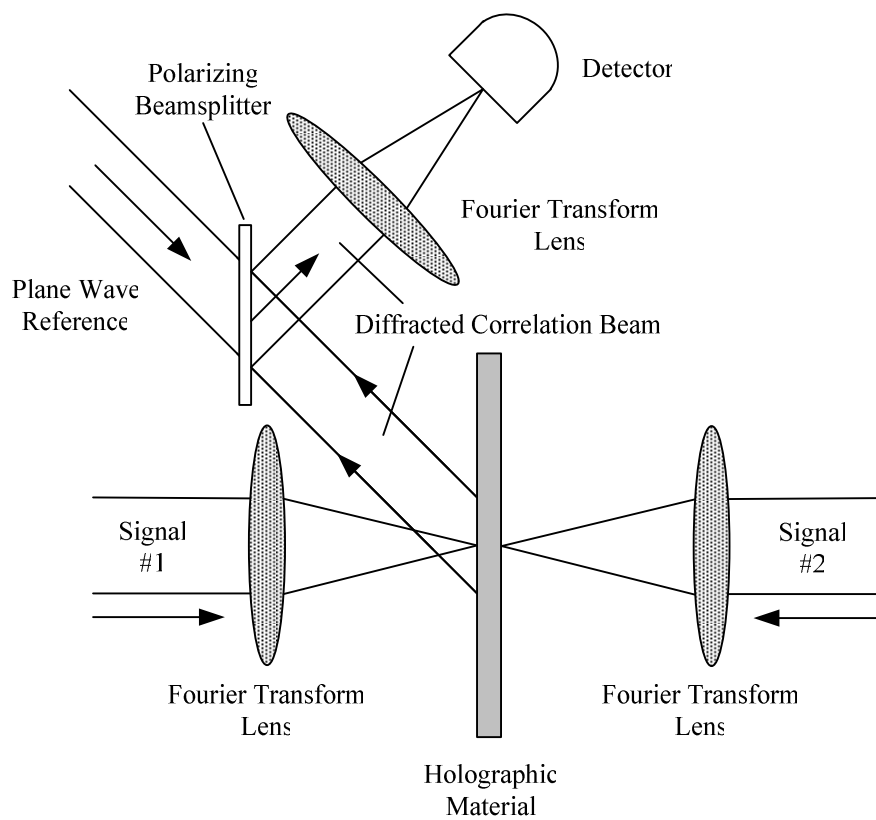


**Figure 7-3: Real-time Vanderlugt Correlator**

Once the grating is written by the reference beam and the signal beam #1, it need not be changed until a new query image is desired. For instance, once the grating is written, the reference and signal #1 beams can remain constant while the signal #2 beam is changed at high-speed and the correlation is measured. The correlation operation itself proceeds in the time it takes the light to traverse the grating and lens, so the operation is limited only by the detector and signal-to-noise ratio requirements.

### 7.3.2 Phase-conjugation Configuration

Figure 7-4 shows an alternative configuration that can be used to test the real-time material before its use in the correlator. This configuration is known as phase-conjugation. By counter-propagating the reference beam using a mirror, the diffracted beam becomes a phase-

conjugate of the original signal beam #1. The quarter-wave plate receives two passes and acts like a half-wave plate to rotate the polarization orthogonal to that of the writing beams. The phase-conjugate readout can be seen by examining the system as follows. The signal beam is denoted by  $h$  and the reference beam by  $r$ . The intensity pattern at the holographic material is then:

$$|r + H|^2 = |r|^2 + |H|^2 + r^* H + r H^* \quad (7.7)$$

where the capitol letter  $H$  is the Fourier transform of  $h$  as obtained by the lens. Counter-propagating the reference beam is akin to applying the field  $r^*$ :

$$r^* |r + H|^2 = r^* (|r|^2 + |H|^2) + (r^*)^2 H + |r|^2 H^* \quad (7.8)$$

The result is a term traveling along the  $r^*$  direction, a term along the  $(r^*)^2$  direction, and finally a term traveling along the  $H^*$  direction. This last term is the one of interest. Note that this is not a mirror image, but a phase-conjugate image that will arrive at the signal beam's origin with none of the defects of the optical system. Phase-conjugation is itself a subject of much research with many applications in signal processing and imaging, but here it is used to experimentally determine the parameters of the real-time material.

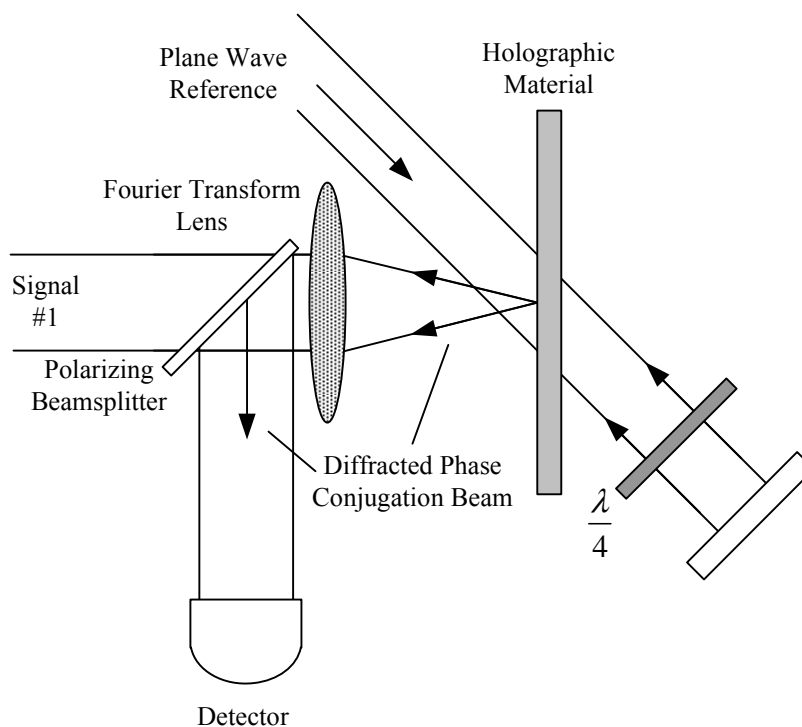


**Figure 7-4: Phase-conjugation**

### 7.3.3 Photorefractive Polymer

The photorefractive polymer used in these experiments was provided by the Nitto Denko Corporation. The samples are 30 microns thick and require a voltage of approximately 50-75 V per micron. The samples also require operating angles of more than 45 degrees to properly align the optical fields with the crystal axis of the material. The material is shown in Figure 7-5.

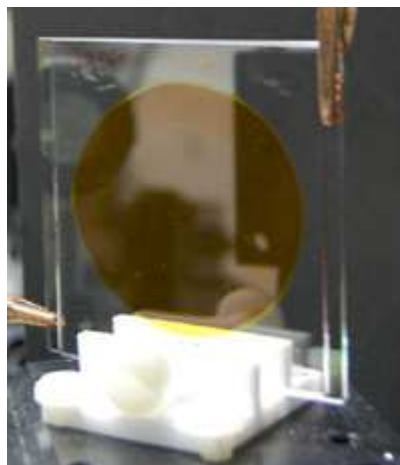


**Figure 7-5: NDT Photorefractive Polymer Material**

The material was tested in the phase-conjugate geometry to establish the proper intensity balance between the three beams. Because the ultimate goal was to establish a correlator with this material, the phase-conjugate geometry was used exactly as shown in Figure 7-4 with a Fourier transform lens in place to transform the signal beam. The Fourier transform of most images has a large DC component, which presents a challenge to a proper phase-conjugation because the dynamic range of most materials is not large enough to properly record both the DC component and the high-frequency components. For example, a typical image is shown in Figure 7-6.



**Figure 7-6: Image and Fourier Transform**

Note that the extremely bright center (DC) spot overshadows the higher-frequency components spread out along the axes. If the reference beam is set to an intensity that will record the DC

component well, the high frequency components will have a very low fringe visibility because the reference beam will be many times stronger. However, if the reference beam is set to an intensity that is proper for recording the higher-frequency components, the DC component will be overexposed and may become partially or fully burned out and blocked.

In fact, blocking the DC component is a desired effect in performing optical correlation and is typically referred to as “edge-enhancement”. Because many images have a strong DC component, they will all have a significant amount of diffraction from the grating produced by the DC component. Removing the DC component produces an edge-enhanced image and provides a much cleaner correlation. For example, consider the two images shown in Figure 7-7. The images are clearly different (rotated), but contain an equal DC component.



**Figure 7-7: Two Dissimilar Images**

We performed a self-correlation of the image on the left and compared it to a cross-correlation between the two images without using edge-enhancement. This is shown in Figure 7-8. On the left, the cross-correlation still produces a significant amount of light, and although the self-correlation on the right shows a strong center peak, the peak is broad. For translation-invariant correlation, the exact position of the output peak can be used to determine movement for target tracking, and the broadness of the correlation peak can obscure movement. Also, the amount of light present in the cross-correlation can interfere with thresholding algorithms.

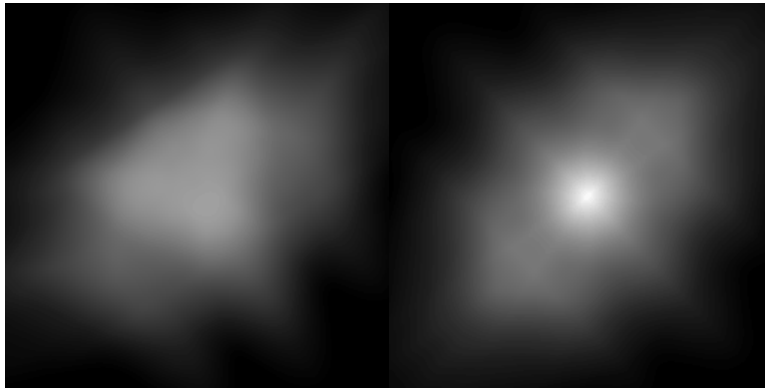


**Figure 7-8: Cross Correlation (left) and Self Correlation (right)**

After blocking the DC component, the edge-enhanced image will look similar to the image in Figure 7-9.

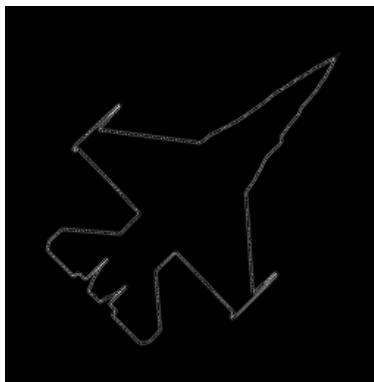


**Figure 7-9: Edge-enhanced Image**

The self- and cross-correlations between the images after edge-enhancement is shown in Figure 7-10. The cross-correlation is almost zero, and the self-correlation is a bright sharp peak in the center of the frame.



**Figure 7-10: Cross Correlation (left) and Self Correlation (right) with Edge-Enhancement**

In practice because the materials rarely have the dynamic range to record all the frequencies, it is a simple matter to set the reference beam to the level of the higher frequencies, which causes the DC component to be saturated and blocked, effectively providing an edge enhancement.

Experimentally, the phase-conjugation configuration was used to test the proper level of the reference beam for edge-enhancement.

### **7.3.4 Experimental Results**

The phase-conjugation and correlation configuration used in the experiment is shown in Figure 7-11 and Figure 7-12. The NDT material is mounted on a Teflon™ stage, which is then mounted on a conventional optical stage.

This is to electrically isolate it from the rest of the table. A voltage amplifier provides up to 3kV across the material to provide the proper bias voltage. The laser beam from a Coherent Verdi frequency-doubled ND:YAG (532 nm) laser is used as the coherent light source. The beam is expanded and divided into reference and signal beams. The signal beam reflects from an SLM to pick up the signal image. Two Pulnix CCD cameras are used to capture the phase-conjugate image and correlation image.

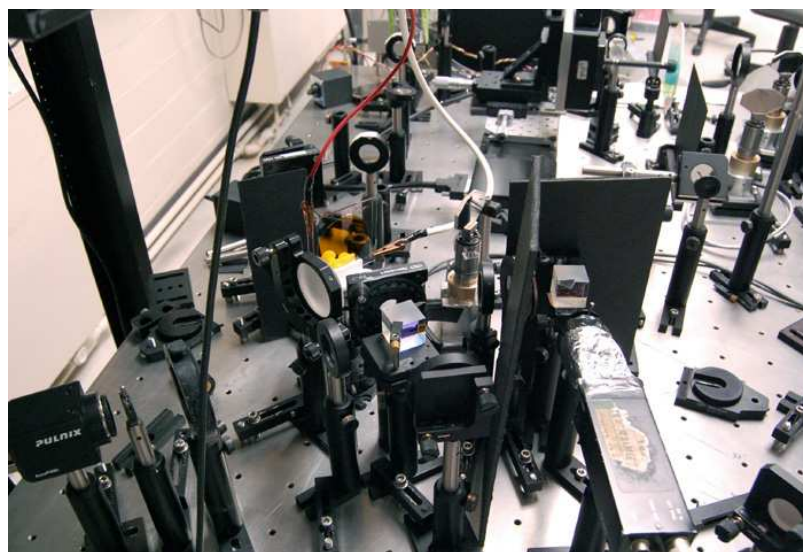


Figure 7-11: Phase-conjugation/Correlation Experiment

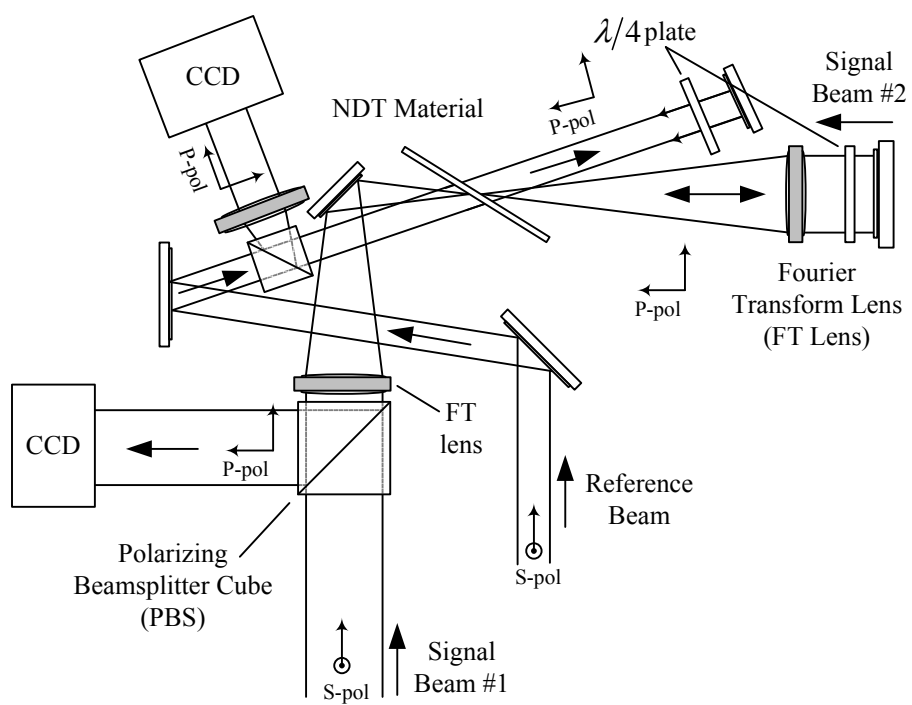


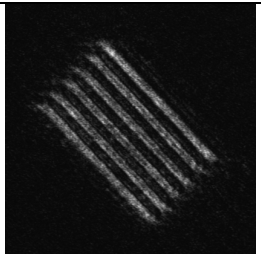
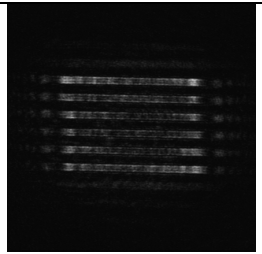
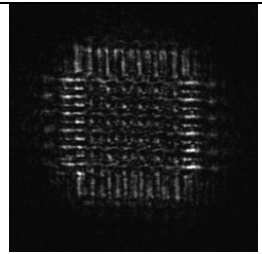
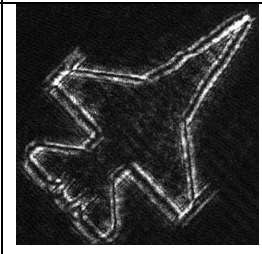
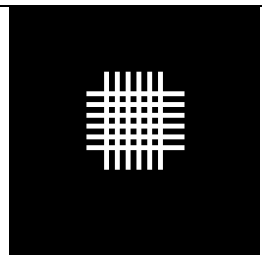
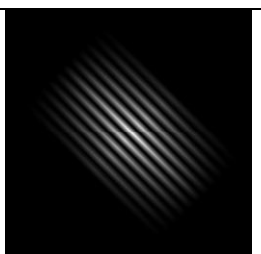
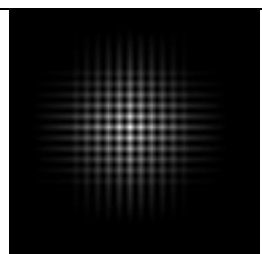
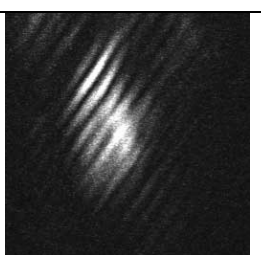
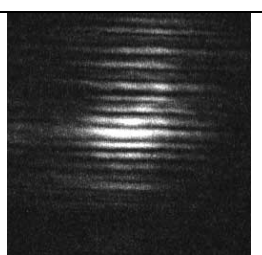
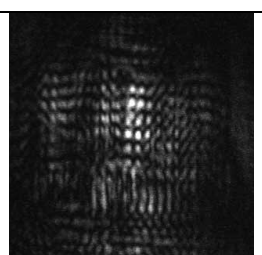
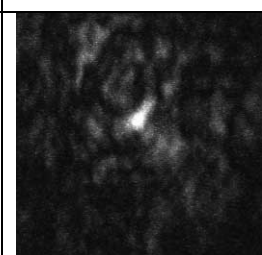
Figure 7-12: Diagram of Phase-conjugation/Correlation Experiment

Both the reference and signal beams are s-polarized. They arrive at the NDT material spaced 30 degrees apart from one another and another 30 degrees from the normal to the material. These angles satisfy the material restraints and provide a good diffraction efficiency.

In self-correlation mode, the signal beam #1 creates a grating with the reference beam, passes through the NDT material, and is retro-reflected by a mirror and through a quarter-wave plate. After the reflected beam passes through the Fourier transform lens, a Fourier transform of the reflection is incident on the NDT material and the grating that is being written by the two s-polarized beams. Because of the symmetry of the Fourier transform, this beam incident upon the gratings is exactly equal to the signal beam #1 but reversed in direction. When the retro-reflected beam arrives at the NDT material, it is polarized orthogonal to the beams that are writing the grating. The correlation beam that diffracts from the grating is also polarized in the p-plane and diffracts in the direction of the reference beam, as shown earlier. It is separated from the reference beam by a polarizing beamsplitter cube and is focused by a lens onto one of the CCD cameras. Because the signal beams #1 and #2 are identical, the self-correlation is obtained.

In phase-conjugation mode, the same grating is created between the reference and signal beam #1; however, in this mode the signal beam is blocked after the NDT material so that no retro-reflection occurs. Instead, a mirror and quarter-wave plate combination placed after the NDT material in the path of the reference beam retro-reflects the reference back to the material. The reflected reference is p-polarized and diffracts in the direction of the signal beam. As shown above, the diffracted beam is the phase conjugate of the signal beam #1 and is also polarized in the p-plane. A polarizing beamsplitter cube selects the phase-conjugate beam and directs it to a CCD camera.

Experimentally I proceeded in two stages. First, the phase-conjugation experiment was run to evaluate the material and to find the proper reference beam intensity level for edge enhancement. Second, the self-correlation experiment was run to determine if the experimental correlations matched the predicted correlation image patterns. Table 7-1 shows the results for four different images. Row 1 of the table shows the phase-conjugate image. The phase conjugate images in 1a and 1b are only mildly edge-enhanced. Compared to their original images 2a and 2b, the phase-conjugates show some loss of the DC component but not enough to render them completely high-pass filtered. The phase-conjugate images in Cell 1c and of the airplane in 1d both show edge-enhancement.

	a	b	c	d
1				
2				
3				
4				

**Table 7-1: Correlation and Phase Conjugation Results**

Row 3 of Table 7-1 shows the MATLAB computed self-correlation of each of the images shown above it in Row 2. Row 4 shows the experimental self-correlation result for each of the corresponding images in Row 2. The experimental correlation results are in good agreement with the predicted correlation results. There is some distortion present, which is caused by the thickness of the material and the lack of anti-reflection coatings. Each of the beams in the

material reflect from the opposite surface and back again. The reflections are generally not large, but the first reflections are significant enough to create secondary gratings that can add noise and distortion to the readout. Also, the readout beam will bounce inside the material and readout multiple copies of the correlation, spaced slightly apart. This problem can be eliminated by adding AR coatings to the glass substrates of the NDT material. Because we operate at a single wavelength, it is possible to suppress the reflections at better than 500:1, which is more than enough to eliminate this problem. The NDT material is still in the development phase and the cost of adding AR coatings is not justified at this point. However, it is a simple matter to use AR coated glass in subsequent experiments.

In order to further test the alignment of the material and the beams, another self-correlation test was run, this time using a pair of F-16 airplane images in a top-bottom configuration. The result is shown in Figure 7-13.

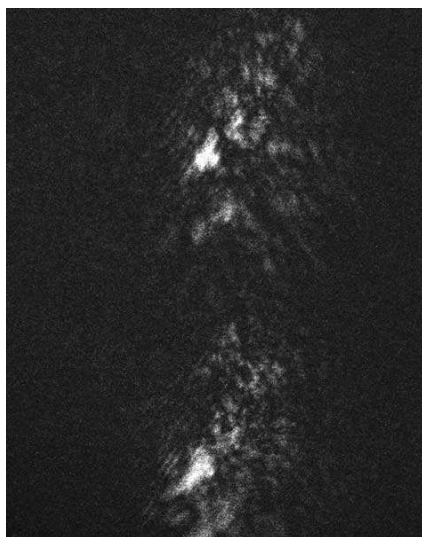


**Figure 7-13: Correlation of a Pair of Jets**

It was found that in order to have robust correlation, the alignment of the two Fourier transformed signal beams needed to be precise. The two beams needed to be as nearly counter-

propagating as possible to achieve clean correlation signals. It is possible that if the material were thinner, the alignment may not need to be quite as precise. The alignment issue can also be mitigated somewhat by using a longer focal length lens for the Fourier transform operation—a longer lens spreads the transform over more area, making it more tolerant to misalignment.

## **7.4 Conclusion and Next Steps**

The real-time Vanderlugt correlator shown here can be combined with a high-speed holographic data storage system to perform high-speed database searches. This has applications ranging from target detection to robot vision. The ultimate goal for the high-speed holographic smart eye system is to combine this type of correlator with a super-parallel holographic memory. However, while the SPHRAM is under development, the holographic smart eye concept has been tested using a more conventional disc-based holographic memory.

Several improvements could be made to the real-time correlator system. First and foremost, the material itself has several undesirable characteristics. It is typically made no smaller than 30 microns thick while anywhere between one and five microns allows enough translation invariance to cover the entire SLM screen. This material requires a high (2-3 kV) voltage to operate, which makes it impractical for a compact system. The material also has the tendency to develop semi-permanent ghost gratings when used for long periods of time. Also, the maximum diffraction efficiency of the material for 532 nm write and read is only about 50%.

Besides improving the material itself, the real-time correlator could be improved by using higher-quality AR-coated optics, along with higher precision polarization optics (half/quarter-wave plates, polarizing beamsplitter cubes). The polarizing beamsplitter cubes in particular are

designed for broadband applications, and as such do not provide a high level of polarization suppression.

These steps will increase the fidelity and strength of the correlation and ensure that the real-time correlator can handle an extensive search using a high-speed holographic memory as the input database

## 8 Holographic Smart Eye

### 8.1 Introduction

Many applications require rapid target identification. Defense applications include target tracking, friend or foe identification, and visual navigation for unmanned aerial vehicles (UAVs). Other applications include fingerprint identification, vegetation and pollution mapping, and robot vision. These applications all have the same structure: A target, or query, image has been acquired by a sensor. The query is to be identified by comparing it to a database of known images. Currently, these types of searches are performed by conventional or specialized electronics, while the databases themselves are stored on hard disks or optics discs. This processing is serial in nature, and the databases are limited in size by the storage medium.

A holographic optical correlator utilizes the parallelism that is inherent in optics to perform this type of search much faster than a conventional microchip. Because the input to an HOC is a two-dimensional data page (either binary/coded data or actual images) and the processing itself takes place at the speed of light, an HOC can offer speeds that are not currently possible with current systems.

However, an HOC requires a database that can be read at a very high speed in order to meet its full potential. A holographic database has two key advantages: one, the data is stored and read optically, thus eliminating a digital to optic conversion step. Two, holographic storage density is many times greater than current optical disc or hard disk technologies and the read speed can also be high, of the order of gigabytes per second.

In this chapter, I will describe how a holographic smart eye can be constructed for a variety of applications. I then show experimental results for a functional holographic smart eye

constructed in our laboratory. Finally, I will detail the next steps to be taken in the development of the holographic smart eye.

## 8.2 Holographic Smart Eye Overview

Suppose a query image is acquired by some type of imaging sensor, as demonstrated in Figure 8-1. An image might be acquired by a UAV to try to identify a landmark on the ground for visual navigation, or a fingerprint could be captured by a fingerprint scanner, or the image might be acquired by a visual targeting system aboard an aircraft or helicopter. Once the image has been captured, it can be sent to the correlation system.

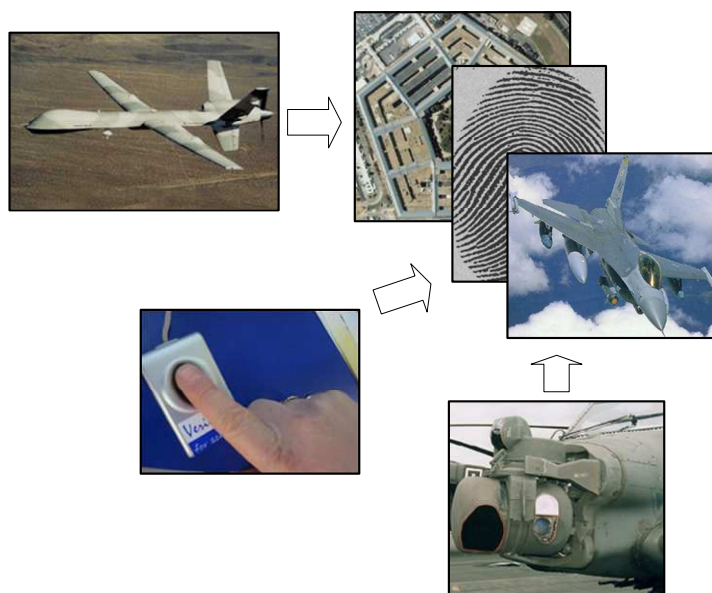


**Figure 8-1: Image Acquisition**

Shown in Figure 8-2 is a conceptualization of the holographic smart eye system. A diode laser (purple) beam is expanded, collimated, and sent through two different beamsplitters. One sends a portion of the beam to an SLM (shown in red and gold) while the other splits the remaining beam into two reference beams. One reference beam is directed through two galvo mirrors to the

holographic disc for readout. The other is directed by a mirror to the holographic optical correlator material (purple square).

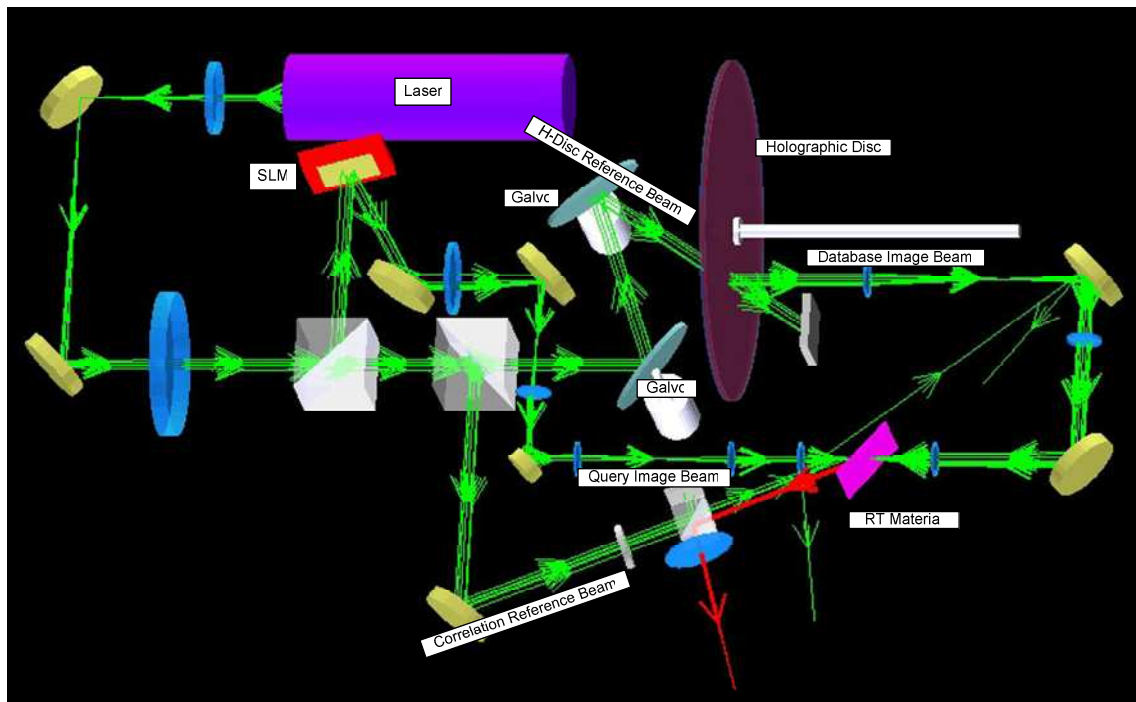


**Figure 8-2: Conceptualization of the Holographic Smart Eye**

Meanwhile, the beam from the SLM is relayed to the holographic correlator material from the left, and the holographic disc readout is transmitted to the correlator material from the right in a counter-propagating geometry. The diffracted beam, shown in red, is separated from the correlation reference beam by a beamsplitter and sent to a CCD camera or other sensor.

A compact geometry similar to the one shown here is the ultimate goal for the holographic smart eye project. In compact form, it could be deployed in all of the applications discussed here.

## **8.3 Experimental Design**

### **8.3.1 Introduction**

The holographic smart eye combines a disc-based holographic memory and a real-time Vanderlugt correlator to form a high-speed database search system. This implementation has been done at a prototype scale on an optical table.

The disc-based holographic memory system was described in Chapter 6, and the real-time correlation system was detailed in Chapter 7. Here, I will show how the two systems were interconnected and how the holographic smart eye operates in search mode. I present the experimental results for the holographic smart eye search and describe the operating software. Finally, I discuss how the system can be expanded and improved in the future.

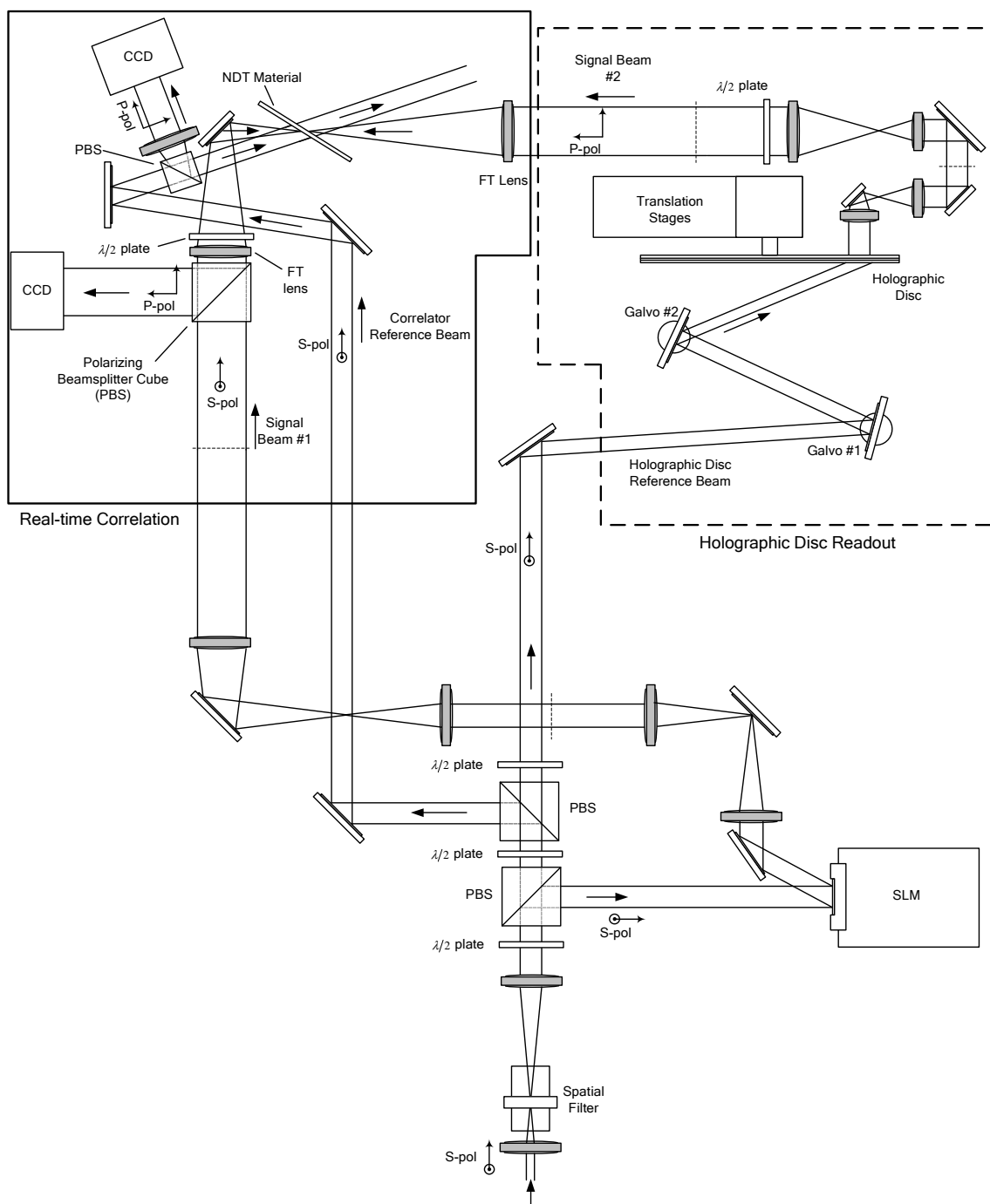
### **8.3.2 Experimental Setup**

The experimental setup is shown in Figure 8-3. At the bottom of the figure, the beam from the Coherent Verdi laser is sent through a spatial filter to homogenize the beam. After the beam is re-collimated, it is split into three parts: the un-deflected section continues forward to form the reference beam for reading from the holographic disc. Two polarizing beamsplitters are used to divert portions of the beam into the correlation reference beam and the correlation signal beam #1.

The first PBS deflects a portion of the beam to the spatial light modulator. There is a half-wave plate placed prior to the PBS that can be used to control the amount of light that is directed to the SLM. The SLM used in these experiments is the projector-based digital light projection SLM and is a reflective type. After picking up the signal image from the SLM, the signal beam is directed through a series of  $4f$  imaging systems to the real-time correlator. The

image plane of each  $4f$  system is marked by a dashed line across the image plane. A Fourier transform lens presents the Fourier transform of the final image plane to the NDT real-time holographic material.

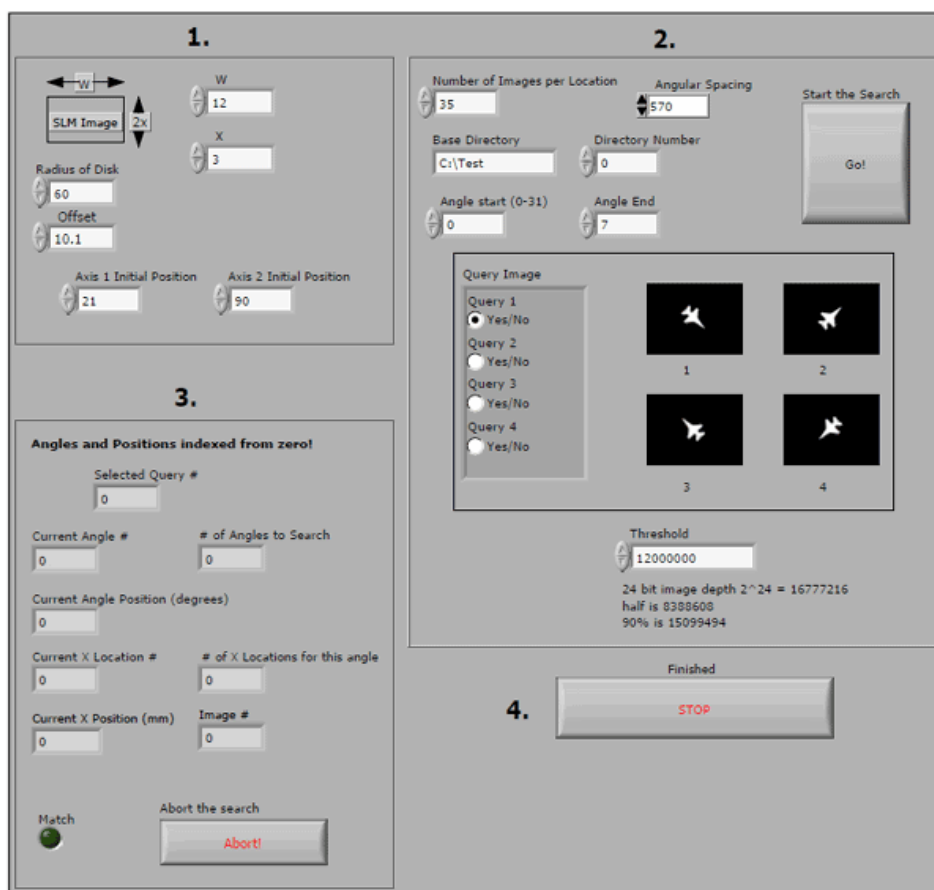
The second half-wave plate-PBS combination splits another portion of the beam to become the correlation reference beam. The un-deflected portion continues to a pair of galvo mirrors which can direct the beam at the proper angle to read out the holographic disc. The stored image is read out and passed through several  $4f$  imaging systems to bring the image to the real-time correlator. In Figure 8-3, the dashed box on the left denotes the components of the real-time correlator while the dashed box on the right contains those of the disc-based holographic memory.



**Figure 8-3: Experimental Design of the Holographic Smart Eye**

The holographic smart eye system is controlled by a LabVIEW program that is a modification of the code used to control the holographic disc memory. The program interface is shown in Figure 8-4. The user controls the offsets and initial positions as well as the disc

geometry first. Then they can adjust the writing parameters for that particular disc, such as the number of multiplexed images and the angular spacing between them. The user can also choose the portion of the holographic disc to search. Finally, the user must select a query image. In this control program, the query image is selected from among four pre-set images.

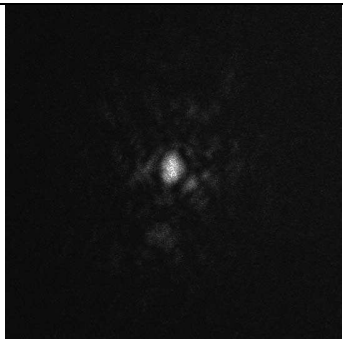
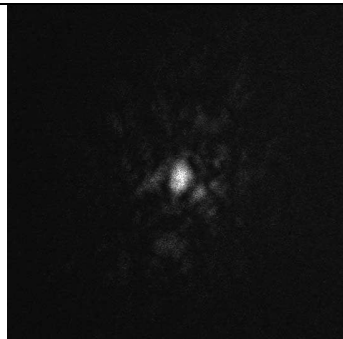
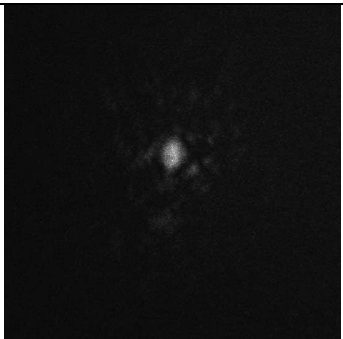


**Figure 8-4: Smart Eye Control Program**

However, the program is easily extendable to searching with any query image. The user must also select a threshold level. As the program searches, any correlation images with a peak higher than the threshold will register a correlation. The search proceeds automatically, with the data in Box 3 shown to provide the user with an update of which location and angle are currently being searched.

### 8.3.3 Results

The holographic smart eye was tested with one of the Aprilis holographic discs that had been written to test that media. The query image was image number 3 in Figure 8-4. The search was run three times to ensure that the result was consistent. The results of the correlation search are shown in Table 8-1.

Search #1	Search #2	Search #3
		

**Table 8-1: Results of the Holographic Smart Eye Search**

In order to produce consistent correlation results, it was necessary to ensure that the query image and the holographic database image beam paths were aligned exactly counter-propagating to each other. If this is done properly, inserting a white card at any of the image planes in the  $4f$  imaging systems in Figure 8-3 should show both images exactly in focus and aligned, one on each side.

In addition, it is necessary to have the proper intensity level ratio between the three beams interacting at the real-time holographic material. The query and reference beams must combine to create an edge-enhanced grating at the material, as described in Chapter 7. There must be enough intensity left in the holographic disc reference beam to read out the database image with enough intensity to register the correlation image. Because this reference beam is diffracted twice—once at the memory and then again at the real-time correlator, this beam

typically carries the bulk of the power. When tweaking the intensity level ratios, it is also important to ensure that the intensity of the query image beam does not rise too high. Because it has such a strong DC component, the intensity at that spot can cause a breakdown in the material if it is too intense, causing the voltage to burn a hole through the material and rendering it useless.

The grating formed in the NDT material is unstable. Vibration carried through the high-voltage cables to the material causes the grating strength to flicker, and, as a result, the correlation must be performed with an intense reference and query beam. This causes the material to carry a ghost grating, so that even when the grating is washed out by vibration, the residual ghost grating is enough to continue the operation. This makes it very difficult to perform multiple consecutive searches. If the grating could be maintained in a stable fashion, less power would be required, and ghost gratings would not be as much of a problem.

Stabilizing the grating is also important for making the correlation search as robust as possible. Currently, because the grating strength flickers, so too does the diffracted correlation output. This makes it difficult to set a threshold level that will give accurate results, especially when comparing similar images.

## ***8.4 Conclusion and Next Steps***

The holographic smart eye is made of two component systems—a real-time Vanderlugt correlator and a disc-based holographic memory. At this point, the system is limited in search speed by the disc-based holographic memory. The real-time correlator can support any increase in speed that can be obtained in the database image readout. Careful optimization of the LabVIEW control program should yield improvements on the galvo mirror seek time and

translation stage movement time. The CCD control software can also be improved.

Currently it is a custom code module using a TWAIN interface to the Epix software package, which in turn interfaces directly to the capture board in the computer. Source code can be purchased so that a custom code module could directly access the capture board, bypassing the slow TWAIN interface. The speed at which the CCD can capture correlations is the current limit on the overall search speed. Even without any changes to the translation stage and galvo code, an increase in the CCD access time can be used to increase the search speed of the system.

The search fidelity, on the other hand, is limited by the real-time correlator. Consistent and accurate results will require both an improved material as well as a better mechanical and optical system. Tests can be done to isolate the cause of the grating flicker in the NDT material. The likely cause is the high-voltage amplifier that is required to produce the 3kV bias. The generator itself has two large fans that disturb the air around the real-time correlator, which may be enough to cause the vibration effects we see. In addition, the wires that connect the voltage amplifier to the material may also transmit vibration directly to the sample. A system to isolate these cables from the vibration of the amplifier as well as a shield over the system to prevent any turbulent air from disturbing it may eliminate this problem. These improvements to the real-time correlator will ensure that when the SPHRAM is ready, the search speed will be limited only by the SPHRAM.

In addition to the improvements of the real-time correlator and disc-based holographic memory, the holographic search eye itself can be upgraded. The system hardware has the capability to receive wireless transmissions from a remote-guided helicopter mounted with a wireless CCD camera. This camera can transmit images to the host computer, which can then process the image and send it to the SLM as a query image. This capability could be

encapsulated in a custom code module and embedded into LabVIEW. This would allow the use of on-the-fly capture of query images for searching the database.

In summary, a functional holographic smart eye was constructed using a real-time Vanderlugt correlator and a disc-based holographic memory system. The system uses a real-time holographic material from Nitto Denko Corporation and a holographic data storage disc from Aprilis. I have described several improvements that can be made to the existing system without adding new hardware. In addition, once the SPHRAM is constructed, it can be added to the real-time Vanderlugt correlator to demonstrate very high-speed database searches. Finally, this holographic smart eye can be combined with a polarization-discriminating LADAR using a holographic Stokesmeter to create a polarization-sensitive search system. The massive storage capacity of a holographic database makes it an excellent candidate for storing both visual and polarimetric image signatures, and the SPHRAM provides high-speed access to the data. Combined with the holographic smart eye, the SPHRAM+HSE can search a large database and compare with the signatures acquired by the polarimetric LADAR.

## 9 References

1. D. Gabor, "A New Microscopic Principle," *Nature* **161**, 777-778 (1948).
2. Y. N. Denisyuk, "On the reflection of optical properties of an object in the wave field of light scattered by it," *Doklady Akademii Nauk SSSR* **144**, 1275-1278 (1962).
3. E. N. Leith and J. Upatniek, "Reconstructed Wavefronts and Communication Theory," *Journal of the Optical Society of America* **52**(10), 1123-1130 (1962).
4. Y. N. Denisyuk, "On the reflection of optical properties of an object in the wave field of light scattered by it," *Optika i Spektroskopija* **15**, 522-532 (1963).
5. E. N. Leith, A. Kozma, Upatniek, J. J. Marks, and N. Massey, "Holographic Data Storage in 3-Dimensional Media," *Applied Optics* **5**(8), 1303-& (1966).
6. H. Kogelnik, "Coupled Wave Theory for Thick Hologram Gratings," *Bell System Technical Journal* **48**(9), 2909-2947 (1969).
7. L. Dauria, J. P. Huignard, and E. Spitz, "Holographic Read-Write Memory and Capacity Enhancement by 3-D Storage," *Ieee Transactions on Magnetics* **MAG9**(2), 83-94 (1973).
8. A. Vanderlugt, "Design Relationships for Holographic Memories," *Applied Optics* **12**(7), 1675-1685 (1973).
9. S. K. Case, "Coupled-Wave Theory for Multiply Exposed Thick Holographic Gratings," *Journal of the Optical Society of America* **65**(6), 724-729 (1975).
10. D. Brady and D. Psaltis, "Information Capacity of 3-D Holographic Data-Storage," *Optical and Quantum Electronics* **25**(9), S597-S610 (1993).
11. K. Curtis, A. Pu, and D. Psaltis, "Method for Holographic Storage Using Peristrophic Multiplexing," *Optics Letters* **19**(13), 993-994 (1994).
12. J. F. Heanue, M. C. Bashaw, and L. Hesselink, "Channel Codes for Digital Holographic Data-Storage," *Journal of the Optical Society of America a-Optics Image Science and Vision* **12**(11), 2432-2439 (1995).
13. M. P. Bernal, H. Coufal, R. K. Grygier, J. A. Hoffnagle, C. M. Jefferson, R. M. Macfarlane, R. M. Shelby, G. T. Sincerbox, P. Wimmer, and G. Wittmann, "A precision tester for studies of holographic optical storage materials and recording physics," *Applied Optics* **35**(14), 2360-2374 (1996).
14. F. H. Mok, G. W. Burr, and D. Psaltis, "System metric for holographic memory systems," *Optics Letters* **21**(12), 896-898 (1996).
15. A. Pu and D. Psaltis, "High-density recording in photopolymer-based holographic three-dimensional disks," *Applied Optics* **35**(14), 2389-2398 (1996).
16. J. L. Sanford, P. F. Greier, K. H. Yang, M. Lu, R. S. Olyha, C. Narayan, J. A. Hoffnagle, P. M. Alt, and R. L. Melcher, "A one-megapixel reflective spatial light modulator system for holographic storage," *Ibm Journal of Research and Development* **42**(3-4), 411-426 (1998).
17. S. S. Orlov, W. Phillips, E. Bjornson, Y. Takashima, P. Sundaram, L. Hesselink, R. Okas, D. Kwan, and R. Snyder, "High-transfer-rate high-capacity holographic disk data-storage system," *Applied Optics* **43**(25), 4902-4914 (2004).
18. J.-K. Lee, J. T. Shen, and M. S. Shahriar, "Demonstration of a Spectrally Scanned Holographic Stokesmeter," in *Submitted to Optics Communications*, (2007).
19. J. K. Lee, J. T. Shen, and M. S. Shahriar, "Photonic Bandgap-based Stokesmeter," in *Work in progress*, (2007).

20. G. S. P. J.T. Shen, M.S. Shahriar, "Lenslet array for a super-parallel holographic memory," in *To be submitted*, (Northwestern University, 2007).
21. J. K. Lee, J. T. Shen, A. Heifetz, R. Tripathi, and M. S. Shahriar, "Demonstration of a thick holographic Stokesmeter," *Optics Communications* **259**(2), 484-487 (2006).
22. A. Heifetz, J. T. Shen, J. K. Lee, R. Tripathi, and M. S. Shahriar, "Translation-invariant object recognition system using an optical correlator and a super-parallel holographic random access memory," *Optical Engineering* **45**(2), - (2006).
23. A. Heifetz, G. S. Pati, J. T. Shen, J. K. Lee, M. S. Shahriar, C. Phan, and M. Yamamoto, "Shift-invariant real-time edge-enhanced VanderLugt correlator using video-rate compatible photorefractive polymer," *Applied Optics* **45**(24), 6148-6153 (2006).
24. H. N. Yum, P. R. Hemmer, A. Heifetz, J. T. Shen, J. K. Lee, R. Tripathi, and M. S. Shahriar, "Demonstration of a multiwave coherent holographic beam combiner in a polymeric substrate," *Optics Letters* **30**(22), 3012-3014 (2005).
25. M. S. Shahriar, J. T. Shen, M. A. Hall, R. Tripathi, J. K. Lee, and A. Heifetz, "Highly polarization-sensitive thick gratings for a holographic Stokesmeter," *Optics Communications* **245**(1-6), 67-73 (2005).
26. A. Heifetz, "Shift-Invariant Real-Time High-Speed Optical Image Correlation System," (Northwestern University, Evanston, IL, 2005).
27. H. N. Yum, P. R. Hemmer, R. Tripathi, J. T. Shen, and M. S. Shahriar, "Demonstration of a simple technique for determining the M/# of a holographic substrate by use of a single exposure," *Optics Letters* **29**(15), 1784-1786 (2004).
28. M. S. Shahriar, R. Tripathi, M. Huq, and J. T. Shen, "Shared-hardware alternating operation of a super-parallel holographic optical correlator and a super-parallel holographic random access memory," *Optical Engineering* **43**(8), 1856-1861 (2004).
29. M. S. Shahriar, J. T. Shen, R. Tripathi, M. Kleinschmit, T. W. Nee, and S. M. F. Nee, "Ultrafast holographic Stokesmeter for polarization imaging in real time," *Optics Letters* **29**(3), 298-300 (2004).
30. M. S. Shahriar, R. Tripathi, M. Kleinschmit, J. Donoghue, W. Weathers, M. Huq, and J. T. Shen, "Superparallel holographic correlator for ultrafast database searches," *Optics Letters* **28**(7), 525-527 (2003).
31. M. S. Shahriar, J. Riccobono, M. Kleinschmit, and J. T. Shen, "Coherent and incoherent beam combination using thick holographic substrates," *Optics Communications* **220**(1-3), 75-83 (2003).
32. J. W. Goodman, *Introduction to Fourier Optics* (McGraw-Hill, New York, 1996).
33. R. Magnusson and T. K. Gaylord, "Analysis of Multiwave Diffraction of Thick Gratings," *Journal of the Optical Society of America* **67**(9), 1165-1170 (1977).
34. D. J. C. L. Solymar, *Volume Holography and Volume Gratings* (Academic Press, London, 1981).
35. M. G. Moharam and T. K. Gaylord, "Rigorous coupled-wave analysis of planar-grating diffraction," *Journal of the Optical Society of America* **71**, 811-818 (1981).
36. G. Barbastathis and D. Psaltis, "Volume Holographic Multiplexing Methods," in *Holographic Data Storage*, H. J. Coufal, D. Psaltis, and G. T. Sincerbox, eds. (Springer-Verlag, Heidelberg, 2000).

37. X. An, D. Psaltis, and G. W. Burr, "Thermal fixing of 10,000 holograms in LiNbO<sub>3</sub> : Fe," *Applied Optics* **38**(2), 386-393 (1999).
38. A. Pu, K. Curtis, and D. Psaltis, "Exposure schedule for multiplexing holograms in photopolymer films," *Optical Engineering* **35**(10), 2824-2829 (1996).
39. H. J. Coufal, D. Psaltis, and G. T. Sincerbox, eds., *Holographic Data Storage*, Springer Series in Optical Sciences (Springer-Verlag, Berlin, 2000), Vol. 76.
40. G. Saxby, *Practical Holography*, 3 ed. (Taylor & Francis, 2003).
41. E. N. Leith, A. Kozma, J. Upatnieks, J. Marks, and N. Massey, "Holographic Data Storage in Three-Dimensional Media," *Applied Optics* **5**(8), 1303-1311 (1966).
42. D. Psaltis, D. Brady, and K. Wagner, "Adaptive Optical Networks Using Photorefractive Crystals," *Applied Optics* **27**(9), 1752-1759 (1988).
43. D. W. Diehl and N. George, "Holographic interference, filters for infrared communications," *Applied Optics* **42**(7), 1203-1210 (2003).
44. D. D. Do, N. Kim, J. W. An, and K. Y. Lee, "Effects of apodization on a holographic demultiplexer based on a photopolymer grating," *Applied Optics* **43**(23), 4520-4526 (2004).
45. H. J. Eichler, P. Kuemmel, S. Orlic, and A. Wappelt, "High-density disk storage by multiplexed microholograms," *Ieee Journal of Selected Topics in Quantum Electronics* **4**(5), 840-848 (1998).
46. X. L. Han, G. Kim, and R. T. Chen, "Accurate diffraction efficiency control for multiplexed volume holographic gratings," *Optical Engineering* **41**(11), 2799-2802 (2002).
47. U. S. Rhee, H. J. Caulfield, C. S. Vikram, and J. Shamir, "Dynamics of Hologram Recording in Dupont Photopolymer," *Applied Optics* **34**(5), 846-853 (1995).
48. J. J. Butler and M. S. Malcuit, "Diffraction properties of highly birefringent liquid-crystal composite gratings," *Optics Letters* **25**(6), 420-422 (2000).
49. D. A. Waldman, C. J. Butler, and D. H. Raguin, "CROP holographic storage media for optical data storage at greater than 100 bits/μm<sup>2</sup>," in *Organic Holographic Materials and Applications*, K. Meerholz, ed. (2003), pp. 10-25.
50. H. Y. Wei, L. C. Cao, G. Claire, Z. F. Xu, M. Z. He, Q. S. He, S. R. He, and G. F. Jin, "Holographic grating formation in cationic photopolymers with dark reaction," *Chinese Physics Letters* **23**(11), 2960-2963 (2006).
51. L. Dhar, A. Hale, H. E. Katz, M. L. Schilling, M. G. Schnoes, and F. C. Schilling, "Recording media that exhibit high dynamic range for digital holographic data storage," *Optics Letters* **24**(7), 487-489 (1999).
52. A. Veniaminov and E. Bartsch, "Diffusional enhancement of holograms: phenanthrenequinone in polycarbonate," *Journal of Optics a-Pure and Applied Optics* **4**(4), 387-392 (2002).
53. A. V. Veniaminov and E. Bartsch, "The shape of the relaxation curve in diffusion measurements with the aid of photoinduced gratings," *Optics and Spectroscopy* **101**(2), 290-298 (2006).
54. A. V. Veniaminov, E. Bartsch, and A. P. Popov, "Postexposure evolution of a photoinduced grating in a polymer material with phenanthrenequinone," *Optics and Spectroscopy* **99**(5), 744-750 (2005).

55. A. V. Veniaminov and Y. N. Sedunov, "Diffusion of phenanthrenequinone in poly(methyl methacrylate): Holographic measurements," *Vysokomolekulyarnye Soedineniya Seriya a & Seriya B* **38**(1), 71-76 (1996).
56. A. V. Veniaminov and H. Sillescu, "Polymer and dye probe diffusion in poly(methyl methacrylate) below the glass transition studied by forced Rayleigh scattering," *Macromolecules* **32**(6), 1828-1837 (1999).
57. J. Mumburu, I. Solomatine, D. Psaltis, S. H. Lin, K. Y. Hsu, W. Z. Chen, and W. T. Whang, "Comparison of the recording dynamics of phenanthrenequinone-doped poly(methyl methacrylate) materials," *Optics Communications* **194**(1-3), 103-108 (2001).
58. G. J. Steckman, I. Solomatine, G. Zhou, and D. Psaltis, "Characterization of phenanthrenequinone-doped poly(methyl methacrylate) for holographic memory," *Optics Letters* **23**(16), 1310-1312 (1998).
59. Y. N. Hsiao, W. T. Whang, and S. H. Lin, "Analyses on physical mechanism of holographic recording in phenanthrenequinone-doped poly(methyl methacrylate) hybrid materials," *Optical Engineering* **43**(9), 1993-2002 (2004).
60. Y. N. Hsiao, W. T. Whang, and S. H. Lin, "Effect of ZnMA on optical and holographic characteristics of doped PQ/PMMA photopolymer," *Japanese Journal of Applied Physics Part 1-Regular Papers Short Notes & Review Papers* **44**(2), 914-919 (2005).
61. K. Y. Hsu, S. H. Lin, Y. N. Hsiao, and W. T. Whang, "Experimental characterization of phenanthrenequinone-doped poly(methyl methacrylate) photopolymer for volume holographic storage," *Optical Engineering* **42**(5), 1390-1396 (2003).
62. R. Burzynski, D. N. Kumar, S. Ghosal, and D. R. Tyczka, "Holographic recording material," (2002).
63. O. Beyer, I. Nee, F. Havermeier, and K. Buse, "Holographic recording of Bragg gratings for wavelength division multiplexing in doped and partially polymerized poly(methyl methacrylate)," *Applied Optics* **42**(1), 30-37 (2003).
64. P. Boffi, M. C. Ubaldi, D. Piccinin, C. Frascolla, and M. Martinelli, "1550-nm Volume Holography for Optical Communication Devices," *IEEE Photonics and Technology Letters* **12**(10), 1355-1357 (2000).
65. S. F. Chen, C. S. Wu, and C. C. Sun, "Design for a high dense wavelength division multiplexer based on volume holographic gratings," *Optical Engineering* **43**(9), 2028-2033 (2004).
66. D. D. Do, S. K. Park, J. W. An, N. Kim, and K. Y. Lee, "Gaussian apodized volume grating to suppress the crosstalk in holographic demultiplexers using high-efficiency photopolymers," *Optical Engineering* **43**(9), 2022-2027 (2004).
67. G. A. Rakuljic and V. Leyva, "Volume Holographic Narrow-Band Optical Filter," *Optics Letters* **18**(6), 459-461 (1993).
68. A. Sato, M. Scepanovic, and R. K. Kostuk, "Holographic edge-illuminated polymer Bragg gratings for dense wavelength division optical filters at 1550 nm," *Applied Optics* **42**(5), 778-784 (2003).
69. G. Q. Zhang, G. Montemezzani, and P. Gunter, "Narrow-bandwidth holographic reflection filters with photopolymer films," *Applied Optics* **40**(15), 2423-2427 (2001).
70. F. Zhao, J. Qiao, X. G. Deng, J. Z. Zou, B. P. Guo, R. Collins, V. Villavicencio, K. K. Chang, J. W. Horwitz, B. Morey, and R. T. Chen, "Reliable grating-based wavelength

- division (de)multiplexers for optical networks," *Optical Engineering* **40**(7), 1204-1211 (2001).
71. F. Zhao, Y. Zhang, J. Z. Zou, Z. Shi, B. Bihari, E. Frietman, X. G. Deng, J. Qiao, Z. Shi, and R. T. Chen, "Wavelength division multiplexers/demultiplexers for optical interconnects in massively parallel processing," *Optical Engineering* **42**(1), 273-280 (2003).
  72. M. S. Shahriar, M. Andrews, S. Tseng, J. Kuykendall, A. Meshal, and N. Valletero, "An Optical Network Integration Platform Based on Holographic Super-dense Wdm Filters," in *Army Science Conference*, (Orlando, FL, 2006).
  73. S. Ahmed and E. N. Glytsis, "Comparison of beam propagation method and rigorous coupled-wave analysis for single and multiplexed volume gratings," *Applied Optics* **35**(22), 4426-4435 (1996).
  74. P. Yeh, *Introduction to Photorefractive Nonlinear Optics* (Wiley, 1993).
  75. G. P. Nordin, J. T. Meier, P. C. Deguzman, and M. W. Jones, "Micropolarizer array for infrared imaging polarimetry," *Journal of the Optical Society of America a-Optics Image Science and Vision* **16**(5), 1168-1174 (1999).
  76. H. D. M. K.P. Bishop, M.P. Fetrow, L. McMackin, "Multispectral polarimeter imaging in the visible to near-IR, Targets and Backgrounds: Characterization and Representation," *Proceedings of the SPIE* **3699**(1999).
  77. J. L. Pezzaniti and R. A. Chipman, "Mueller Matrix Imaging Polarimetry," *Optical Engineering* **34**(6), 1558-1568 (1995).
  78. W. S. Bickel and W. M. Bailey, "Stokes Vectors, Mueller Matrices, and Polarized Scattered-Light," *American Journal of Physics* **53**(5), 468-478 (1985).
  79. D. R. H. C. Bohren, *Absorption and scattering of light by small particles* (Wiley, 1998).
  80. M. G. L.J. Denes, B. Kaminsky, D. Huber, "Spectro-polarimetric imaging for object recognition," *Proceedings of the SPIE* **3240**(1998).
  81. S. F. N. T. Nee, "Infrared polarization signatures for targets," *Proceedings of the SPIE* **2469**(1995).
  82. W. G. Egan, "Polarization in remote sensing," *Proceedings of the SPIE* **1747**(1992).
  83. C. W. D. Kim, K. Vaccaro, C. Woods, "Imaging multispectral polarimetric sensor: single-pixel design, fabrication, and characterization," *Applied Optics* **42**(19), 3756-3764 (2003).
  84. S. M. Nee and T. W. Nee, "Principal Mueller matrix of reflection and scattering measured for a one-dimensional rough surface," *Optical Engineering* **41**(5), 994-1001 (2002).
  85. J. M. B. A. Gerrard, *Introduction to Matrix Methods for Optics* (Dover Publications, New York, 1974).
  86. H. Kogelnik, "Coupled Wave Theory for Thick Hologram Gratings," *Bell System Technical Journal* **48**(9), 2909-+ (1969).
  87. A. M. L. D.S. Sabatke, M.R. Descour, W.C. Sweatt, J.P. Garcia, E.L. Dereniak, S.A. Kemme, G.S. Phillips, "Figures of merit for complete Stokes polarimeter optimization," *Proceedings of the SPIE* **4133**, 75-81 (2000).
  88. A. Ambirajan and D. C. Look, "Optimum Angles for a Polarimeter .1.," *Optical Engineering* **34**(6), 1651-1655 (1995).

89. S. Habraken, Y. Renotte, S. Roose, E. Stijns, and Y. Lion, "Design for Polarizing Holographic Optical-Elements," *Applied Optics* **34**(19), 3595-3602 (1995).
90. C. Carre, S. Habraken, and S. Roose, "Computer-Originated Polarizing Holographic Optical-Element Recorded in Photopolymerizable Layers," *Optics Letters* **18**(9), 738-740 (1993).
91. G. L. Schuster and J. R. Andrews, "Coherent Summation of Saturated Algaas Amplifiers," *Optics Letters* **18**(8), 619-621 (1993).
92. P. Hariharan, *Optical Holography: Principles, techniques, and applications* (Cambridge University Press, New York, 1996).
93. M. S. S. P. Hemmer, J. Ludman, H.J. Caulfield, "Holographic Optical Memories," in *Holography for the New Millenium* H. J. C. J. Ludman, and J. Riccobono, ed. (Springer-Verlag, New York, 2002).
94. J. H. Zhao, P. H. Yeh, M. Khoshnevisan, and I. McMichael, "Diffraction properties of vector synthetic volume index gratings," *Journal of the Optical Society of America B-Optical Physics* **17**(6), 898-903 (2000).
95. A. Yariv, *Quantum Electronics* (Wiley, New York, 1989).
96. J. R. J.E. Ludman, N. Reinhand, Yu Korzinin, I. Semenova, M.S. Shahriar, "Nonspatial filter for laser beams," *Kvantovaya Elektronika* **26**(12), 1093-1096 (1996).
97. J. E. Ludman, J. R. Riccobono, N. O. Reinhand, I. V. Semenova, Y. L. Korzinin, S. M. Shahriar, H. J. Caulfield, J. M. Fournier, and P. Hemmer, "Very thick holographic nonspatial filtering of laser beams," *Optical Engineering* **36**(6), 1700-1705 (1997).
98. D. N. K. R. Burzynski, M.K. Casstevens, D. Tyczka, S. Ghosal, P.M. Kurtz, J.F. Weibel, "," Proc. SPIE 4087, s Eds., 741-753 (2000). "New Photopolymer for Holographic Optical Storage Technology," *Proceedings of the SPIE* **4087**, 741-753 (2000).
99. A. H. B. G. Bekefi, *Electromagnetic Vibration, Waves, and Radiation* (MIT Press, Cambridge, 1990).
100. W. W. Goj, *Synthetic-Aperture Radar & Electronic Warfare* (Artec House, New York, 1992).
101. D. Stranneby, *Digital Signal Processing: DSP and Applications* (Newnes, Oxford, 2001).
102. C. Gu, H. Fu, and J. R. Lien, "Correlation patterns and cross-talk noise in volume holographic optical correlators," *Journal of the Optical Society of America A*. **12**, 861 (1995).
103. A. Pu, R. Denkewalter, and D. Psaltis, "Real-time vehicle navigation using a holographic memory," *Optical Engineering* **36**(10), 2737-2746 (1997).
104. K. Curtis and D. Psaltis, "3-Dimensional Disk-Based Optical Correlator," *Optical Engineering* **33**(12), 4051-4054 (1994).
105. G. W. Burr, S. Kobras, H. Hanssen, and H. Coufal, "Content-addressable data storage by use of volume holograms," *Applied Optics* **38**(32), 6779-6784 (1999).
106. L. C. Cao, Q. S. He, C. Ouyang, Y. Liao, and G. F. Jin, "Improvement to human-face recognition in a volume holographic correlator by use of speckle modulation," *Applied Optics* **44**(4), 538-545 (2005).
107. T. J. Suleski and R. D. Kolste, "Fabrication Trends for Free-Space Microoptics," *Journal of Lightwave Technology* **23**(2), 633-646 (2005).
108. N. F. Borrelli, *Microoptics Technology* (Marcel Dekker, 2005).

109. T. Suleski, D. C. O'Shea, A. D. Kathman, and D. Prather, *Diffraction Optics: Design, Fabrication, and Test* (SPIE Press, 2003).
110. S. Sinzinger and J. Jahns, *Microoptics* (Wiley-VCH, 2003).
111. B. E. A. Saleh and M.C. Teich, *Fundamentals of Photonics* (John Wiley & Sons, 1991).
112. L. Hesselink, S. S. Orlov, and M. C. Bashaw, "Holographic data storage systems," *Proceedings of the Ieee* **92**(8), 1231-1280 (2004).
113. G. W. Burr, "Holographic data storage with arbitrarily misaligned data pages," *Optics Letters* **27**(7), 542-544 (2002).
114. G. W. Burr, J. Ashley, H. Coufal, R. K. Grygier, J. A. Hoffnagle, C. M. Jefferson, and B. Marcus, "Modulation coding for pixel-matched holographic data storage," *Optics Letters* **22**(9), 639-641 (1997).
115. I. McMichael, W. Christian, D. Pletcher, T. Y. Chang, and J. H. Hong, "Compact holographic storage demonstrator with rapid access," *Applied Optics* **35**(14), 2375-2379 (1996).
116. G. Zhou, D. Psaltis, and F. Mok, "Holographic read-only memory," *Optical and Quantum Electronics* **32**(3), 405-417 (2000).
117. C. Moser, W. H. Liu, Y. Fainman, and D. Psaltis, "Folded shift multiplexing," *Optics Letters* **28**(11), 899-901 (2003).
118. P. Boffi, D. Piccinin, M. C. Ubaldi, and M. Martinelli, "All-optical pattern recognition for digital real-time information processing," *Applied Optics* **42**(23), 4670-4680 (2003).
119. L. Hesselink, "Materials requirements for dense optical data storage," *Glass Science and Technology* **75**, 39-50 (2002).
120. G. J. Steckman, A. Pu, and D. Psaltis, "Storage density of shift-multiplexed holographic memory," *Applied Optics* **40**(20), 3387-3394 (2001).
121. G. W. Burr and T. Weiss, "Compensation for pixel misregistration in volume holographic data storage," *Optics Letters* **26**(8), 542-544 (2001).
122. G. W. Burr, C. M. Jefferson, H. Coufal, M. Jurich, J. A. Hoffnagle, R. M. Macfarlane, and R. M. Shelby, "Volume holographic data storage at areal density of 250 gigapixels/in.<sup>2</sup>," *Optics Letters* **26**(7), 444-446 (2001).
123. A. Adibi, K. Buse, and D. Psaltis, "Two-center holographic recording," *Journal of the Optical Society of America B-Optical Physics* **18**(5), 584-601 (2001).
124. C. Moser, I. Maravic, B. Schupp, A. Adibi, and D. Psaltis, "Diffraction efficiency of localized holograms in doubly doped LiNbO<sub>3</sub> crystals," *Optics Letters* **25**(17), 1243-1245 (2000).
125. I. G. Kim, M. Lee, S. Takekawa, Y. Furukawa, K. Kitamura, L. Galambos, and L. Hesselink, "Volume holographic storage in near-stoichiometric LiNbO<sub>3</sub> : Ce,Mn," *Japanese Journal of Applied Physics Part 2-Letters* **39**(11A), L1094-L1096 (2000).
126. L. Hesselink, "Ultra-high-density data storage," *Communications of the Acm* **43**(11), 33-36 (2000).
127. W. H. Liu and D. Psaltis, "Pixel size limit in holographic memories," *Optics Letters* **24**(19), 1340-1342 (1999).
128. M. Levene, G. J. Steckman, and D. Psaltis, "Method for controlling the shift invariance of optical correlators," *Applied Optics* **38**(2), 394-398 (1999).

129. K. Buse, A. Adibi, and D. Psaltis, "Efficient non-volatile holographic recording in doubly doped lithium niobate," *Journal of Optics a-Pure and Applied Optics* **1**(2), 237-238 (1999).
130. A. Adibi, K. Buse, and D. Psaltis, "Multiplexing holograms in LiNbO<sub>3</sub> : Fe : Mn crystals," *Optics Letters* **24**(10), 652-654 (1999).
131. L. Dhar, K. Curtis, M. Tackitt, M. Schilling, S. Campbell, W. Wilson, A. Hill, C. Boyd, N. Levinos, and A. Harris, "Holographic storage of multiple high-capacity digital data pages in thick photopolymer systems," *Optics Letters* **23**(21), 1710-1712 (1998).
132. W. C. Chou and M. A. Neifeld, "Interleaving and error correction in volume holographic memory systems," *Applied Optics* **37**(29), 6951-6968 (1998).
133. G. W. Burr, W. C. Chou, M. A. Neifeld, H. Coufal, J. A. Hoffnagle, and C. M. Jefferson, "Experimental evaluation of user capacity in holographic data-storage systems," *Applied Optics* **37**(23), 5431-5443 (1998).
134. G. W. Burr, G. Barking, H. Coufal, J. A. Hoffnagle, C. M. Jefferson, and M. A. Neifeld, "Gray-scale data pages for digital holographic data storage," *Optics Letters* **23**(15), 1218-1220 (1998).
135. M. P. Bernal, G. W. Burr, H. Coufal, and M. Quintanilla, "Balancing interpixel cross talk and detector noise to optimize areal density in holographic storage systems," *Applied Optics* **37**(23), 5377-5385 (1998).
136. R. M. Shelby, J. A. Hoffnagle, G. W. Burr, C. M. Jefferson, M. P. Bernal, H. Coufal, R. K. Grygier, H. Gunther, R. M. Macfarlane, and G. T. Sincerbox, "Pixel-matched holographic data storage with megabit pages," *Optics Letters* **22**(19), 1509-1511 (1997).
137. G. Barbastathis, M. Levene, and D. Psaltis, "Shift multiplexing with spherical reference waves," *Applied Optics* **35**(14), 2403-2417 (1996).
138. H. Y. S. Li and D. Psaltis, "Alignment Sensitivity of Holographic 3-Dimensional Disks," *Journal of the Optical Society of America a-Optics Image Science and Vision* **12**(9), 1902-1912 (1995).
139. A. Vanderlugt, "Signal Detection by Complex Spatial Filtering," *Journal of the Optical Society of America* **53**(11), 1341-& (1963).
140. C. S. Weaver and J. W. Goodman, "A Technique for Optically Convolution 2 Functions," *Applied Optics* **5**(7), 1248-& (1966).
141. Z. Zalevsky, A. Rubner, J. Garcia, P. Garcia-Martinez, C. Ferreira, and E. Marom, "Joint transform correlator with spatial code division multiplexing," *Applied Optics* **45**(28), 7325-7333 (2006).
142. V. H. Diaz-Ramirez, V. Kober, and J. Alvarez-Borrego, "Pattern recognition with an adaptive joint transform correlator," *Applied Optics* **45**(23), 5929-5941 (2006).
143. E. Watanabe and K. Kodate, "Implementation of a high-speed face recognition system that uses an optical parallel correlator," *Applied Optics* **44**(5), 666-676 (2005).
144. T. Yao and T. Minemoto, "Hybrid nonlinear joint transform correlator that operates at a high frame rate," *Applied Optics* **42**(26), 5290-5301 (2003).
145. S. H. Shin and B. Javidi, "Three-dimensional object recognition by use of a photorefractive volume holographic processor," *Optics Letters* **26**(15), 1161-1163 (2001).
146. R. Ryf, G. Montemezzani, P. Gunter, A. A. Grabar, I. M. Stoika, and Y. M. Vysochanskii, "High-frame-rate joint Fourier-transform correlator based on Sn<sub>2</sub>P<sub>2</sub>S<sub>6</sub> crystal," *Optics Letters* **26**(21), 1666-1668 (2001).

147. S. Bartkiewicz, P. Sikorski, and A. Miniewicz, "Optical image correlator realized with a hybrid liquid-crystal-photoconducting polymer structure," *Optics Letters* **23**(22), 1769-1771 (1998).
148. I. Glaser, "Compact Lenslet-Array-Based Holographic Correlator Convolver," *Optics Letters* **20**(14), 1565-1567 (1995).
149. G. Asimellis, J. Khoury, J. Kane, and C. Woods, "Two-port photorefractive joint-transform correlator," *Optics Letters* **20**(24), 2517-2519 (1995).
150. A. Partovi, A. M. Glass, T. H. Chiu, and D. T. H. Liu, "High-Speed Joint-Transform Optical-Image Correlator Using Gaas/Algaas Semiinsulating Multiple-Quantum Wells and Diode-Lasers," *Optics Letters* **18**(11), 906-908 (1993).
151. F. T. S. Yu, S. D. Wu, S. Rajan, and D. A. Gregory, "Compact Joint Transform Correlator with a Thick Photorefractive Crystal," *Applied Optics* **31**(14), 2416-2418 (1992).
152. H. Rajbenbach, S. Bann, P. Refregier, P. Joffre, J. P. Huignard, H. S. Buchkremer, A. S. Jensen, E. Rasmussen, K. H. Brenner, and G. Lohman, "Compact Photorefractive Correlator for Robotic Applications," *Applied Optics* **31**(26), 5666-5674 (1992).
153. D. T. H. Liu and L. J. Cheng, "Real-Time Vanderlugt Optical Correlator That Uses Photorefractive Gaas," *Applied Optics* **31**(26), 5675-5680 (1992).
154. T. Iwaki and Y. Mitsuoka, "Optical-Pattern Recognition of Letters by a Joint-Transform Correlator Using a Ferroelectric Liquid-Crystal Spatial Light-Modulator," *Optics Letters* **15**(21), 1218-1220 (1990).

## 10 Appendices

### 10.1 Coupled-wave Theory

The coupled-wave theory approach to volume holographic gratings has been pursued by several authors. This Appendix shows an addition to the theory when more than one grating (multiplexed gratings) is considered, and derives the condition necessary for 100% efficient diffraction from all gratings.

Figure 10-1 illustrates the basic model used in this analysis. For simplicity, we consider first the combination of two read beams incident on a hologram with two gratings. We will then extrapolate the result for  $N$  beams and  $N$  gratings.

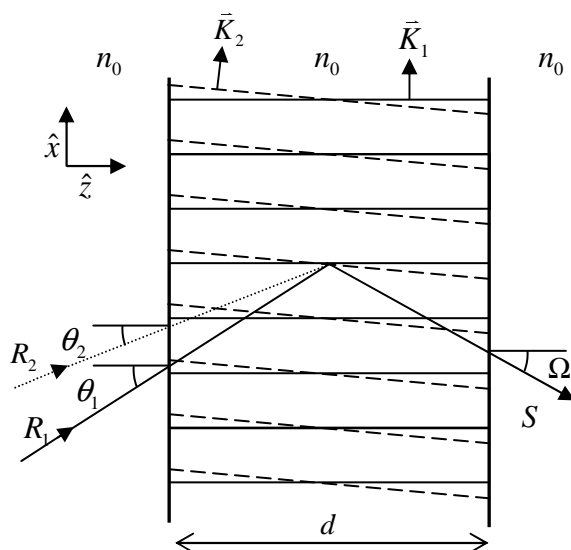


**Figure 10-1: Two Multiplexed Volume Gratings**

A further simplification is the assumption that the index of refraction is the same throughout the system. This model is used merely to simplify the notation. In reality the input and output angles would have to take into account refraction at the entrance and exit surfaces.

The scalar wave equation for this system can be written as:

$$\nabla^2 E(x, z) + k^2 E(x, z) = 0 \quad (10.1)$$

where  $k$  is the wavenumber, and  $E$  is the electric field describing all the oscillatory fields at the degenerate frequency,  $\omega$ . Here, we assume the field to be TE polarized. An extension to TM or arbitrary polarization can be made in the same manner as illustrated in reference 13. We also assume that the field does not vary in the  $y$  direction, and express the field as the sum of the input ( $R_1$  and  $R_2$ ) and the output ( $S$ ) waves:

$$E(x, z) = R_1(z) e^{-i\bar{\rho}_1 \cdot \bar{x}} + R_2(z) e^{-i\bar{\rho}_2 \cdot \bar{x}} + S(z) e^{-i\bar{\sigma} \cdot \bar{x}} \quad (10.2)$$

The wavevectors for each of these beams are assumed to be of the same magnitude:

$$\rho_1^2 = \rho_2^2 \equiv \beta^2 \quad (10.3)$$

$$\sigma^2 = \beta^2 \quad (10.4)$$

We also assume Bragg matching for each input beam:

$$\vec{\sigma} = \vec{\rho}_1 - \vec{K}_1 = \vec{\rho}_2 - \vec{K}_2 \quad (10.5)$$

where  $\vec{K}_1$  and  $\vec{K}_2$  are the grating vectors. Using phase matching terms, in the slowly-varying envelope approximation (SVEA) [22], the wave equation reduces to:

$$C_{R1} \frac{\partial R_1}{\partial z} = -i\kappa_1 S \quad (10.6)$$

$$C_{R1} \frac{\partial R_1}{\partial z} = -i\kappa_1 S \quad (10.7)$$

$$C_S \frac{\partial S}{\partial z} = -i\kappa_1 R_1 - i\kappa_2 R_2$$

Where

$$C_S = \cos \Omega \quad (10.8)$$

$$C_S = \cos \Omega \quad (10.9)$$

$$\kappa_j = \frac{\pi n_j}{\lambda}, \quad (j=1,2) \quad (10.10)$$

Here,  $n_1$  and  $n_2$  are the amplitudes of the index modulations, defined by:

$$n(x, z) = n_0 + n_1 \cos \overline{K_1} \cdot \overline{x} + n_2 \cos \overline{K_2} \cdot \overline{x} \quad (10.11)$$

Using boundary conditions that  $R_1(0) = r_1$  (complex),  $R_2(0) = r_2$  (complex), and  $S(0) = 0$ , the solutions to these equations, evaluated at the exit surface, become:

$$R_1(d) = \kappa_2 A + \kappa_1 C_{R2} B \cdot \cos(\alpha_0 d) \quad (10.12)$$

$$R_2(d) = \kappa_2 A + \kappa_1 C_{R2} B \cdot \cos(\alpha_0 d) \quad (10.13)$$

$$S(d) = -iC \cdot \sin(\alpha_0 d) \quad (10.14)$$

Where

$$A = \frac{C_{R1} \kappa_2 r_1 - C_{R2} \kappa_1 r_2}{C_{R1} \kappa_2^2 + C_{R2} \kappa_1^2} \quad (10.15)$$

$$B = \frac{\kappa_1 r_1 + \kappa_2 r_2}{C_{R1} \kappa_2^2 + C_{R2} \kappa_1^2} \quad (10.16)$$

$$C = (\kappa_1 r_1 + \kappa_2 r_2) \cdot \left( \frac{C_{R1} C_{R2}}{C_S (C_{R1} \kappa_2^2 + C_{R2} \kappa_1^2)} \right)^{1/2} \quad (10.17)$$

$$\alpha_0 = \left( \frac{C_{R1} \kappa_2^2 + C_{R2} \kappa_1^2}{C_{R1} C_{R2} C_S} \right)^{1/2} \quad (10.18)$$

These equations are formulated in a way such that the energy flow is conserved in the z-direction:

$$C_{R1} |R_1|^2 + C_{R2} |R_2|^2 = C_S |S|^2 \quad (10.19)$$

The intensity of the diffracted beam is  $I_d = F |S|^2$ , where the obliquity factor,  $F$ , is given by:

$$F = \frac{r_1^2 + r_2^2 - |R_1(d)|^2 - |R_2(d)|^2}{|S(d)|^2} \quad (10.20)$$

The diffraction efficiency,  $\eta$ , is given by:  $\eta \equiv I_d / (r_1^2 + r_2^2)$ , where  $\eta = 1$  corresponds to the situation where the intensity of  $R_1$  and  $R_2$  fall to zero at the output, indicating that all of the incident power has been transferred to the diffracted beams.

One possible condition for achieving  $\eta = 1$  is:  $d = \pi/2\alpha_0$  and

$$\frac{r_1}{r_2} = \frac{\kappa_1}{\kappa_2} \cdot \frac{C_{R2}}{C_{R1}} \quad (10.21)$$

$$\frac{r_1}{r_2} = \frac{\kappa_1}{\kappa_2} \cdot \frac{C_{R2}}{C_{R1}} \quad (10.22)$$

For symmetry, one can then infer that the general condition for  $\eta = 1$  with  $n$  input beams is:

$$\frac{C_{R1} \cdot r_1}{\kappa_1} = \frac{C_{R2} \cdot r_2}{\kappa_2} = \frac{C_{R3} \cdot r_3}{\kappa_3} = \dots = \frac{C_{Rn} \cdot r_n}{\kappa_n} \quad (10.23)$$

And:

$$d = \frac{\pi}{2} \cdot \sqrt{C_S} \cdot \left[ \sum_{j=1}^n \frac{\kappa_j^2}{C_{Rj}} \right]^{-\frac{1}{2}} \quad (10.24)$$

This result shows that it is possible to combine  $N$  mutually coherent beams with 100% efficiency, provided some constraints are met.

## 10.2 Fourier Optics and the Lens

The application of Fourier theory to optics is an entire field of study in its own right; here, I show a few results that are often used in optics and optical design. For a complete treatment of the

subject, I recommend Goodman's *Introduction to Fourier Optics*, which is the source for the material reviewed here.

The basic tenant of Fourier theory is that any function  $g(x)$  can be represented as a weighted sum of complex exponentials:

$$g(x) = \int_{-\infty}^{\infty} G(f) e^{i2\pi f x} df \quad (10.25)$$

Of course, there are criteria that must be met for equation (10.25) to be true, but without delving into the details, it is sufficient to note that in all the cases dealt with in this thesis, the conditions are satisfied. Although some readers may be familiar with the Fourier transform as a one dimensional relationship between time and frequency, the transform can also be defined in two dimensions relating space and spatial frequency:

$$g(x, y) = \int_{-\infty}^{\infty} \int_{-\infty}^{\infty} G(f_x, f_y) e^{i2\pi(f_x x + f_y y)} df_x df_y \quad (10.26)$$

How does the Fourier transform apply to optics? Suppose that we consider  $g(x, y)$  to be the electric field amplitude distribution of a plane wave:

$$E(x, y, z, t) = g(x, y) e^{i(\omega t - kz)} \quad (10.27)$$

By plugging equation (10.26) into equation (10.27) and considering the complex amplitude only:

$$U(x, y, z) = \int_{-\infty}^{\infty} \int_{-\infty}^{\infty} G(f_x, f_y) e^{i2\pi(f_x x + f_y y)} e^{ikz} df_x df_y \quad (10.28)$$

Thus, we can consider an image-bearing plane wave  $g(x, y) e^{ikz}$  to be made up of a infinite weighted-sum of plane waves, each traveling in a direction  $\theta_x = \sin^{-1}(\lambda f_x)$  and  $\theta_y = \sin^{-1}(\lambda f_y)$ .

Many optical systems can be considered to be linear and invariant and because of this, the input and output of an optical system can be related by the so-called impulse response of the system:

$$g_2(x, y) = \int_{-\infty}^{\infty} \int_{-\infty}^{\infty} g_1(\xi, \eta) h(x - \xi, y - \eta) d\xi d\eta \quad (10.29)$$

The form of the integral in equation (10.29) is called the convolution integral, and (10.29) represents the convolution of the input function  $g_1$ , with the impulse response of the system  $h$  and the output of the system is  $g_2$ .

By using the convolution theorem of the Fourier transform, we can instead relate the functions  $G_2$  and  $G_1$  by using the transfer function of the system,  $H$ :

$$G_2 = HG_1 \quad (10.30)$$

Many times it is easier to calculate the Fourier transforms  $G_1$  and  $H$ , perform the multiplication to find  $G_2$ , and then inverse Fourier transform to obtain  $g_2$ , rather than to calculate the convolution integral. Also, it can be more physically intuitive to view an optical system in the spatial frequency domain—the form of  $H$  can reveal the effect that the optical system will have on an incoming beam of light. The multiplication of  $H$  and  $G_1$  shows the effect that  $H$  can have: for each  $f_x$  and  $f_y$ , a complex number  $H$  is multiplied with  $G_1$  to obtain the resulting spatial frequency distribution. We can calculate the transfer function  $H$  for an optical system, or even for free space. The transfer function of free space is given by:

$$H(f_x, f_y) = \begin{cases} \exp\left[i2\pi \frac{z}{\lambda} \sqrt{1 - (\lambda f_x)^2 - (\lambda f_y)^2}\right] & \sqrt{f_x^2 + f_y^2} < \frac{1}{\lambda} \\ 0 & \text{otherwise.} \end{cases} \quad (10.31)$$

The transfer function is split into two parts, one for traveling waves and one for evanescent waves. By applying this transfer function to a wave function, one can propagate the wave from one location to another. For optical systems where the transfer function is known, the result of the entire system can be calculated by taking the input field pattern, Fourier transforming it and then multiplying by each of the transfer functions in the order they are encountered. One of the most common and useful optical elements is the lens, and here I will review the salient points of the lens under Fourier optics.

A simple lens is two refracting surfaces (surfaces of a differing index of refraction than the host material, usually air) separated by a thickness. In this section, we will make several assumptions about the nature of the lens. First, we make the “thin-lens” approximation. This assumption means that we ignore the effect of the distance between the two refracting surfaces. In effect, the lens is assumed to be infinitely thin, so that the front refracting surface and the back refracting surface act simultaneously on the wavefronts that enter the lens.

The lens is also assumed to have a quadratic curve on both sides, although not necessarily the same curve on each side. This quadratic curve can be thought of in two ways. Because we are choosing the parameters for the lens, we can arbitrarily choose the surfaces to be quadratic in curvature. However, the curve can also be seen as the result of the paraxial approximation of a spherical lens. Although it is now possible to create aspheric optics (like a parabolic lens), spherical optics were the original choice for lenses because they are much easier both to make and to measure and correct for errors. The paraxial approximation considers only rays that lay on or near the optical axis of the system. The paraxial approximation of a spherical lens is a parabolic lens, where the approximation is valid only in the paraxial region around the optic axis of the system.

Finally, we assume that the lens is completely transparent (non-absorbing) and so the lens affects only the phase of the light. Using these assumptions, the phase transformation of the lens is given by:

$$t_{lens} = \exp \left[ -ik(n-1) \frac{x^2 + y^2}{2} \left( \frac{1}{R_1} - \frac{1}{R_2} \right) \right] \quad (10.32)$$

Using the well-known Gaussian optics formula for the focal length of a lens, equation (10.32) can be re-written as:

$$t_{lens} = \exp \left[ -ik \frac{x^2 + y^2}{2f} \right] \quad (10.33)$$

where  $f$  is  $(n-1) \left( \frac{1}{R_1} - \frac{1}{R_2} \right)$  and  $n$  is the index of refraction of the lens material. Now we can see what happens when an image beam of light is sent through a lens under a specific condition: the image is placed a distance  $f$  in front of the lens, and the output is viewed at a distance  $f$  in back of the lens. Under these conditions, the output is:

$$U_{out}(x_2, y_2) = \int_{-\infty}^{\infty} \int_{-\infty}^{\infty} U_{image}(x_1, y_1) \exp \left[ -j \frac{2\pi}{\lambda f} (x_2 x_1 + y_2 y_1) \right] dx_1 dy_1 \quad (10.34)$$

This can be recognized as the Fourier transform of the input image  $U_{image}$  with the spatial frequencies  $f_x = \frac{x_2}{\lambda f}$ ,  $f_y = \frac{y_2}{\lambda f}$ . Thus, a simple lens performs a two-dimensional Fourier transform on any input placed in its front focal plane, with the output appearing in the back focal plane. This is a key result in optics, and allows the construction of optical correlators such as the Vanderlugt and Joint-Transform correlators.

### 10.34f Imaging Systems

The  $4f$  imaging system is commonly used in laboratory optics experiments to transfer an image-bearing beam from location to location, to magnify/de-magnify an image, or to perform spatial filtering. A standard  $4f$  configuration is shown in Figure 10-2.

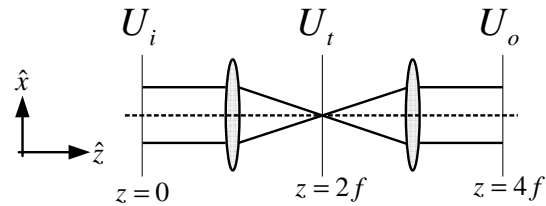


**Figure 10-2:  $4f$  System**

Two lens of equal focal length  $f$  are separated by a distance  $2f$ . The input to the system  $U_i$  is presented  $f$  in front of the first lens, and the output  $U_o$  is measured at a distance  $f$  away from the second lens. Therefore the total length of the optical system is  $4f$ . Using the results of Section 10.2 the field at  $z=2f$  will be:

$$U_t(x, y, z = 2f) = \frac{e^{i2kf}}{j\lambda f} \tilde{U}_i\left(\frac{x}{\lambda f}, \frac{y}{\lambda f}\right) \quad (10.35)$$

In equation (10.35),  $\tilde{U}_i\left(\frac{x}{\lambda f}, \frac{y}{\lambda f}\right)$  represents the Fourier transform of  $U_i$ , scaled by the wavelength and the focal length of the lenses. Thus at the middle of the  $4f$  system, the Fourier transform of the input is obtained. This allows for the opportunity to perform spatial filtering as follows. Consider a transparency placed at  $z=2f$  with a transmittance function  $t(x, y)$ . This function may be purely real, as it would be for an actual transparency with an absorbing or reflecting pattern etched into it, or it may be a phase-only function, which could be accomplished using a liquid-crystal screen. Finally, some special SLM's can achieve an amplitude and phase

modulation simultaneously. In any case, the transparency function is multiplied by the field obtained at  $z=2f$ , and the resulting field passes through the second lens of the system. It is simple to see that the second lens should perform in the same manner as the first lens, since it is also presented an input in its front focal plane and has the same focal length. Therefore, the output of the system is simply the Fourier transform of the field at the middle of the system:

$$U_o(x, y, z = 4f) = \frac{e^{i4kf}}{-(\lambda f)^2} F.T. \left[ t(x, y) \tilde{U}_i \left( \frac{x}{\lambda f}, \frac{y}{\lambda f} \right) \right] \quad (10.36)$$

If the transparency is absent, that is  $t(x,y)=1$ , then the result of equation (10.36) is simply the function  $U_i$  from the input, with no phase variation normally associated with diffraction, only the constant phase accrued from traveling a distance  $4f$ . If spatial filtering is desired, the transparency provides a simple means. For example, a transparency with a dark pinpoint spot in the center of the Fourier plane will provide a zero-frequency block. A larger dark circle could provide a high-pass filter. An aperture would provide a low-pass filter, and so on. In fact, the common spatial filter is a  $4f$  system with a very narrow low pass filter. All of the high frequency noise is thus filtered out of the beam, providing a clean, uniform profile. Spatial frequency filtering and diffraction-less propagation are the two principle uses of the  $4f$  system, and are covered extensively in Goodman's *Introduction to Fourier Optics* as well as the EECS course 382.

## 10.4 Common Holographic Calculations

For experimental holography using thick gratings, there are several common calculations that are used. These are used to calculate the proper writing angles in order to ensure certain readout properties. For instance, a common task is to write a grating using a laser of one wavelength for readout with a laser of a different wavelength. In this task and others, it is

important to calculate the grating period and slant. Here, I show how this may be done for the general case of an asymmetric (slanted) grating.

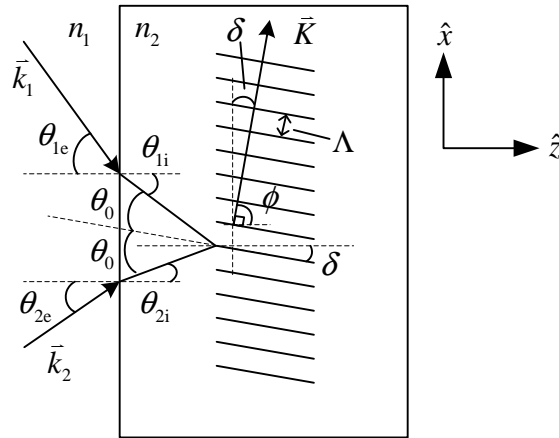


**Figure 10-3: Asymmetric Grating**

Figure 10-3 shows the geometry used to analyze this case. The two writing beams have k-vectors  $\vec{k}_1$  and  $\vec{k}_2$ , which are incident to the holographic material at external angles  $\theta_{1e}$  and  $\theta_{2e}$  respectively. Note that the asymmetric writing beams (differing angles) leads to a slant in the grating. The material has an index of refraction  $n_2$ , while the surrounding material (usually air) has an index  $n_1$ . In the figure, the material is shown in two sections, with a larger block of material surrounding the grating portion in the middle. This is a useful construct for visualizing the process, but does not represent the actual physical reality. The incident beams are refracted according to Snell's law ( $n_1 \sin \theta_e = n_2 \sin \theta_i$ ) to produce two beams inside the material at angles  $\theta_{1i}$  and  $\theta_{2i}$ . Once inside the material, the beams interfere and the material responds to the intensity of this interference pattern. This interference pattern is represented by the k-vector of the grating:

$$\vec{K} = \vec{k}_1 - \vec{k}_2 \quad (10.37)$$

where the magnitude is  $|\bar{K}| = K = \frac{2\pi}{\Lambda}$ , and  $\Lambda$  is the grating period. The angle  $\phi$  is the angle

of the grating vector  $\bar{K}$ . The value of  $\bar{k}_1$  and  $\bar{k}_2$  inside the material is:

$$\begin{aligned}\bar{k}_1 &= k_w (\hat{z} \cos \theta_{1i} - \hat{x} \sin \theta_{1i}) \\ \bar{k}_2 &= k_w (\hat{z} \cos \theta_{2i} + \hat{x} \sin \theta_{2i})\end{aligned}\quad (10.38)$$

where  $k_w$  is the wave-number inside the medium for the writing beams (the subscript w indicating a write parameter):

$$k_w = \frac{2\pi}{\lambda_w} n_2 \quad (10.39)$$

In order to analyze this case further, we first consider the symmetric case. If the angles of the writing beams were equal, equation (10.37) would yield:

$$\begin{aligned}\bar{K} &= -\hat{x}2k \sin \theta \\ K &= \frac{2\pi}{\Lambda} = |-\hat{x}2k \sin \theta|\end{aligned}\quad (10.40)$$

This yields the grating spacing for the symmetric case.

$$\Lambda = \frac{\lambda_w / n_2}{2 \sin \theta} \quad (10.41)$$

Now, we can reduce the asymmetric case to the symmetric case by choosing a new axis that is rotated from the z-axis by  $\delta$ , where  $\delta = \frac{\theta_{1i} - \theta_{2i}}{2}$ . By doing this, we are choosing a new

axis where the writing angles are symmetric inside the medium. The symmetric angle is  $\theta_0$ :

$$\begin{aligned}\delta &= \frac{\theta_{1i} - \theta_{2i}}{2} \\ \theta_0 &= \theta_{1i} - \delta = \theta_{2i} + \delta \\ \phi &= \frac{\pi}{2} - \delta\end{aligned}\quad (10.42)$$

Using this information and the result of (10.41), we have all the information for this grating.

In order to determine the result of readout from this grating using a different wavelength, we must set the readout angle such that the periodicity of the grating matches that of the reading wavelength. In other words, changing the wavelength of the read beam requires changing the angle of the beam so that the periodicity matches. This is expressed by:

$$\Lambda = \frac{\lambda_w/n_2}{2 \sin \theta_w} = \frac{\lambda_r/n_2}{2 \sin \theta_r} \quad (10.43)$$

Equation (10.43) can be solved for any angle given the other angle and two wavelengths, or solved for a wavelength given two angles and a wavelength.

## 11 Vita

John Thomas Shen was born on January 2, 1980 in Cleveland, Ohio. He attended Saint Ignatius high school in Cleveland, where he tutored math and was active in several regional youth music groups as well as the Boy Scouts of America, achieving Eagle Scout.

He attended Northwestern University in Evanston, Illinois, initially pursuing undergraduate degrees in music performance (clarinet) and computer engineering. He was active in the residential college system at Northwestern as well as playing ultimate Frisbee. Deciding to pursue engineering, he left the music performance program and concentrated his efforts on electrical engineering. During his senior year, after doing summer research with Professor Allen Taflove and taking several interesting optics courses, he applied to graduate schools in the area of optics and electrical engineering.

John joined Professor Selim Shahriar's Laboratory for Atomic and Photonic Technologies at Northwestern just as it was getting started in Evanston, and has done research in polarization optics and imaging, holographic data storage, and optical information processing. He married his college sweetheart Myra Sutanto, whom he met at Northwestern, in August of 2006. After graduating from Northwestern, John will go to work with Stryker Endoscopy in San Jose, helping to develop their next-generation medical systems.

### *Publications*

1. J. T. Shen and M. S. Shahriar, "A Simple Method for Bragg Diffraction in Volume Holographic Gratings," submitted to the American Journal of Physics (2007).
2. J.-K. Lee, J. T. Shen, and M. S. Shahriar, "Demonstration of a Spectrally Scanned Holographic Stokesmeter," submitted to Optics Communications, (2007).
3. J. K. Lee, J. T. Shen, and M. S. Shahriar, "Photonic Bandgap-based Stokesmeter," in *Work in progress*, (2007).
4. J. T. Shen, G.S. Pati, M. S. Shahriar, "Lenslet array for a super-parallel holographic memory," submitted to Optical Engineering, (2007).

5. J. K. Lee, J. T. Shen, A. Heifetz, R. Tripathi, and M. S. Shahriar, "Demonstration of a thick holographic Stokesmeter," *Optics Communications* **259**(2), 484-487 (2006).
6. A. Heifetz, J. T. Shen, J. K. Lee, R. Tripathi, and M. S. Shahriar, "Translation-invariant object recognition system using an optical correlator and a super-parallel holographic random access memory," *Optical Engineering* **45**(2), - (2006).
7. A. Heifetz, G. S. Pati, J. T. Shen, J. K. Lee, M. S. Shahriar, C. Phan, and M. Yamamoto, "Shift-invariant real-time edge-enhanced VanderLugt correlator using video-rate compatible photorefractive polymer," *Applied Optics* **45**(24), 6148-6153 (2006).
8. H. N. Yum, P. R. Hemmer, A. Heifetz, J. T. Shen, J. K. Lee, R. Tripathi, and M. S. Shahriar, "Demonstration of a multiwave coherent holographic beam combiner in a polymeric substrate," *Optics Letters* **30**(22), 3012-3014 (2005).
9. M. S. Shahriar, J. T. Shen, M. A. Hall, R. Tripathi, J. K. Lee, and A. Heifetz, "Highly polarization-sensitive thick gratings for a holographic Stokesmeter," *Optics Communications* **245**(1-6), 67-73 (2005).
10. A. Heifetz, "Shift-Invariant Real-Time High-Speed Optical Image Correlation System," (Northwestern University, Evanston, IL, 2005).
11. H. N. Yum, P. R. Hemmer, R. Tripathi, J. T. Shen, and M. S. Shahriar, "Demonstration of a simple technique for determining the M/# of a holographic substrate by use of a single exposure," *Optics Letters* **29**(15), 1784-1786 (2004).
12. M. S. Shahriar, R. Tripathi, M. Huq, and J. T. Shen, "Shared-hardware alternating operation of a super-parallel holographic optical correlator and a super-parallel holographic random access memory," *Optical Engineering* **43**(8), 1856-1861 (2004).
13. M. S. Shahriar, J. T. Shen, R. Tripathi, M. Kleinschmit, T. W. Nee, and S. M. F. Nee, "Ultrafast holographic Stokesmeter for polarization imaging in real time," *Optics Letters* **29**(3), 298-300 (2004).
14. M. S. Shahriar, R. Tripathi, M. Kleinschmit, J. Donoghue, W. Weathers, M. Huq, and J. T. Shen, "Superparallel holographic correlator for ultrafast database searches," *Optics Letters* **28**(7), 525-527 (2003).
15. M. S. Shahriar, J. Riccobono, M. Kleinschmit, and J. T. Shen, "Coherent and incoherent beam combination using thick holographic substrates," *Optics Communications* **220**(1-3), 75-83 (2003).

#### *Conference Presentations*

1. J. K. Lee, J. T. Shen, S. Tseng, G. Pati, M. S. Shahriar, "Demonstration of a spectrally multiplexed holographic Stokesmeter," presented by J. T. Shen at *Frontiers in Optics*, October (2006).
2. J. K. Lee, J. T. Shen, S. Tseng, G. Pati, M. S. Shahriar, "A volume-grating Stokesmeter based on photonic band-gap structures," presented by J. T. Shen at *Frontiers in Optics*, October (2006).
3. J. T. Shen, J. K. Lee, A. Heifetz, G. S. Pati, R. Tripathi, J. Donoghue, S. Tseng, M. S. Shahriar, "Poly(methyl methacrylate)-based material for thick holographic memory plates and ultra-narrow filters," presented by J. T. Shen at *Frontiers in Optics*, October (2005).
4. H. N. Yum, P. Hemmer, A. Heifetz, J. T. Shen, J. K. Lee, R. Tripathi, M. S. Shahriar, "Demonstration of a multiwave coherent holographic beam combiner in a polymeric substrate," presented by J. T. Shen at *Frontiers in Optics*, October (2005).

5. J. K. Lee, J. T. Shen, A. Heifetz, R. Tripathi, M. S. Shahriar, "Spectrally scanned polarimetric imaging using a thick holographic Stokesmeter," presented by J. T. Shen at *Frontiers in Optics*, October (2005).
6. M. S. Shahriar, R. Tripathi, J. T. Shen, et al., "High speed data-search and pattern identification using a hybrid super-parallel holographic RAM-JTC geometry," presented by J. T. Shen at the *SPIE Defense & Security Symposium* (2005).
7. M. S. Shahriar, J. T. Shen, J. K. Lee, R. Tripathi, "Super-parallel holography and holographic polarimetry for optical pattern recognition," presented by J. T. Shen at the *SPIE Defense & Security Symposium* (2004).
8. M. S. Shahriar, A. Heifetz, J. T. Shen, "A landmark identification-based navigation system using a hybrid holographic correlator," presented by A. Heifetz at *SPIE Photonics West* (2005).
9. M. S. Shahriar, J. K. Lee, J. T. Shen, A. Heifetz, R. Tripathi, "Demonstration of a thick holographic Stokesmeter," presented by J. K. Lee at the *Conference on Lasers and Electro-Optics* (2005).
10. "Shift-Invariant Real-Time Edge-Enhanced VanderLugt Correlator Using Video-Rate Compatible Photorefractive Polymer," A. Heifetz, G.S. Pati, J. T. Shen, J.-K. Lee, M. S. Shahriar, C. Phan, and M. Yamamoto, presented at CLEO, Long Beach, California, (May 2006).
11. "Demonstration Of A Spectrally Multiplexed Holographic Stokesmeter," Jong-Kwon Lee, John.T. Shen, Alex. Heifetz, and M. S. Shahriar," presented at CLEO, Long Beach, California, (May 2006).
12. "Demonstration of a Thick Holographic Stokesmeter," M. S. Shahriar, J-K. Lee, J. T. Shen, A. Heifetz, R. Tripathi, presented at CLEO/QELS, Baltimore, MD, (May 2005).
13. "High speed data search and pattern identification using a hybrid super-parallel holographic RAM-JTC geometry," M. S. Shahriar, Renu Tripathi, J. T. Shen, A. Heifetz, J-K. Lee, presented at SPIE Aerosense, invited (2005).
14. "Holographic Polarimeter Utilizing the Polarization Dependency of Thick Holographic Substrates," M. S. Shahriar, J. T. Shen, J-K. Lee, R. Tripathi, and A. Heifetz, presented at the OSA Annual Meeting, Rochester, NY (2004).
15. "Spatio-Angular Parallelism in a Holographic Correlator and Random Access Memory," M. S. Shahriar, J. T. Shen, R. Tripathi, J-K. Lee, and A. Heifetz, presented at the OSA Annual Meeting, Rochester, NY (2004).
16. "A Hybrid Correlator and RAM Using Super-Parallel Holography," M. Andrews, M. Huq, J. Shen, R. Tripathi, and M. S. Shahriar, presented at the SPIE Photonics West, San Jose, CA (Jan., 2004). (Invited Paper)
17. "Demonstration of a single exposure technique for determining the M/# of a holographic substrate," H. N. Yum, P. R. Hemmer, R. Tripathi, J. T. Shen, and M. S. Shahriar, presented at the CLEO/IQEC, San Francisco, CA (2004).
18. "Holographic Stokesmeter Using Polarization-Sensitive Volume Gratings," M. S. Shahriar, J. T. Shen, Renu Tripathi, J. K Lee, and M. A. Hall, presented at CLEO/IQEC, San Francisco, CA (2004).
19. "Demonstration of a super-parallel holographic RAM using the super-parallel holographic optical correlator architecture," M. S. Shahriar, R. Tripathi, M. Huq, and J.T. Shen, presented at CLEO/IQEC, San Francisco, CA (2004).